H4.SMR/204-20

WINTER COLLEGE

ON

DIAGNOSTIC ATOMIC AND MOLECULAR SPECTROSCOPY

9 March - 3 April 1987

A. HYDROSPHERIC DIAGNOSTICS.

B. ATMOSPHERIC DIAGNOSTIC METHODS INVOLVING MICROWAVE SPECTROSCOPY (SEMINAR).

D.T. GJESSING

Royal Norwegian Council for Scientific
and Industrial Research
Kjeller
Norway

INTERNATIONAL CENTER FOR THEORETICAL PHYSICS

Trieste Course (March - April, 1987)

on

HYDROSPHERIC DIAGNOSTICS

Interaction of electromagnetic waves with sea surface involving scattering and diffraction

by

Dag T Gjessing

Royal Norwegian Council for Scientific and Industrial Research
Environmental Surveillance Technology Programme

and

University of Tromsö
Institute of Mathematical and Physical Sciences

5 SEA CLUTTER BACKGROUND, CHARACTERIZATION OF OCEAN SURFACE

This section will be devoted to ocean surface phenomena. The objective is to illustrate the matched illumination principle to sea surface scattering. As before, we characterize the scattering surface by a space time delay function $\sigma(\vec{r},t)$ which tells us how the scattering cross-section σ varies with position $\vec{r}$ and time t, or we use the Fourier transform of this delay function which is the well-known irregularity spectrum $\Phi(\vec{K},\omega)$. Note that at the moment we make no attempt to relate scattering cross-section to wave height. All we need in order to apply our adaptive radar method is information about the space time spectrum $\Phi(\vec{K},\omega)$ of scattering cross-section.

There are many air/sea phenomena which play a role in relation to backscattering of radio waves in the microwave region: gravity waves "modulate" the capillary wave structure, overturning wave crests produce focusing effects and also periodic regions of strong turbulence, the boundary layer wind field with strong turbulence amplified by the ocean waves will conceivably leave a patchy and even periodic footprint on the sea surface. Internal waves originating from density gradients in this ocean further complicate the sea surface irregularity pattern.

By virtue of the fact that our particular multifrequency radar, used as an example, allows one to measure the velocity distribution ("coherent and incoherent component") associated with 15 different ocean irregularity scales simultaneously in a directional manner, it is possible to study the different air/sea mechanisms in some degree of detail.

Radio methods have a substantial potential in the study of the irregularity structure of the sea surface for several reasons:

- They provide a rather unique possibility to measure the directional wave spectra with good directional resolution

- By means of a multifrequency radio method wavelength and wave velocity can be measured independently

- It is also possible to distinguish between coherent wave motion and incoherent motion (turbulence) and between dispersive and non-dispersive wave phenomena.

We shall present a simple theory and experimental examples of the sea surface. We shall in particular demonstrate that a microwave illuminator can be tailored so as to optimize the coupling between electromagnetic waves and ocean wave phenomena.

It is important at this early stage to specify our aims and establish perspectives. There are three rather distinctly different problem areas:

1) One must obtain an understanding of the coupling mechanisms between the electromagnetic waves on the one hand and the sea surface on the other. The scattering medium can conveniently be described as a function of space and time $f(\vec{r},t)$ or by the four-dimensional spectrum which is expressed by the Fourier transform $E(\vec{K},\omega)$ of this space time distribution. Bandwidth measurements were introduced many years ago to determine this function characterizing the scattering medium. Particularly powerful were the methods introduced by Waterman et al. (1961) and Crawford et al. (1959).
   We shall be using a technique very similar to these, which was also analysed in connection with studies of waves and turbulence in the atmosphere (Gjessing 1962).

2) Having established information about the sea surface as a scattering surface for radio waves (the delay function $f(\vec{r},t)$ or the spectrum $E(\vec{K},\omega)$), it remains necessary

to establish the relationship between this "description domain of the radio scientist" and that of the ocean scientist, who wants information about the most significant waveheight, waveheight spectra, etc. To convert from scattering cross-section to waveheight one needs information about how gravity waves and other large-scale phenomena affect small-scale phenomena (capillary waves) which are comparable with the wavelength of the radio field and which are responsible for the scattering. In this context the term "modulation transfer function" is appropriate. Since there are many ocean surface phenomena which contribute (see section 2.2), it is not a straightforward task to convert from scattering cross-section to waveheight. Pioneers in this field of science are Wright[1968], Plant[1977], Schuler[1978], Hasselmann[1973], Alpers[1978], Valenzuela[1978], Barrick 1972 and others.

3) One needs an understanding of the fundamental hydrodynamic mechanisms. The list of notable scientists in this field is, of course, very long, ranging from the days of Reynolds and Richardson to present-day contributors, such as Hasselmann and Phillips.

Here we shall confine ourselves to the first problem area, the interaction between electromagnetic waves and an irregular ocean surface. We describe the sea surface in terms of the delay function $f(\vec{r},t)$ and in terms of the four-dimensional spectrum $E(\vec{K},\omega)$ and thus obtain information about the sea surface in terms of radio bandwidth. We do not enter into the very complex and often speculative field of science involved with establishing a "modulation transfer function" to be able to obtain quantitative information about waveheight. We limit ourselves to giving relative distributions.

For details the reader is referred to (Gjessing, Hjelmstad, Lund 1985 and Gjessing and Hjelmstad 1986).

Before we discuss the various coupling mechanisms between electromagnetic and ocean waves, however, a brief description of the dynamic properties of the sea is of relevance.

Fig. 5.1 introduces this section. As we have shown at several earlier instances already, a spectrum of electromagnetic waves $E(\vec{K})$ couple to the same sea surface irregularities $\Phi(\vec{K})$ (see Fig. 2.4 above).

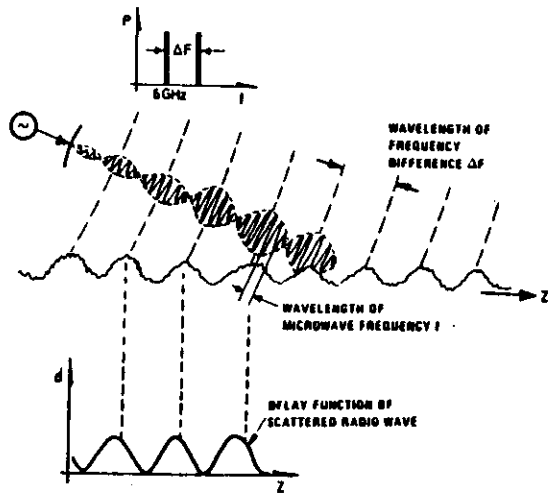

Fig. 5.1 Electromagnetic waves $E(\vec{K})$ interact with ocean waves when their irregularity spectrum $\Phi(\vec{\kappa}) = E^*(\vec{K})$. (Gjessing 1981a © IEEE).

5.1 The motion pattern of the sea surface irregularity structure

In the section above, we have shown that frequency components with mutual frequency spacing ΔF couple to irregularity scale sizes $\Delta L = \frac{c}{2\Delta F}$ (to wavenumbers $\frac{2\pi}{\Delta L} = \frac{4\pi\Delta F}{c}$).

Any irregularity structure, periodic or random non-periodic, can be resolved into its wavenumber spectrum (Fourier component) as illustrated in Fig. 2.4. Keeping track of the time

history of the spatial covariance function $V(F)V^*(F+\Delta F)$, we obtain information about the motion pattern of the irregularity scale ΔL.

We shall now consider the motion pattern of the ocean surface structure. We shall briefly consider three classes of surface structures and discuss ways by which these can be separated by signal analysis methods:

- Surface "coherent" gravity waves resulting from a distant wind field.
- Internal waves set up in a density gradient in the sea and coupled to the surface irregularity structures.
- Incoherent turbulent irregularity structure resulting from a local wind field.

For the purpose of illustrating the basic principles involved, first order expressions will form the basis for the simple calculations.

Let us first consider surface gravity waves expressed by the basic equation

$$\omega^2 = g\, k \tanh kd \qquad (5.1)$$

where k is the wavenumber (spatial frequency) and d the depth.

For deep water $kd >> 1$ and the wave equation becomes

$$\omega^2 = g\, k$$

The phase velocity is given by

$$v_{ph} = \frac{\omega}{k} = \sqrt{\frac{g}{k}} \qquad (5.2)$$

whereas the group velocity becomes

$$v_g = \frac{d\omega}{dk} = 1/2\sqrt{\frac{g}{k}} \qquad (5.3)$$

We have already observed that a beat frequency ΔF couples to scales $L = \frac{c}{2\Delta F}$.

The phase velocity of gravity waves is therefore given by

$$v = \sqrt{\frac{gc}{4\pi\Delta F}} \qquad (5.4)$$

Since the Doppler shift produced by a scattering element is given by

$$f = \frac{1}{2\pi} \vec{K} \cdot \vec{V}$$

for backscattering this gives

$$f = \sqrt{\frac{g\ \Delta F}{c\pi}} \qquad (5.5)$$

We note that the gravity waves are dispersive such that the Doppler shift is proportional to the square root of the illuminating frequency ΔF matched to the irregularity scale (ocean wavelength) L given by $L = c/2\Delta F$.

Then let us consider internal waves set up in an interface between water of two different densities as indicated in Fig. 5.2.

The wave equation for such waves is very much analogues with that for gravity waves on shallow water (Dysthe 1980).

$$\omega^2 = g \frac{\delta\rho}{\rho} k \tanh k d$$

i.e.

$$v_{ph} = \frac{\omega}{k} = \begin{cases} \sqrt{\frac{\delta\rho}{\rho} \frac{g}{k}} & \text{when } kd >> 1 \\ \sqrt{\frac{\delta\rho}{\rho} gd} & \text{when } kd << 1 \end{cases} \qquad (5.6)$$

For long waves on a shallow thermocline $(kd << 1)$ we therefore have that

$$v_{ph} = v_g = \sqrt{\frac{\delta\rho}{\rho} d\ g} \qquad (5.7)$$

i.e. no dispersion.

Note that since the density step in practice is in the order of 10^{-3} there will be practically no height modulation of the sea surface since the amplitude of the sea surface modulation is reduced by a factor $\frac{\delta\rho}{\rho}$ relative to that of the thermocline.

However, due to the periodic variation of the surface current resulting from the internal waves as illustrated in Fig. 5.2, the surface gravity waves will see a periodic current.

Now let us finally briefly consider the effect of these surface currents.

Based on the principle of adiabatic invariance, it can be shown (Dysthe 1980) that if a gravity wave is moving with a group velocity v_g in the direction of the current of velocity $\bar{u}$, the following relation applies

$$E\ v_g(v_g + \bar{u}) = \text{constant}$$

Hence, the energy E and accordingly the wave amplitude of the gravity wave must increase when the wave travels in the

direction of the surface current and decrease when it travels in the opposite direction.

When $v_g = \bar{u}$ the effect of the current becomes very dominating.

Referring again to Fig. 5.2, one would therefore expect certain scales on the sea surface to be particularly influenced by the internal waves, namely those which are associated with a velocity equal to that of the internal waves.

To obtain an expression for these scales we equate the group velocity of the surface waves and that of the internal wave.

Hence

$$1/2\sqrt{\frac{g}{k}} = \sqrt{\frac{\delta\rho}{\rho} g d} \qquad (5.8)$$

giving us a measure of the scale L on the sea surface which will be most strongly influenced by the internal wave as:

$$L = \frac{2\pi}{k} = 8\pi \frac{\delta\rho}{\rho} d \qquad (5.9)$$

In order to couple to that irregularity scale with a radar system, a ΔF given by the follcwing equation is required

$$\Delta F = \frac{c}{2L} = \frac{c}{16 \pi d \frac{\delta\rho}{\rho}} \qquad (5.10)$$

Typical values of d and $\frac{\delta\rho}{\rho}$ are 50 meters and 10^{-3} respectively, giving us a coupling frequency of 119 MHz (irregularity scale 1.25 meters).

The Doppler shift caused by the internal waves is thus

$$f = \frac{1}{2\pi} \vec{K} \cdot \vec{V}$$

$$f = \frac{2\Delta F}{c} \sqrt{\frac{gd}{\rho}} \qquad (5.11)$$

As an illustration of interaction between internal waves and surface waves Fig. 5-2 is presented.

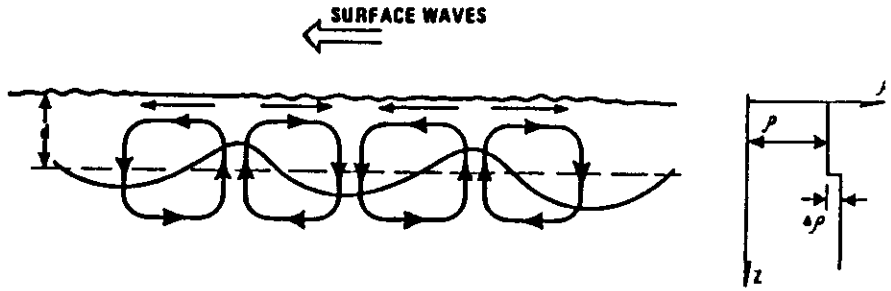

Fig. 5.2 The gravity wave will see a periodic current on the surface when an internal wave structure is present.

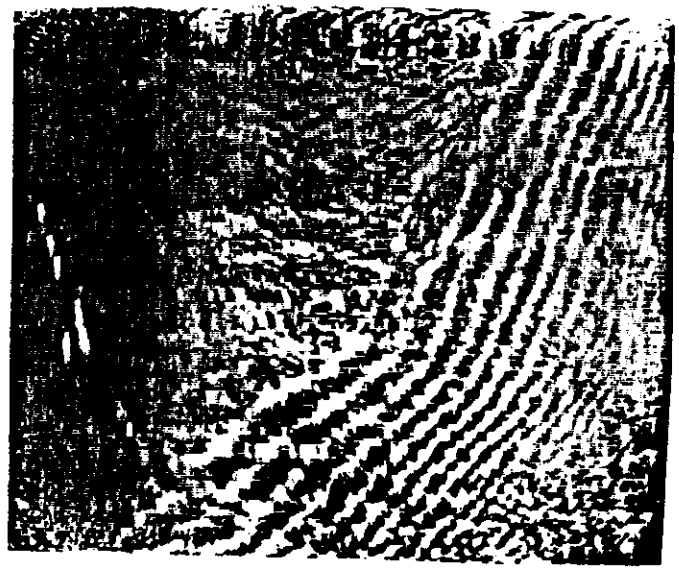

Fig. 5.3 Internal wave pattern off the south-eastern coast of Norway depicted by SLAR. Recording on 7 Sep 83 by Fjellanger-Widerøe AS/Norwegian State Pollution Control Authority (Svein-Eirk Høst). The wavelength of the periodic structure is approximately 500 m. Photograph covers an area of approximately 8 by 5 km. (Gjevik 1984).

In contrast, note that the gravity waves give rise to a Doppler shift given by

$$f = \sqrt{\frac{g\ \Delta F}{c\pi}}$$

5.2 Ocean wave spectra, waveheight, wavelength

Having concluded the section on motion pattern in relation to wavelength, it remains to consider the wave amplitude. Wave spectra for various conditions of fetch and wind velocity have been studied by many fluid dynamicists, also in recent years of which in particular Phillips[1969], Pierson-Moskovitz[1964] and Hasselmann[1973] (JONSWAP) should be mentioned. A brief sketch of the essential findings will now be given.

O.M. Phillips (1969) considers the dissipation mechanisms through breaking waves and regards these as the limiting factor for growth. For a fully developed sea when the wind has acted on the sea for a sufficiently long time so that the phase velocity of the gravity waves is the same as the wind velocity, no more energy can be transferred from the wind field into the ocean waves.

Hence the phase velocity of the dominant wave in the wave spectrum is equal to the wind speed; we have resonant conditions. Under such conditions we have that the wind speed u is given by

$$u = v = \frac{\omega}{K}$$

where v is the phase velocity of the ocean wave, ω its angular frequency and K its wavenumber.

Under such conditions Phillips gives the following expression for the waveheight spectrum

$$s(f) = \begin{cases} \frac{0.01\ g^2}{(2\pi)}\ f^{-5} & \text{for } f > \frac{g}{2\pi u} \\ 0 & \text{for } f < \frac{g}{2\pi u} \end{cases} \qquad (5.12)$$

Since the relationship between wave frequency $f = \frac{\omega}{2\pi}$ and ocean wavelength L is given by

$$L = \frac{g}{2\pi f^2}$$

the cut-off wavelength L_m is given by

$$L_m = \frac{2\pi u^2}{g}$$

The Phillips expression is shown in Fig. 5.4B.

For comparison, a measured spectrum after Moskovitz is also shown.

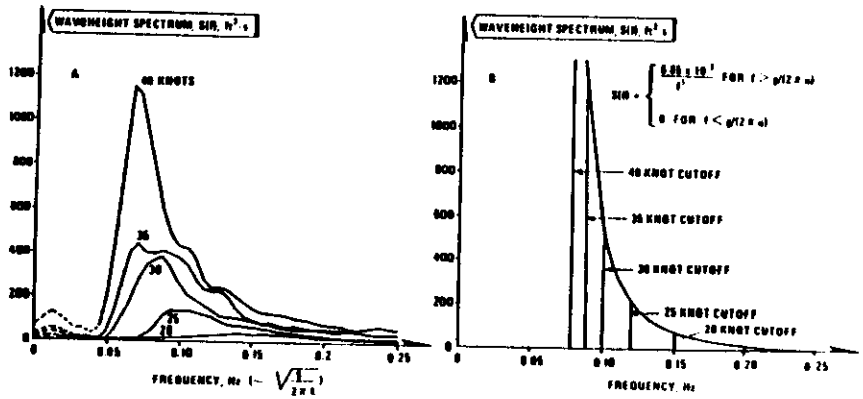

Fig. 5.4 Measured and model waveheight temporal spectra.
A: Measured (after Moskovitz, 1964); seas are not fully developed at winds about 25 knots.
B: Phillips model for fully developed seas.

Pierson-Moskovitz give a similar spectrum with the addition of an $\exp\{-(\frac{f_m}{f})^4\}$ term

$$S(f) = \frac{0.01\, g^2}{(2\pi)^4} f^{-5} \exp\{-\frac{5}{4}(\frac{f_m}{f})^4\} \qquad (5.13)$$

Pierson-Moskovitz measure the driving wind u at a height of 19.5 m above sea level. As before $f_m = \frac{g}{2\pi u}$

Finally, the model developed by Hasselman from the JONSWAP also takes fetch into consideration. For infinite fetch, the Hasselman expression degenerates to a spectrum similar to that of Pierson-Moskovitz.

Hasselman suggests the following waveheight spectrum

$$E(f) = \frac{\alpha\, g^2}{(2\pi)^4} f^{-5} \exp\{-\frac{5}{4}(\frac{f}{f_m})^{-4}\}\ \gamma^{\exp\{\frac{-(f-f_m)^2}{2\sigma^2 f_m^2}\}} \qquad (5.14)$$

$$= \begin{cases} \sigma_a & \text{for } f < f_m \\ \sigma_b & \text{for } f > f_m \end{cases}$$

The various parameters are defined in Fig. 5.5 showing the results of the JONSWAP experiments for different values of fetch. Note that for a fully developed spectrum $\gamma = 1$ and $\alpha = 0.01$.

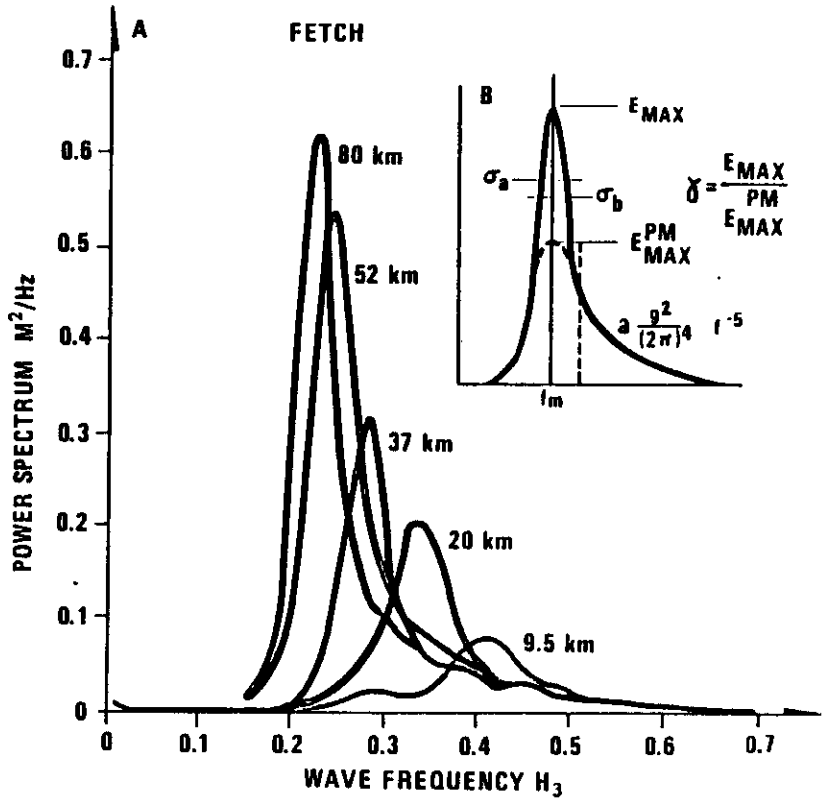

Fig. 5.5 JONSWAP experimental spectra for different values of fetch (Hasselman et al. (1973).

5.3 Interaction mechanisms between plane electromagnetic waves and sea surface irregularities, basic principles

The basic scattering equation can be expressed as

$$E_s(\vec{K},t) \sim \int_{-\infty}^{\infty} f(\vec{r},t)\, e^{-j\vec{K}\cdot\vec{r}}\, d^3\vec{r} \qquad (5.15)$$

$$\vec{K} = \vec{k}_i - \vec{k}_s \quad \text{and} \quad |\vec{K}| = \frac{4\pi}{\lambda} \sin \theta/2$$

λ is wavelength and θ scattering angle.

In order to obtain backscatter from a scattering surface, the surface must have a structure, regular or irregular, containing scale sizes $L = \frac{2\pi}{K} = \frac{\lambda}{2}$. Referring again to equation (5.15), $\vec{r}$ is a position vector, t is time and $f(\vec{r})$ is the delay function characterizing the surface. This complex function tells us how the scattering elements contributing to the 'bulk scattering cross-section σ' are distributed spatially.

By considering the inverse transform $f(\vec{r}) \sim \int E(\vec{K}) \exp(j\vec{K}\cdot\vec{r})\, d\vec{K}$ we see that a general scattering medium can be characterized by a sum of Fourier components $E(\vec{K})$. For our electromagnetic field to give constructive backscatter from this structure, the wavenumber of the electromagnetic wave $\vec{K}_{EM}$ must be 'matched to' (be equal to) that characterized by the Fourier component of the reflecting structure $\vec{K}_{STR}$ (Crawford et al. 1959). We now dwell on this statement for a moment and consider the $f(\vec{r})$ function in relation to a reflector such as the sea surface.

First consider the case of a rigid (frozen) structure or a structure varying slowly with time. The general four-dimensional irregularity spectrum reduces to a three-dimensional spectrum

$$E(\vec{K}) \sim \int_{-\infty}^{+\infty} f(\vec{r})\, \exp(-j\vec{K}\cdot\vec{r})\, d\vec{r}$$

Note that this simple treatment assumes a rough scattering surface (diffuse non-specular scattering). We first assume that the scattering surface is one-dimensional (unidirectional waves) in the sense that the lines of constant $f(\vec{r})$ are parallel. All waves, irrespective of wavelength, are assumed to propagate in the same direction. This means that the delay function $f(\vec{r})$ reduces to a simple function of z normal to the wave front. The expression for the scattered field can then be written as (Gjessing et al. 1964 a and b)

$$E(\vec{K}) \sim \int_{-\infty}^{\infty} f(\vec{r}) \{\exp -j(K_x x + K_z z)\} dx\, dz$$

where x and z are orthogonal coordinates in the horizontal plane. But with a set of unidirectional ocean waves, $f(\vec{r})$ reduces to $f(z)$, the scattering function (the delay function) being constant in the x direction. Thus we have

$$E(\vec{K}) \sim \int_{-\infty}^{\infty} \exp(-jK_x x)\, dx \int f(z) \exp(-jK_z z)\, dz \qquad (5.16)$$

The integral having x argument is immediately recognized as the Fourier integral representation of the Dirac delta distribution since $f(x)$ is constant, so that the above expression may be rewritten

$$E(\vec{K}) \sim \left[\int_{-\infty}^{\infty} f(z)\, \exp(-jK_z z)\, dz\right] \delta(K_x x) \qquad (5.17)$$

The scattered field $E(K)$ vanishes unless K_x is zero. Hence, $E(\vec{K})=0$ unless $\vec{K}$ is normal to the wave crest. We see that in order for this statement to be strictly correct, we have to perform a $-\infty$ to $+\infty$ integration. This again implies that we have to illuminate the scattering surface over a large area compared to the ocean wavelength under investigation.

Let us assume that we illuminate the sea surface with a beam whose width is limited so as to cut out a section D of the ocean wave front (see Fig. 5.6). In this case $E(K_x)$

will be of a sinc form instead of the Dirac delta function when approximating the antenna beam function to a rectangular distribution. Thus, if D is the width of the truncation influencing $f(x)$, and $K = 2\pi L$ is the wavenumber of the one-dimensional delay function $f(z)$ (L is the ocean wavelength) then the angular width (angle between nulls) 2α of the $E(K_x)$ function is

$$2\alpha = \frac{L}{D}$$

This is a relationship well known from antenna theory. The beamwidth 2α (azimuth resolution) is determined by the antenna aperture D expressed in wavelengths L.

If the intensity distribution of the illuminator is not a simple rectangular one, the effect of the convolution (truncation) will be different. In general, we have to compute the Fourier transform of the illumination intensity in the x direction in order to obtain the angular distribution of the radio power scattered back from a plane ocean wave. This scattering property of plane ocean waves can be illustrated in a simple manner. From Fig. 5.6 we see that if the

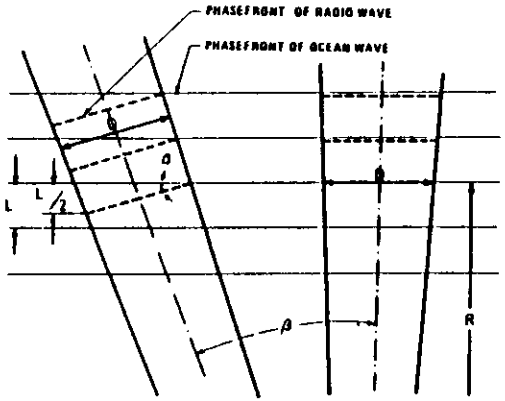

Fig. 5.6 The geometry of the truncation (convolution) process.

radar antenna is pointing in a direction such that the phase front of the ocean waves coincides with that of the radio waves, constructive interference will take place. Turning the antenna through an azimuthal angle β, a situation arises where the radio waves which are scattered from one-half of the illuminated ocean area cancel those scattered from the other half by destructive interference. This leads to a null in the angular power spectrum of the backscattered waves. As seen from Fig. 5.6 the azimuth angle giving rise to zero backscatter is given by $\beta = \tan^{-1}(L/2D)$. This is illustrated in Figs. 5.7 and 5.8 and verified experimentally in Fig. 5.26 (see section 5.4).

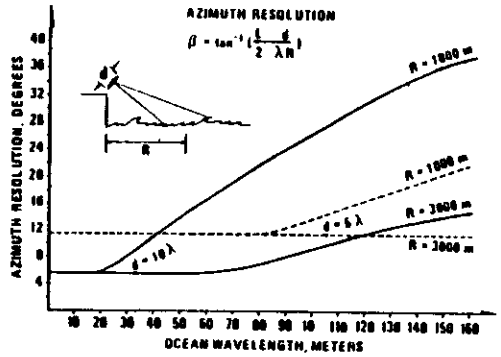

Fig. 5.7 The angular resolution is determined by ocean wavelength and by the width of the illuminated spot on the sea surface.

In Fig. 5.8 this function is plotted in polar coordinates.

Having considered the effect of a limited footprint size in regard to azimuthal resolution (wave direction), let us now consider the ocean wavelength resolution. The radar antenna is illuminating a range interval B measured along the

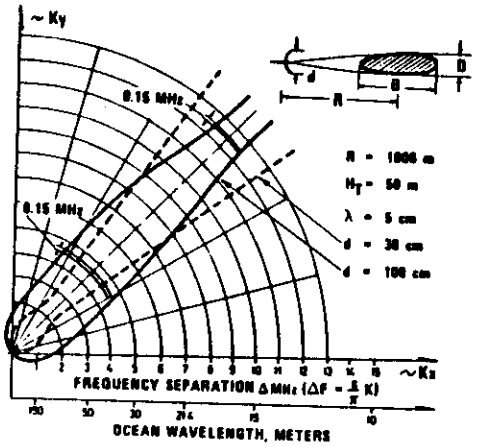

Fig. 5.8 The angular resolution of our radar varies with ocean wavelength. As the ocean wavelength decreases, the resolution approaches that of the antenna beamwidth. (R is range; H_T is height of radar above sea surface; λ is radio wavelength, and d is antenna aperture). (Gjessing and Hjelmstad 1986).

direction of wave propagation. This leads to a truncation of the delay function $f(\vec{r})$. We now assume that the field-strength distribution over the spot-length B can be approximated by an exponential function. This is a reasonable assumption as the field-strength decreases with the square of the distance and the intensity distribution through the antenna beam can be approximated by a Gaussian distribution.

The scattered field-strength is, as we have seen (see equation (5.17)), proportional to the Fourier transform of the delay function $f(\vec{r},t)$, which again is proportional to the incident field-strength. Our exponential illumination distribution will, therefore, lead to a convolution integral. The sinusoidal sea surface is convolved with the exponential

function leading to a widening of the filter function. If there had been no such truncation, our filter would have been a δ-function centred at the frequency (c/2πL), where L is the ocean wavelength. Note that we have disregarded the cos α term stemming from a finite depression angle α. The exponential truncation leads to a widening of the filter function given by

$$\delta F_{12} = 0.16 \frac{c}{B}$$

where δF is the half-power width (see, for example, Gjessing 1978). B is determined by the antenna beamwidth and by geometry (see Figs. 5.8 and 5.9). For this case we

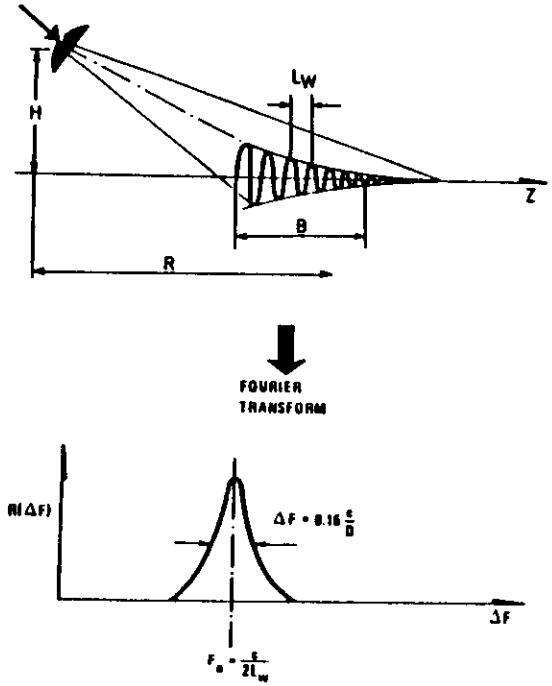

Fig. 5.9 As a result of a limited distribution in range of the illuminating spot, truncation effects (convolution) lead to degradation of the wave-number resolution (degradation of the coupling between electromagnetic waves and ocean waves).

have

$$\frac{\delta F_{12}}{F_0} = 1.28 \times 10^{-3} L$$

For a 100 m wavelength we therefore get a 12 per cent wavelength resolution.

In concluding this discussion on the scattering of radio waves from plane ocean waves, we should note that due to convolution effects caused by a limited spot-size the complex $E(\vec{K})$ spectrum will not be a simple expression involving a δ-function as shown in equation (5.17). We shall have to deal with a somewhat more complicated situation, an example of which is shown in Fig. 5.9.

In section 5.3.2 a set of experimental results are presented. We now suggest a simple mathematical model based on basic and rather intuitive physical arguments to provide a simple way of assessing the experimental findings. We assume that long ocean waves (wavenumber approaching cut-off K_o) are unidirectional. The higher the wavenumber, the larger the angular spread. For waves in the wavenumber region above K_s, the irregularity structure is isotropic.

We shall not involve ourselves in a detailed discussion on angular spread as a function of wavenumber. We therefore write the complex irregularity spectrum simply as

$$E(\vec{K}) = E(|\vec{K}|,\theta) \cdot K^{-n} (\cos\theta)^s$$

where s, the planeness parameter, is expressed as

$$s = \frac{K_s - K}{K - K_o}$$

K_o is the wavenumber corresponding to the short wavenumber cut-off and K_s is the wavenumber at which the ocean surface structure becomes 'random' and isotropic with no pre-

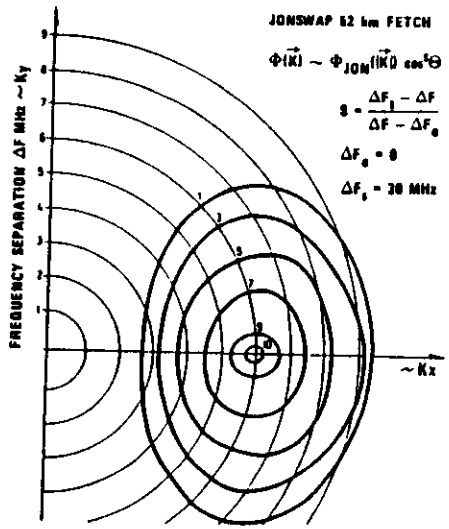

Fig. 5.10 Complex wave spectrum calculated from the simple model presented above. Waves having long wavelength are plane, small-scale irregularities are isotropic. The example presented is for $K_o = 0$ and $K_1 = 2\pi\ 5m^{-1}$. (Gjessing, Hjelmstad, Lund 1985).

vailing wave direction. This form satisfies the limiting conditions expressed above: long waves are unidirectional since the exponent $s \to \infty$ as $K \to K_o$. Short waves are isotropic since the exponent $s \to 0$ as $K \to K_s$. Figure 5.10 shows an example of such a two-dimensional wavenumber spectrum. Note that we have used the JONSWAP results of Hasselmann et al. (1973) for the scalar wavenumber spectrum $\Phi_{JON}(|\vec{K}|)$. For details the reader is referred to Phillips (1969). In short, the JONSWAP experiments show that the wave frequency f_o corresponding to maximum spectral intensity is determined by the fetch F through the approximate relation $f_o \sim F^{-1.4}$.

Note that this $\cos^{8}\theta$ angular spread model gives a 50^{o} half-power width of the angular spectrum of 25 m waves (6 MHz), while the 50 m waves have a spread of only 30^{o}.

This simple model is in agreement also with the JONSWAP experimental results. By the aid of a linear array of wave meters, it was observed that the angular spread of waves in the vicinity of the cut-off frequency f_m is much smaller than that for shorter ocean waves.

As a means of comparison, the complex wavenumber spectrum resulting from a $\cos^{2}\theta$ directionality for all wavenumbers is given in Fig. 5.11.

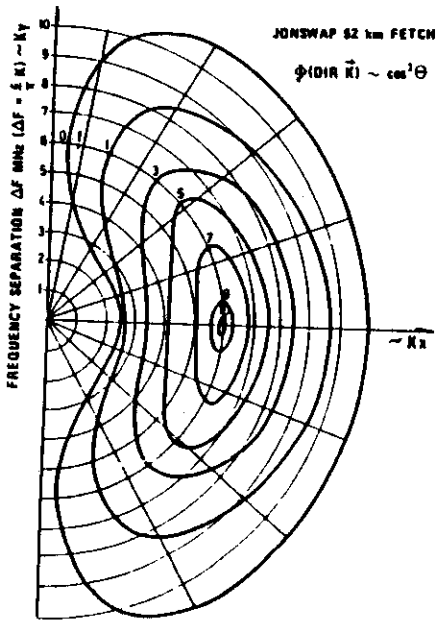

Fig. 5.11 Complex wave spectrum based on a $\cos^{2}\theta$ angular distribution and a JONSWAP one-dimensional spectrum.

The statement on angular spread in relation to ocean wavelength can be motivated as follows:

1) Long wavelength waves have a distant origin resulting from low attenuation. The larger the distance in relation to the 'source area' the more directional the wave. It takes a long fetch to produce a long wavelength.

2) Long waves once produced react slowly to changes in local wind direction.

3) Short waves are produced at short ranges. Changes in the direction of local wind field have a strong influence on the short ocean waves.

4) Waves interacting with a local wind field give rise to a patchy gust pattern superimposed on the wave pattern. This 'fossilized turbulence footprint' (Bretherton 1969, Woods 1969 , Lumley 1967) is likely to give rise to incoherent motion as distinct from the well-behaved gravity waves. The symmetry axis of the wind gust pattern is likely to be centered on the direction of the mean wind. This does not necessarily coincide locally with the direction of the ocean waves.

A local wind field may, through shear mechanisms, break up the coherency of the ocean wave ridge. The effect of this is to widen the angular distribution of the backscattered radar wave considerably, as illustrated in Fig. 5.12.

It is well known from turbulence theory that the nearness of a rough boundary, such as the sea surface, results in a low wavenumber suppression of the turbulence field and, also, to anisotropy (see, for example, Panovsky and McCormick 1960). Furthermore, any keen observer will have seen the modulation of the sea surface by the wind turbulence. If there had been no wave structure on the sea surface one would expect

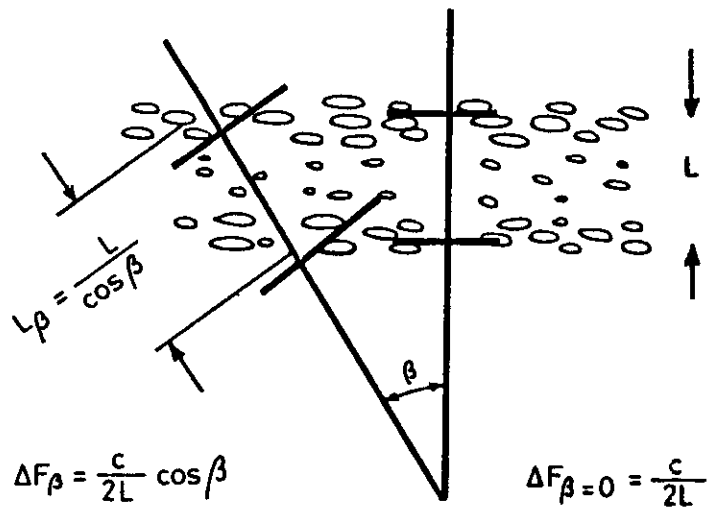

Fig. 5.12 Scattering from turbulent irregularities caused by the "footprint" of a local wind field interacting with the wave structure of the sea. (Gjessing, Hjelmstad 1986).

the footprint of the wind field to give rise to an anisotropic irregularity structure on the sea surface with an axis of symmetry determined by the direction of the local mean wird (Gjessing 1962). The presence of a wave structure on the sea surface will also modulate the wind field and seek to produce a sea-surface irregularity pattern with an axis of symmetry coinciding with that of the direction of the dominant wave spectrum. One would expect these factors to give rise to an incoherent irregularity structure on the sea surface with the 'axis of symmetry' along a direction somewhere between the direction of mean wind and that of the most energetic ocean waves (Gjessing 1962, 1964). This is illustrated in Figs. 5.13 and 5.14.

Here we have assumed that the wave crests and troughs are broken up by turbulence and wave braking phenomena such that there is no 'phase matching' between radio wave and ocean wave over the illuminated area, contrary to the coherent case depicted in Fig. 5.6.

Thus, when turning the antennas an azimuth angle β, the radio wave sees a dominating ocean irregularity scale which is increased from L when β=0 to

$$L_\beta = \frac{L}{\cos\beta}$$

This is illustrated in Fig. 5.12. Note that for certain values of K (and the corresponding ΔF) the back-scattered radio signal will increase with increasing azimuth angle symmetrically on either side of the β=0 direction, see Fig. 5.13. For experimental verification, the reader is referred to Figs. 5.30 and 5.32.

This phenomenon is illustrated in Fig. 5.14 where the angular relationship above is plotted assuming the following $\Phi(|K|)$ relationships: The wavenumber spectrum can be approximated by two power laws. On the low wavenumber side of maximum intensity it can be expressed by a K^m relationship, and on the high wavenumber side as a K^{-n} relationship. It is well known from turbulence theory that the nearness of a rough boundary such as the sea surface results in a low wavenumber suppression of the turbulence field and also in anisotropy (see e.g. H Panovsky et al. 1960). (Modulation of the sea surface by the wind turbulence, anisotropic irregularity structure on

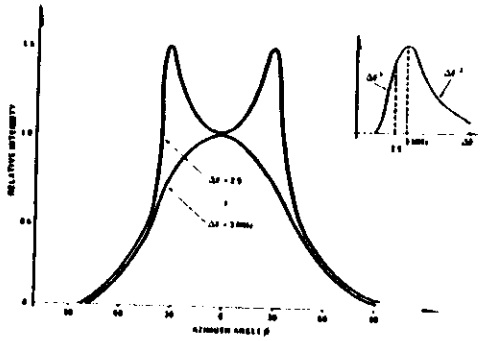

Fig. 5.13 Scattering from turbulent irregularities is expected to give a two-lobed angular response for frequencies below the spectral peak. (Gjessing, Hjelmstad 1986).

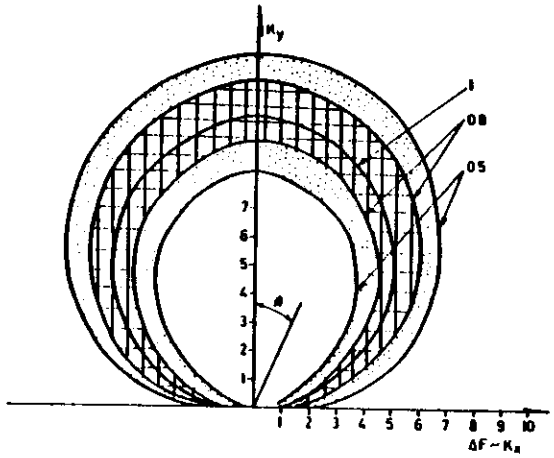

Fig. 5.14 Directional wavenumber plot of scattering from turbulent irregularities. (Gjessing, Hjelmstad 1986).

the sea surface with an axis of symmetry determined by the direction of the local mean wind (Gjessing 1962). In the case of a wide footprint (large coherence distance along the wave crest) the directional pattern will, obviously, be the same as in the coherent case.

5.3.1 The multifrequency radar principle, frequency difference matching

Up to this point we have been dealing with electromagnetic waves having wavelengths which are comparable with the irregularity scale of the scattering surface. We saw that by illuminating a surface with an electromagnetic wave having wavenumber $K=4\pi/\lambda$ we obtain information about the scattering structure at a scale $L = 2\pi/K$. This means that we are directly matching the radio wavenumber $\vec{K}$ to the Fourier component with wavenumber $2\vec{K}$ of the scattering surface. Thus, if we are to investigate ocean wave phenomena of scale, say 100 m, we should use a radio frequency of 1.5 MHz. However, in order to resolve the angular distribution of such waves with a resolution of, say 10^{o} (see Fig. 5.7), we need an antenna aperture of some 1200 m. This, obviously, represents some practical difficulties.

We now investigate what information can be obtained by matching some beat patterns (difference frequency) to the irregularity scales of the sea surface. Fig. 5.1 illustrates the physics of the problem. For this ΔK matching scheme to work (see, for example, Plant 1977), the scattering surface must have irregularities which contribute to the delay function $f(z)$ for scales corresponding to the difference wavenumber ΔK. To illustrate this, consider the following example. We illuminate the sea surface with a pulsed radar. The pulse length should be short compared with the gravity wave structure and long in comparison to the radio wavelength λ. We measure the detailed shape of the return pulse (voltage V as a function of time τ). The function $V(c\tau)$ gives us, directly, the delay function $f(z)$. If the gravity wave structure shows up on the delay function $f(z)$, i.e. if the spectrum of $f(z)$ has Fourier components matching the wavenumber ΔK, we would experience a radar return at the beat frequency $\Delta\omega = c\Delta K$.

There are many ostensible explanations for this 'modulation' of the small-scale structure (to which the wavenumber $\vec{F}$ is matched) by the long wave phenomena (to which ΔK is matched) (see, for example, Plant 1977, Plant and Schuler 1980, Clifford and Barrick 1978, Jones et al. 1981, Weissman et al. 1977 and 1982, Valenzuela 1978 a and b, Weight et al. 1980).

1) It is well known that the scattering cross-section of a surface increases with incidence angle. This means that from a sinusoidal gravity wave we get maximum low angle return at the point of maximum slope, i.e. from the inflection points where the second derivative is zero.

2) The turbulent intensity is governed by damping factors such as shear forces (Woods 1969 a,b, Luley 1969).

   Orbital motion within the wave structure changes the velocity shear periodically in phase with the gravity wave.

3) Shadowing effects may enhance the patchiness of the radar illumination and strengthen the apparent modulation effect of the gravity waves (Bass and Fuks 1979).

4) When the radius of curvature of the wave surface is the same as the distance from the radar to the scattering region in question, we may experience focusing (Gjessing 1964, Gjessing and Irgens 1964).

Breaking waves and white capping resulting from the local wind field, etc. complicates the issue still further.

In this presentation on the physics of electromagnetic interaction mechanisms, we make no attempt to resolve the question of scattering cross-section (delay function f(z)) in relation to waveheight in a quantitative manner. We constrain ourselves to giving qualitative results and note that empirical relations and also promising theoretical models are about to become available (see, for example, Valenzuela 1978, Plant 1977, Schuler 1978).

Note that there is nothing new about the characterization of scattering surfaces by bandwidth measurements. As early as in 1961 such measurements were performed by Alan Waterman at Stanford University, see e.g. Waterman, Gjessing and Liston (1961). Pioneers in this field are also Crawford, Hogg and Kummer from Bell's Research Lab (1959). The Stanford group, as well as that from Bell's, focused their attention on wave-phenomena in the troposphere superimposed on which there are also incoherent turbulence much in the same way as for the ocean surface with coherent gravity waves and capillary waves with turbulence. This problem was also addressed by Tor Hagfors as early as in 1959. His approach is indeed very analogous with the current one. Instead of investigating the scattering properties of a sea surface consisting of small scale "incoherent" irregularities riding on large scale wave phenomena, Hagfors studied the layered/turbulent structure of the ionosphere from below making use of the bandwidth properties of the scattering medium (Hagfors 1959). A very similar technique was used by Hagfors of Stanford University to measure the topography of the lunar surface (Hagfors 1961). Here the "delay spectrum"

was deduced from measurement of the correlation function in the frequency domain. See also Ishimaru (1978) and Tatarsky (1961). Conceptually, therefore, the problem of ΔK matching to the sea surface is very straight-forward and does not require a sophisticated consideration on capillary resonance phenomena. Any scattering surface such as a plowed field having irregularities of scale K coupling to the carrier electromagnetic wave and also scales ΔK coupling to the beat frequency wave lends itself to multifrequency investigations (ΔK matching).

For this ΔK matching scheme to work, the scattering surface obviously must have irregularities which contribute to the delay function $f(z)$ for scales corresponding to the difference wavenumber ΔK. If the gravity wave structure shows up in the delay function $f(z)$, i.e. if the spectrum of $f(z)$ has Fourier components matching the wavenumber ΔK, we would experience a radar return at the beat frequency $\Delta\omega = c\Delta K$.

As an illustration emphasizing the physics of the problem, consider the following question which currently is being addressed by the authors' organization. One is looking for a method by which a forest of Norway spruce can be characterized by the multifrequency matched illumination method. The planted spruce forest consists of a grid of trees. There are many dominating scales like on the sea surface to which K and ΔK shall have to be coupled.

Obviously a carrier frequency should be chosen so as to give resonant coupling to the needle dipoles. The length distribution of the ensemble of needles is very narrow and centered round approximately 20 mm. For these to act as efficient dipoles, the carrier frequency should be approximately 7.5 GHz. (To couple to a Scotch pine, the carrier frequency should be approximately 3 GHz). Then the branch of the spruce tree consists of sub shoots which typically are 8 cm long whereas the length of the branch itself could be 1 meter and the vertical spacing of branches something like 1/2 meter.

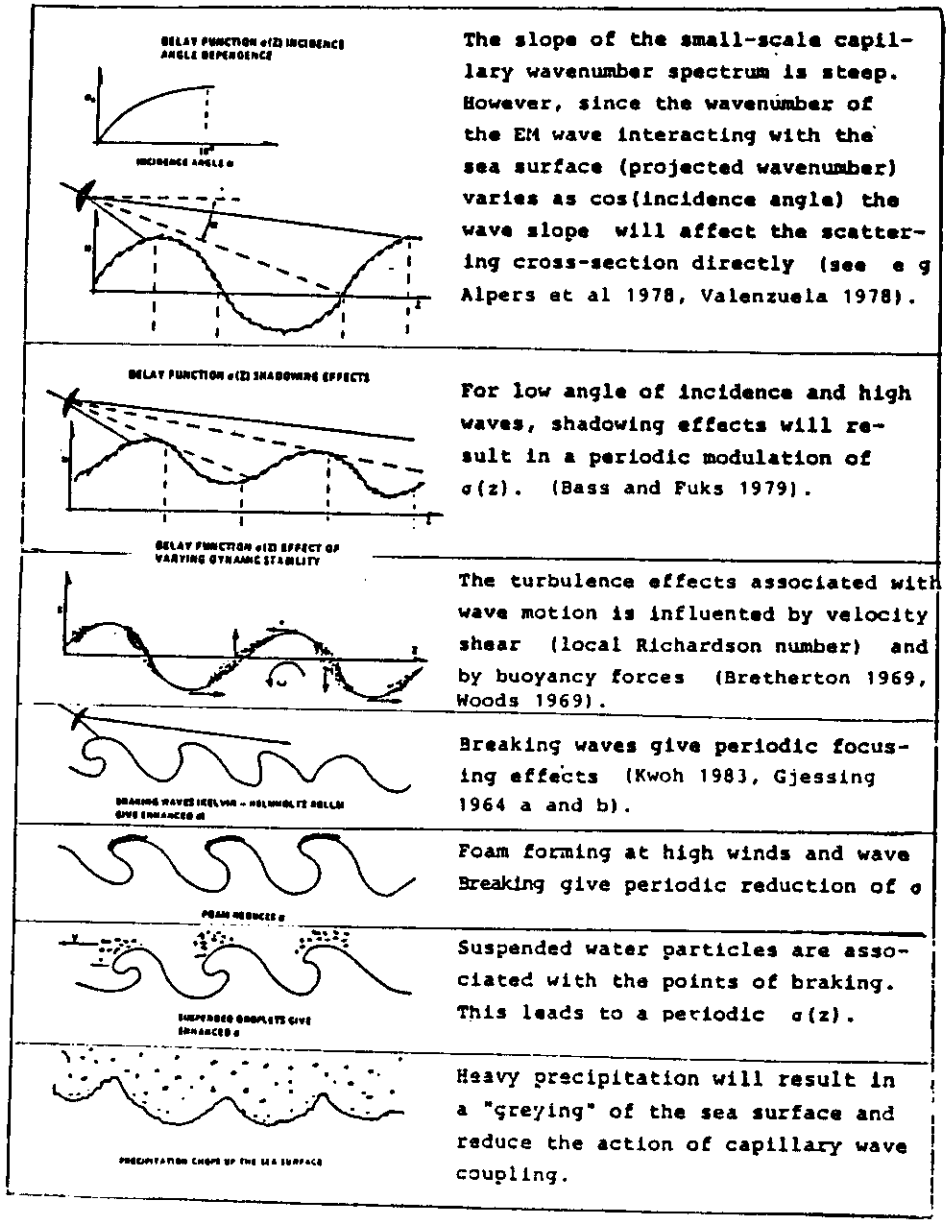

Fig. 5.15 Various mechanisms giving a periodic distribution of scattering cross-section with range, which is controlled by the dynamics of the sea.

If the interest now is limited to the measurement of the distances between the rows of trees (typically 2-5 meters) we should use a carrier frequency of 7.5 GHz and difference frequencies in the range from 30 - 75 MHz. The antennas should as in the case of the sea investigation be directed nearly horizontally and in an azimuth direction which corresponds to the direction where the distance distribution is sought.

In this context, obviously, it is not meaningful to use the term "modulation transfer function", neither is it perhaps appropriate to refer to "Bragg scattering".

The mathematics of difference frequency matching are given in section 2.1.

Before bringing this section on matched illumination in relation to ocean waves to an end, it may serve a purpose to present a very brief overview of other powerful techniques for sea surface radar investigations. The more important of these techniques are illustrated in Figs. 5.16 - 5.18. (See also Jackson 1980, Alpers et al, 1979).

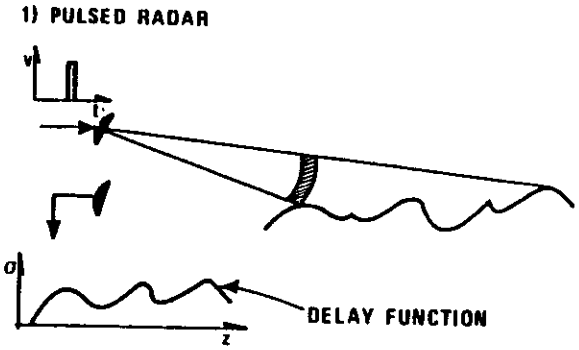

Fig. 5.16 A conventional pulsed radar measures the distribution in range of scattering cross-section as a "snap shot" (i.e. one realization of a statistical ensemble) if the pulse width is small compared with the ocean wavelength. Poor azimuthal (angular) resolution. Using a coherent radar with a stationary resolution cell small compared to the wavelength, improved directional resolution can be achieved (see Fig. 5.21).

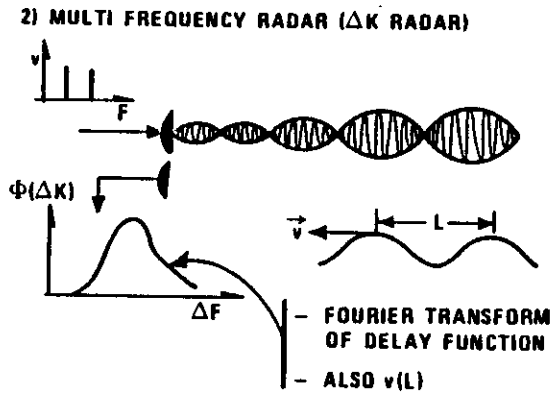

Fig. 5.17 The multifrequency radar measures the statistical properties of the sea surface by measuring the Fourier transform of the delay function $\sigma(z)$. This provides information about ocean wave spectrum $\Phi(\vec{K})$ and also about the distribution of wave velocity as a function of wavelength. Good angular resolution.

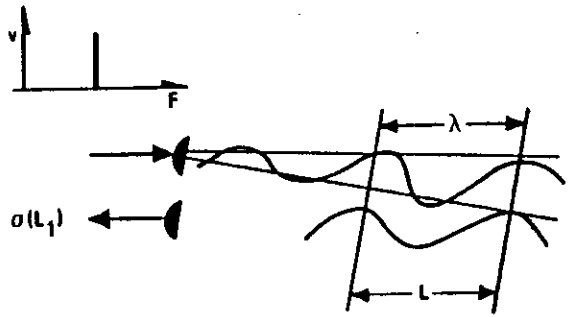

Fig. 5.18 Using an HF radar, direct constructive interaction between EM wave and ocean wave can be achieved. Measuring the Doppler shift information about wave direction can be obtained on the basis of knowledge about wave dispersion relationship. Varying the EM frequency over the appropriate frequency band, $\sigma(L)$ can be obtained. Poor angular resolution.

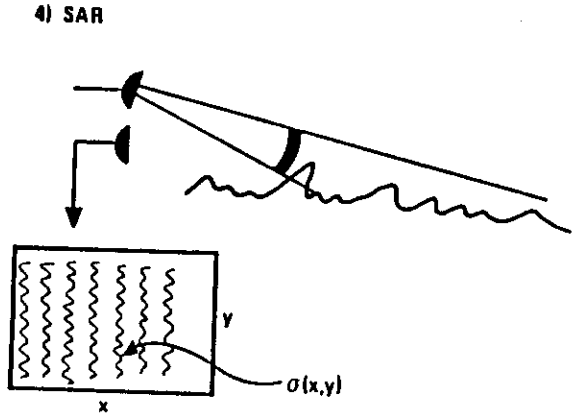

Fig. 5.19 Synthetic aperture radar SAR is based on a short pulse (FM chirp, pulse compression technique, etc.) for range resolution. For azimuthal resolution the principle of synthetic aperture is made use of. This involves the measurement of amplitude and phase as the flying radar sweeps its beam over the scattering surface.

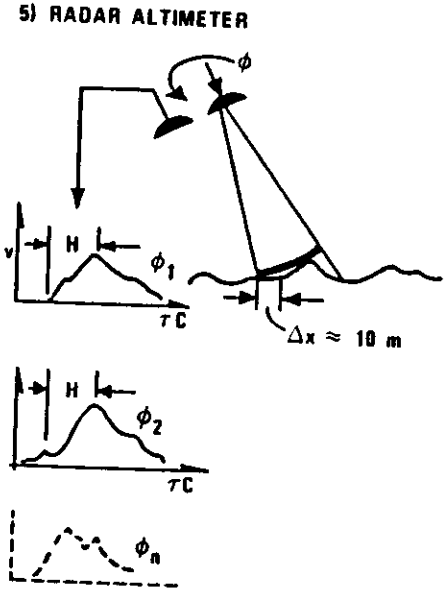

Fig. 5.20 Radar altimeter makes use of a short pulse. Measuring the rise and fall time of the back-scattered pulse pattern as the pointing direction of the antenna beam is changed, direct information about wave height and wave direction is achieved. Note that this experiment does not require information about the relationship between wave height and scattering cross-section (ref Welsh 1979).

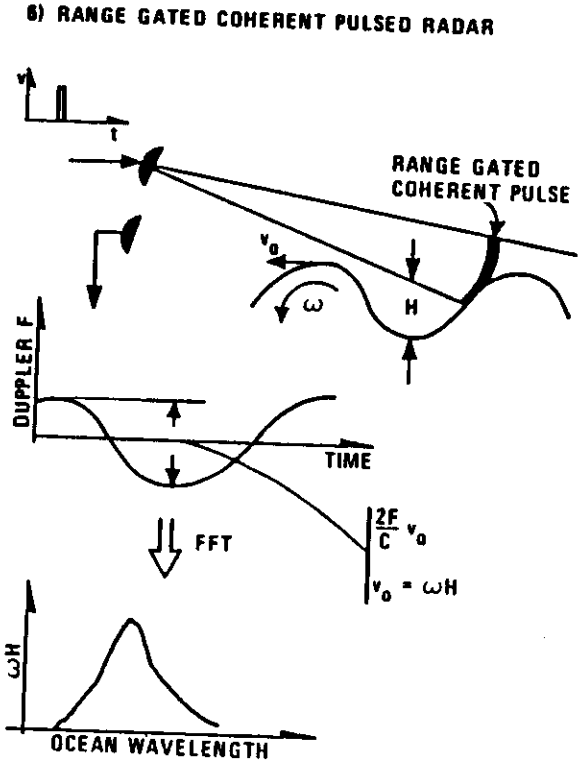

Fig. 5.21 Range-gated coherent pulsed radar involves a pulse to pulse coherent transmitter. Measuring the frequency modulation as a function of time of the backscattered signal, the orbital velocity is obtained through Doppler considerations when the pulse width is small compared with the ocean wavelength. Since the phase velocity $v = \omega H$ information about wave height is obtained under ideal sea conditions.
(Grønlie, Brodtkorb, Wøien 1984).

In summing up this section on the characterization of sea surface by modern radar methods, table 5.1 may serve a purpose.

B) OCEAN SURFACE (GRAVITY WAVES, INTERNAL WAVES, WIND PATTERN, SHIP WAKES)

	ADAPTIVE MULTI-FREQUENCY	PULSE COMPRESSION	CHIRP FM/CW	SAR
1-D SPECTRUM $A(\vec{K})$	YES	YES	YES	YES
2-D SPECTRUM $A(\vec{K},\omega)$ SPACE/TIME	YES	YES	NO	NO
2-D SPECTRUM $A(\vec{K})$ 2-D SPACE	YES	LIMITED	LIMITED	YES
3-D SPECTRUM $A(\vec{K},\omega)$ VELOCITY SPECTRA AS A FUNCTION OF SCALE SIZE (COHERENT/NONCOHERENT)	YES	NO	NO	NO
MATCHED ILLUMINATION FOR SPECIFIC WAKES • DIRECTIONAL SPECTRA FOR NON DISPERSIVE PHENOMENA • DIRECTIONAL SPECTRA FOR DISPERSIVE WAVES	YES	NO	NO	NO
SPACE/TIME COHERENCE FOR DIFFERENT SCALES	YES	NO	NO	NO

Table 5.1 Characterization of ocean surface (gravity waves, internal waves, wind pattern, ship wakes). The relative potential of modern radar systems.

5.3.2 Some illustrative experimental examples

Having laid the basis for an understanding of the principles involved in relation to the coupling of electromagnetic waves to ocean waves (ΔK coupling) some illustrating example may strengthen our physical understanding. Before we presen the experimental arrangements and give some illustrative experimental results, however, it is of importance to perfor some simple calculations so as to have some idea of what to expect from the experiments.

Basing our calculations more on the expression for Doppler shift given earlier (see section 5.1)

$$f = \sqrt{\frac{2\Delta F}{\pi C}} \qquad (5.17)$$

and on the familiar JONSWAP spectrum for ocean waves referred to above, we can calculate the Doppler shift and spectral intensity associated with each radio frequency pair subject to the assumption that we know the relationship between scattering cross-section and waveheight. Fig. 5.22 relates with the multifrequency radar concept. We select a given ΔF_1 (which is the same as selecting a given irregularity scale L_1), and we measure how the frequency covariance function

$$R(\Delta F_1, t) = V(F,t)V^*((F+\Delta F_1),t)$$

is varying with time t. We then compute the power spectrum of the frequency covariance function $R(\Delta F_1, t)$. This means, as depicted in Fig. 5.22, that we apply a Fourier transformation of the $R(\Delta F_1, t)$ function with respect to time t so as to obtain the Doppler spectrum. If, then, the ordered gravit waves dominate over the incoherent velocity components which ride on the gravity waves, we would expect the Doppler spectrum to have a maximum at the frequency corresponding to the dispersion relation of gravity waves (eq. (5.17)), and we would expect a Doppler broadening determined by the velocity spread δV. Hence, the Doppler broadening Δf is given by

$$\Delta f = \frac{2\Delta F}{c} \cdot \delta V \qquad (5.18)$$

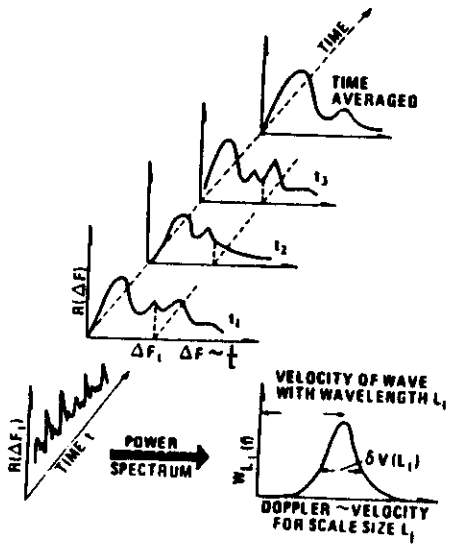

Fig. 5.22 By studying the temporal variation of the frequency covariance function $R(\Delta F)$ for a given frequency ΔF_1 (scale size $L_1 = c\ 2\Delta F_1$) we derive information about the motion pattern (Doppler) of the irregularity scale L_1 (Gjessing 1978).

The detailed signal analysis procedure is shown in Fig. 5.23.

The following calculations will be based on the JONSWAP experimental results shown in Fig. 5.5 above. Knowing from this figure the ocean wave-height spectra in the conventional time domain, it remains, before we can calculate the radar signature, to convert the temporal spectra to spatial spectra, applying the relationships given in section 5.1 (frequency $f = \sqrt{\frac{g}{2\pi L}}$ where L is the ocean wavelength).

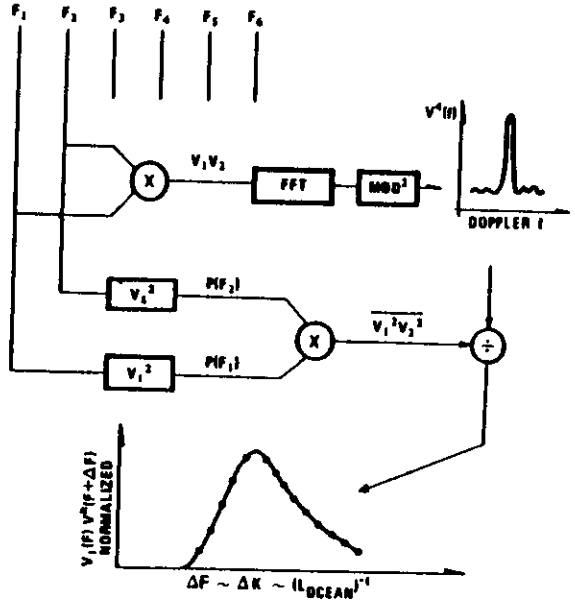

Fig. 5.23 Multiplying the various combinations of the six frequencies, 15 values of ΔK are obtained, coupling to 15 ocean scales. Thus we get information about the motion pattern of 15 ocean scales (coherent and incoherent components) and we also get information about the scattering cross-section through the Fourier transform of the delay function $\sigma(z)$. The spectra are normalized as indicated in the figure.

Thus the frequency axis of Fig. 5.5 showing the JONSWAP spectra is converted directly to a beat frequency ΔF axis by the relationship

$$f = \sqrt{\frac{g\Delta F}{\pi c}}$$

This is shown in Fig. 5.24.

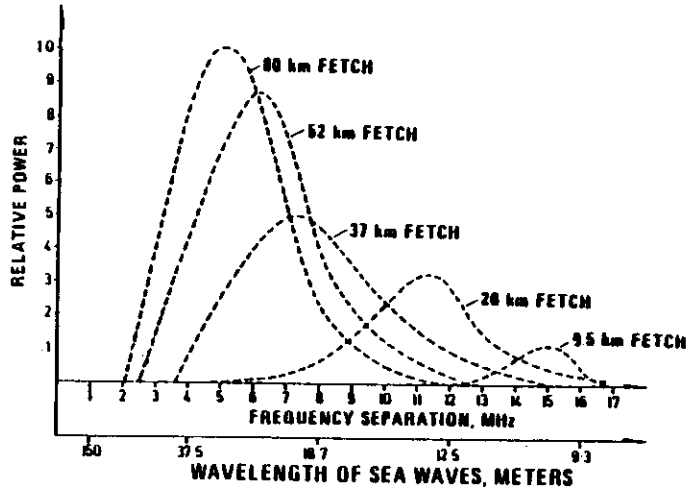

Fig. 5.24 ΔK signature of the ocean surface based on the JONSWAP experiments of Fig. 5.5. Note that the relative power (wave height) axis is in arbitrary units. There is not necessarily a linear relationship between waveheight and the measured radio quantity given in Fig. 5.23 $V(F)V^*(F+\Delta F)$. (Gjessing 1981 © IEEE).

Then finally, let us present some illustrative experimental results.

A. Directional ocean wave spectra observed from the NASA Electra aircraft

Illuminating the sea surface by a fixed 14^o beamwidth side-looking antenna pointing 10^o downwards relative to the horizontal plane, the ocean wave spectra were determined for various azimuth directions and for 15 different ocean wavelengths in the interval from some 16 m (couples to F = 8 MHz to 300 m (corresponding to $\Delta F = 1/2$ MHz). For each frequency separation ΔF the frequency covariance function $V(F,tV^*(F+\Delta F,t)$ was computed.

The NASA Electra operated north-east of Wallops Flight Facility (38.49.2 N - 74.24 W) at an altitude of 12 000 ft, January 20, 1983, time 2203Z.

Banking the aircraft 10^o so that the antennas were pointing at a depression angle of 20^o, the aircraft completed a 360^o circle. In this way the antenna was illuminating essentially the same area on the sea surface at all azimuth directions. The longitudinal dimension of the footprint is approximately 5600 m, whereas the transverse dimension is approximately 2000 m.

Flying in a closed circle, the frequency covariance function $V(F)V^*(F+\Delta F)$ was computed for 15 different values of ΔF for all azimuth angles. The results are shown in Fig. 5.25. Note that the Bragg angle is clearly visible for the longer wavelengths (215 - 88 m).

In terms of aircraft altitude H, depression angle α and antenna beamwidth $\Delta\beta$ we get the following expression for the Bragg angle

$$\beta = \frac{L}{2H} \frac{\sin\alpha}{\sin(\frac{\Delta\beta}{2})}$$

This is presented in Fig. 5.26. Note the good agreement between theory and experimental results.

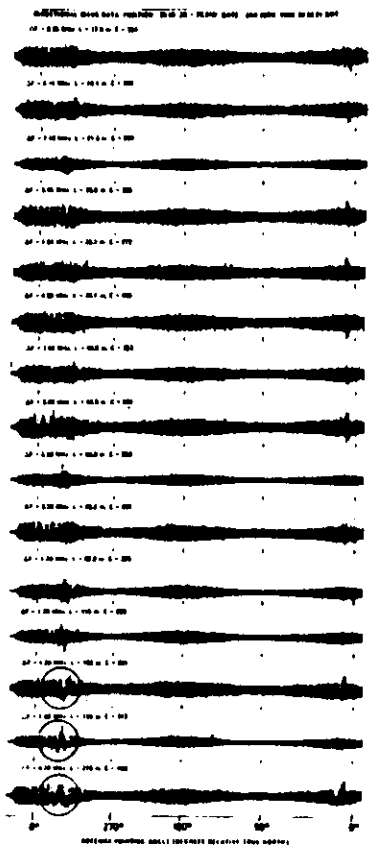

Fig. 5.25 The aircraft flew in a closed circle pointing the antennas 30° down from 12 000 ft. The covariance function $V(F)V^{*}(F+\Delta F)$ is shown for 15 different values of ΔF. (Gjessing and Hjelmstad 1986).

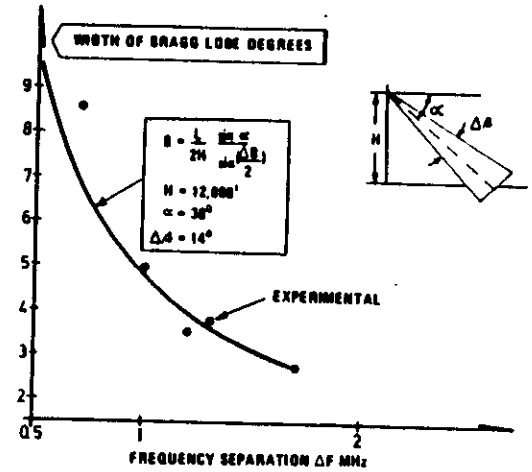

Fig. 5.26 The measurement of Bragg angle is compared with theory. Note that the aircraft altitude is 2 000 ft, depression angle 30° and beamwidth 14°. (Gjessing and Hjelmstad 1986).

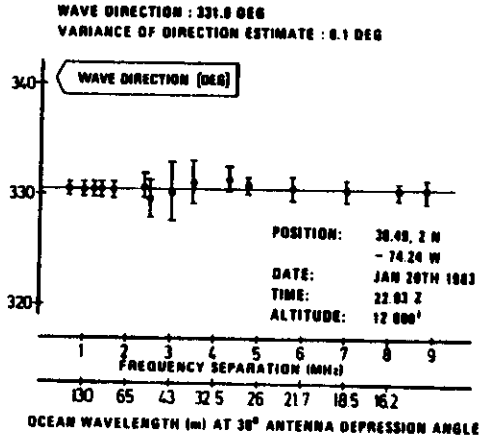

Fig. 5.27 Wave direction plotted as a function of wavelength. (Gjessing and Hjelmstad 1986).

Noting the two azimuth angles corresponding to destructive interference on either side of the wave direction, this can be determined with great precision as shown in Fig. 5.27.

Finally, for an azimuth direction corresponding to that of the propagation direction of the ocean waves, the distribution with wavelength of the scattering cross-section is computed. This is shown in Fig. 5.28. Note that two wavelengths dominate, 130 m and 18 m.

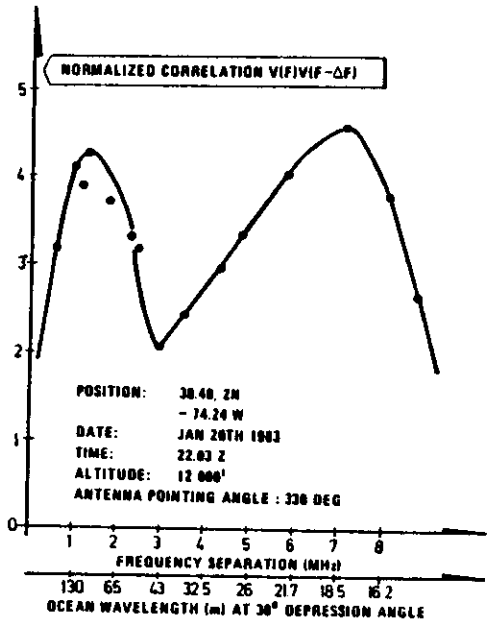

Fig. 5.28 There are two dominating wavelengths, 130 m and 18 m.

B. Directional spectra obtained from ground-based station on a cliff

The complex field strength was recorded over a period of some 12 minutes before the azimuth angle was changed, thus obtaining a plot of power spectral density and Doppler spectrum as a function of frequency separation (ocean wavelength). A typical result is shown in Fig. 5.29.

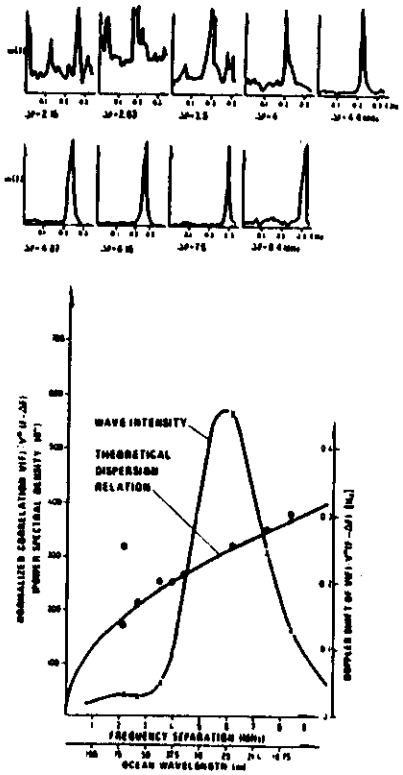

Fig. 5.29 Spectra of wavelength and wave velocity. Note that wavelengths shorter than that corresponding to the spectral peak move at constant velocity. This is not the case for longer scales. The results are from Langesund March 12,1981 at 1030 local time, the azimuth direction being 135°. (Gjessing et al. 1985).

First, consider the results obtained on March 12, 1981 (1010 - 1235 local time). The weather and sea state can be characterized as follows:

- Wind direction 90^{o} (East)
- Wind speed approximately 8 m/s
- Wave height 1.4 m peak to peak
- Waverider gives maximum wave height for f = 0.225 Hz
- Wind decreasing at noon, turning northerly. Wave height reduces to 1 m peak to peak, choppy sea

Fig. 5.29 shows the wave intensity for a particular azimuth direction and also the Doppler spectra associated with various scale sizes. Note the very well defined spectral peak in the intensity versus wavelength distribution. Note also that the Doppler frequency is in very good agreement with the theoretical dispersion relation. There seems to be a slight, but consistent, displacement to higher Doppler frequency. This is a result of an inward current.

Finally, in Fig. 5.30 we present the two-dimensional irregularity spectrum summing up the description of the sea-surface structure. Here we have plotted the isolines of spectral intensity, or more specifically the quantity $V(F)V^{*}(F+\Delta F)/V(F)^{2}$, in the K_x-K_y plane. This presentation should be compared with those of Figs. 5.10, 5.11 and 5.12. Note also that the isolines of spectral intensity $\Phi(\Delta\vec{K})$ are obtained directly from a set of one-dimensional spectra such as those shown in Fig. 5.29.

As will be seen, we distinguish between coherent and incoherent components. With "coherent component" we refer to the dominant Doppler spectral line caused by the "coherent" gravity wave ($f = \sqrt{\frac{g\Delta F}{\pi c}}$).

The incoherent component is the "residue intensity" of the Doppler spectrum (the contribution from the skirts) obtained

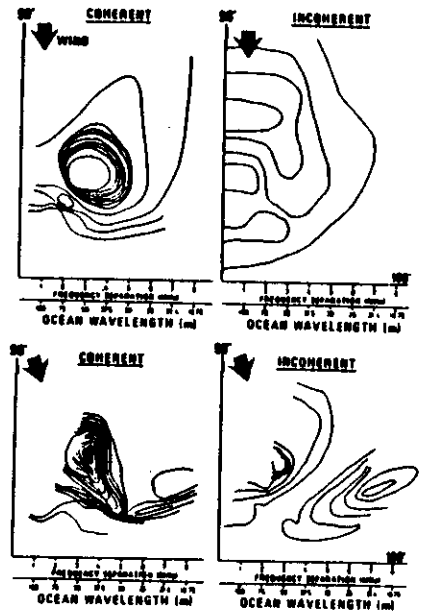

Fig. 5.30 Isolines of spectral intensity $\Phi(\Delta\vec{K})$ in the K_x-K_y plane. Note the effect of changes in wind direction on the coherent irregularity spectrum. Note that the upper set of maps was obtained on March 12, 1981, 1010 to 1135 local time, whereas the lower set refers to the situation during the time interval 1135 to 1235. (See also Gjessing, Hjelmstad, Lund 1985).

when the coherent contribution wave is subtracted. It can be visualized as all the random turbulent velocity contributions outside the short velocity interval dominated by the gravity wave. Note, however, that although the velocities of the scatterers vary widely as seen e.g. from Fig. 5.31, the difference frequency ΔF selects a narrower range of irregularity scales centered around the scale size L given by

$$L = \frac{c}{2\Delta F}$$

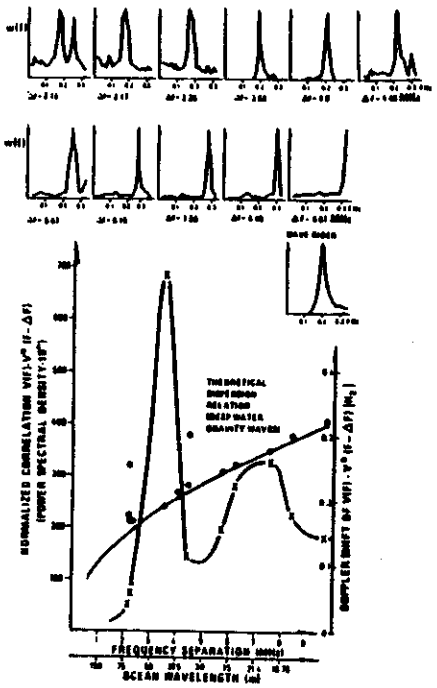

Fig. 5.31 Spatial and temporal wave spectra for an azimuth direction of 140°. Location is Langesundsfjorden, time is March 18, 1981, 1525 local time.

If these weak incoherent irregularities were entirely due to the local wind field, one would expect the local wind direction to provide an axis of symmetry. Unfortunately, the antenna systems were not flexible enough to be turned beyond the east direction ($\theta = 90^{\circ}$). It is therefore difficult to establish such a symmetry. The coherent contribution, however, has a pronounced axis of symmetry determined by the direction of the most energetic ocean wave. We see that the angular distribution is far from $\cos^2\theta$ distributed, long waves are more plane than the shorter ones, as suggested in Fig. 5.11.

The lower set of directional spectra in Fig. 5.30 gives the situation one hour later when the wind has turned from east towards north. We see that the most energetic waves (the "eye" of the isoplot chart) have not changed direction, whereas the shorter scales and weaker disturbances are re-oriented slightly. The distribution of the incoherent (turbulent) irregularities is drastically altered.

On March 18, 1981 there is no wind before noon. At 1330 the wind speed is 10 m/s from south, bringing the water height up to 2.5 m. The complex K plot shows a unidirectional spectrum.

Two hours later, when the wave height has increased to 2.5 m peak to peak and wind has turned easterly, the irregularity structure is very much altered. This most striking feature has (as indicated in Fig. 5.31 and also summarized in Fig. 5.32) the very pronounced appearance of a second peak at a wavelength of 25 m whereas the dominating spectral peak is still 50 m. Note that this two-peak spatial spectrum for a particular azimuth direction is not very pronounced in the waverider spectrum. This, presumably is a result of the omni-directional response pattern of the waverider. Note also that Fig. 5.31 shows a very pronounced two-peak structure in the Doppler spectrum for an ocean wavelength of some 70 m. Finally, Fig. 5.32 sums up the results of the afternoon run in the form of $\Phi(\Delta\vec{K})$ isolines for the coherent as well as for the incoherent components. Note that the wavelength corresponding to peak spectral intensity varies with azimuth angle.

For details regarding sea-surface signatures in relation to the matched illuminator concept, the reader is referred to refs Gjessing, Hjelmstad, Lund 1985 and Gjessing, Hjelmstad 1986.

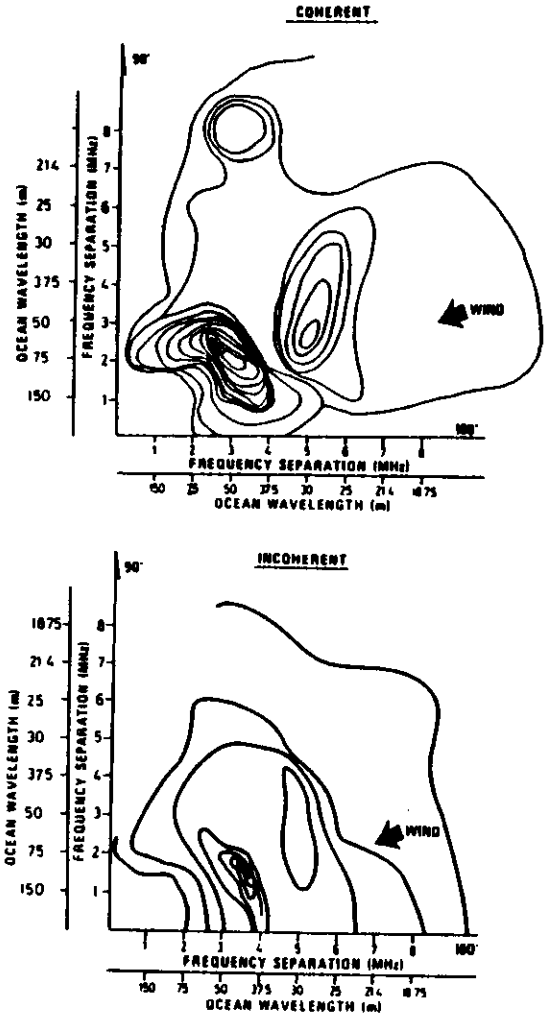

Fig. 5.32 The two-dimensional ocean irregularity spectrum (isolines of $\Phi(\Delta\vec{K})$) when the wave height has increased to 2.5 m peak to peak and the wind has turned towards east.

Before ending this section on illustrating examples in relation to the sea surface, it may be of interest to compare our experimental results with earlier findings of theoretical and experimental nature. Fig. 5.33 serves this purpose. Here we have plotted a JONSWAP (Hasselmann et al. 1973) for a 52 km fetch with a result obtained on March 13, 1981 using the multifrequency radar. We can see from this comparison that there is a good general agreement.

Here it is important to note, as pointed out earlier, that no attempts have been made to convert our normalized spectral intensity to a quantity that provides direct information about wave height. The relation between our normalized spectral intensity and waveheight squared per hertz is not likely to be a linear one, neither is it likely to be invariant for varying conditions of whitecapping (splash), foam formations, etc. Therefore, all that Fig. 5.33 can tell us is that the spectral wave intensity distributions observed by Hasselmann et al. are similar to those observed by our multifrequency radar system.

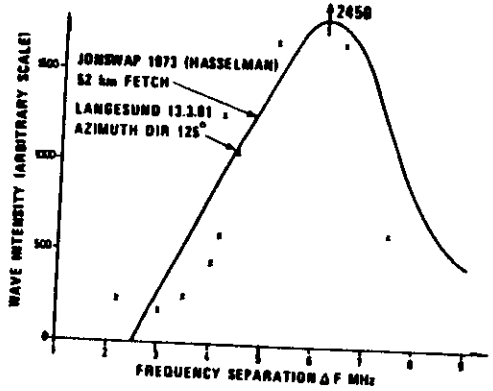

Fig. 5.33 A typical result from the multifrequency radar experiment is compared with the "classical" JONSWAP experiment (Langesundsfjorden March 12, 1981, 12.15).

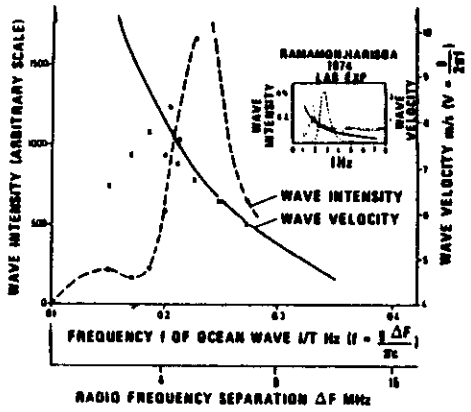

Fig. 5.34 Wind-tunnel experiments of Ramamonjiarisoa (1974) are compared with the results from multifrequency radar experiments (Langesundsfjorden, March 12, 1981). (Gjessing, Hjelmstad 1986).

Wind wave-tunnel measurements by Ramamonjiarisoa (1975) show a remarkable drop in phase velocity of ocean waves with wavenumber (oscillation frequency), smaller than that corresponding to maximum spectral intensity. In Fig. 5.34 these results are compared with radar experiments. Note the close resemblance between the wind-tunnel results and those obtained by the radar. Near the spectral peak, the measured phase velocities lie close to the dispersion relation for freely travelling gravity waves. Phillips (1969, p.157) attributes the marked deviation from the dispersion line for low wavenumbers to distrubances associated with groups of the more energetic waves travelling with the appropriate group velocity. (See also Phillips 1957).

This brings the section on ocean signatures to an end. We shall now approach the more complex problem of providing matched illumination for a target in the form of a rigid ship against an ocean background. This will be the topic of Chapter 6.

HYDROSPHERIC DIAGNOSTICS

Electromagnetic interaction phenomena involving molecular resonance giving rise to distortion

by

Dag T Gjessing

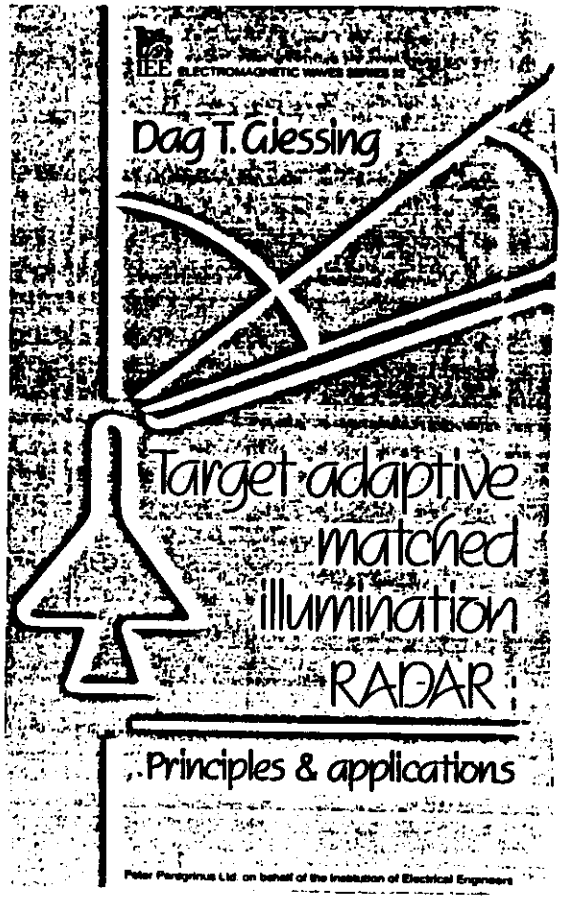

2.6 Influence of absorbing surfaces; molecular resonance phenomena. Illumination matched to the surface material composition.

Up to this point we have confined our attention to macro-scale phenomena, to resonance phenomena brought about by the interaction between electromagnetic waves and geometrical structures. These principles rely on the imaginary term in the scattering matrix; we have not considered molecular resonance phenomena giving rise to absorption.

It is not within the scope of this book to consider molecular resonance phenomena in any degree of detail. However, for the sake of completeness, and for the sake of forming the basis for a comprehensive understanding of potential mechanisms involved when electromagnetic waves are scattered from a surface, a brief high-lighting of the subject may prove appropriate.

In addition to completing the scattering picture, it is believed that the current section will illustrate in a rather simple way the principle of matched illumination. This is in particular the case since we are dealing with a scalar quantity rather than as hitherto the four-dimensional space-time problem.

First, let us dwell shortly on the fundamentals of surface spectroscopy (see e.g. Eckert et al. 1974).

When we discussed methods by which the geometrical shape of an object could be determined remotely, we relied on the back-scattering capability of the object. In order to determine the material composition, we shall rely on the capability of the object to absorb electromagnetic waves. Specifically, we select an illuminating wavelength which stimulates resonance phenomena in the molecular surface structure of the object. Hitting one of the resonance frequencies causes the material to absorb electromagnetic

waves. Noting the frequency at which electromagnetic energy is absorbed, and also the amount of absorbed energy, gives us information about the absorption spectrum which reveals the molecular composition of the material. Having at our disposal electromagnetic waves in the range from microwaves through infrared waves and visible light to the ultraviolet region, gives us the capability of determining a large number of material compositions.

Consider as an example a diatomic molecule within which potential forces are acting; the atoms are bound together by elastic forces as illustrated in Fig. 2.37. If these atoms, having finite mass, are excited by an alternating electromagnetic field, resonance will occur when the stimulating frequency equals that corresponding to the difference between two quantised vibrational energy levels. We can consider these two atoms, with masses m_1 and m_2, as being tied together by forces that can be represented as a ball and spring system where the restoring force obeys Hooke's law. The frequency of this simple harmonic oscillating ball and spring system is given by

$$\nu_o = (1/2\pi)(K/\mu)^{\frac{1}{2}}$$

where K is the spring constant in Hooke's law and μ is the reduced mass, $m_1m_2/(m_1+m_2)$. By considering the energy which is being absorbed, we obtain

$$E_v = (v+\tfrac{1}{2})(h/2\pi)(K/\mu)^{\frac{1}{2}}$$

where $v(=0,1,2,3\ldots)$ is the vibrational quantum number.

The above example applies for two atoms. A complex molecule will have a large number of oscillating modes leading to numerous energy levels. Still, if we know the detailed structure of the molecule of interest, we can in principle calculate the absorption spectrum. Also, if we have access to the material of interest, which is generally the case,

then the absorption spectrum can be obtained experimentally. In both cases we have information about the "fingerprint", and thus know what to look for. We shall now discuss methods by which chemical substances of known molecular structure (absorption spectrum) can be detected and identified selectively.

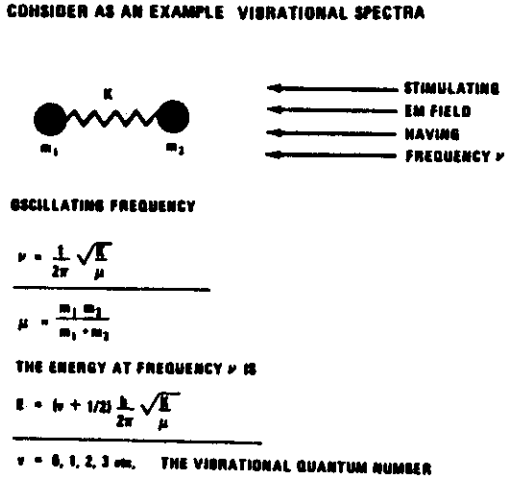

Fig. 2.37 An electromagnetic wave can stimulate resonance phenomena in molecules when the appropriate frequency is chosen.

We see that as a result of molecular resonance phenomena, the electromagnetic wave impinging on a scattering and lossy surface will suffer frequency selective absorption. These will be superimposed on the bandwidth limitations imposed by the multipath phenomena (shape and size of scattering object) discussed earlier. If one mechanism is wide- or narrow-banded in relation to the other, we have nc conceptual or practical difficulties. The difficulties arise when the width of the molecular absorption lines are comparable with the bandwidth limitations caused by the geometric shape of the scattering body ($\Delta F = \frac{c}{2L}$ where L is the size of the object).

Now, in order to illustrate the essential points and the potentials of surface spectroscopy techniques, let us define a challenging problem of practical importance, using it as an example. Our aim is to detect and identify a particular chemical agent, for example some sulfate deposited on vegetation in a certain geographical area. This could be an area contaminated from human activity or by deposits from general air pollution. A priori this agent may have its fingerprint (absorption lines) in any wavelength region from the ultraviolet region (λ = 0.2 - 0.4 μm) through the infrared region (2 - 20 μm) to the millimeter and microwave region (λ = 100 - 200 μm).

To reveal these fingerprints, we illuminate the ground on which this agent may be present with electromagnetic waves, changing the frequency over the frequency band of interest in some predescribed manner that is optimum with regard to the detection and identification of the particular chemical compound of interest. The situation is assumed to be as follows:

- We are looking solely for a specific chemical compcund.
- We know the absorption spectrum or reflectance spectrum of this compound.
- We know nothing about any of the other agents (interferents) that may be present.

- We have very meager information about the vegetation (topography) on which the agents may be deposited, but we have some general idea about the roughness of the structure (grass, coniferous trees, rocky ground). Let us assume that the background is coniferous trees.

A hypothetical detection system will be discussed for the purpose of illustrating the essential points. Figure 2.38, which is sub-divided into two sections, shows a remote probing system in symbolic form. Section A has a generator G providing the illumination. It illuminates an area on which contaminated trees are growing. The contaminating agent is assumed to be deposited over the area, which is viewed by two receivers having two separate not overlapping fields of view. When the frequency of the illuminator is changed in a linear manner (saw-tooth frequency modulation) and the signals V_1 and V_2, which are received at the two receivers, are observed (referring to the symbolic diagram of Figure 2.38), the signals have the following components:

- A random signal with large variance (Rayleigh distributed) resulting from the topography. The signal is a result of

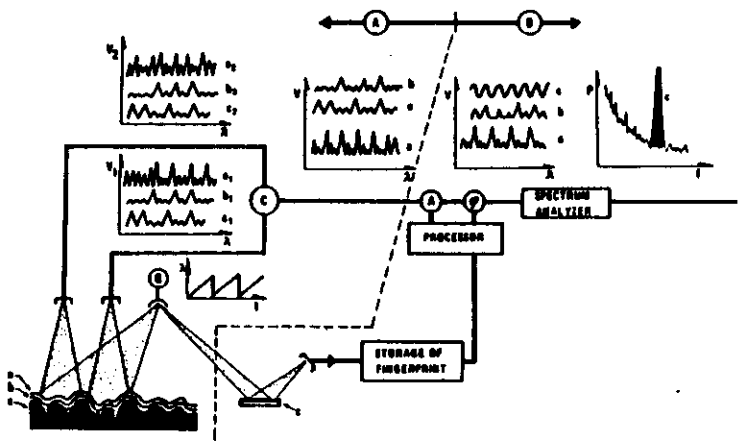

Fig. 2.38 Symbolic diagram illustrating the optimum detection and identification principle. (Gjessing 1978a).

backscatter from scattering facets distributed in depth. They give rise to many interfering waves and result in large variations in field strength with frequency (signal trace marked "a").

- A deterministic signal component resulting from the complex surface chemistry (trace marked "b") appearing as modulation of the random topography signal.

- Deeply imbedded in the background chemistry is the component of interest, namely that stemming from the absorption spectrum of the particular chemical compound of interest (trace marked "c").

Our first task in the signal enrichment process is to reduce the dominating effect of the topography (traces a_1 and a_2). In order to achieve this, we shall make use of knowledge we already have about the signal (the deterministic molecular absorption spectrum) and about the noise (the random signal resulting from scattering from a random surface such as from a tree). The noise resulting from the scattering process will obviously be statistical in nature, and there will be no correlation between the signals at the two receivers if the vegetation within the two separate fields of view is not identical in form. Furthermore, if the scatterers (the branches of the trees) move only a fraction of a wavelength from one frequency scan to the next, the correlation from one frame to another at either receiver will be limited. Since the turbulence scale (i.e. the spatial correlation distance) of the surface wind causing the vegetation to move is small compared with the height of the vegetation, the above assumptions are justified.

Therefore our task is to find a process by which the uncorrelated noise component can be reduced relative to the correlated signal component. This is done in the correlator marked C in Figure 2.36. To ensure a thorough physical understanding of the statistical signal retrieval methods involved, this process will be discussed in some detail.

First let us consider the case where the two contributions are added together (additive noise). Figure 2.39 gives a

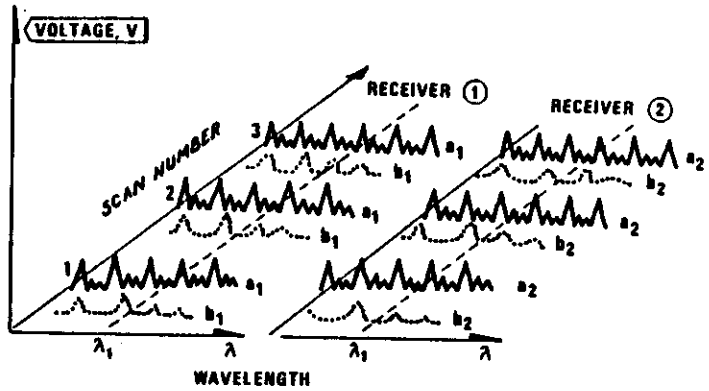

Fig. 2.39 Data forming the basis for signal enhancement by a correlation process.

plot in three dimensions of the data that form the basis for the correlation process. Consider the signals from receiver No.1 first. In our cartesian coordinate system the signal strength is plotted vertically, wavelength is plotted horizontally in the plane of the paper, and the frame-number (or scan number) is plotted orthogonally to the V-λ plane. The signal resulting from the deterministic absorption spectrum is denoted "b" as in Figure 2.39 and the random signal stemming from the vegetation is denoted "a". To reduce the effect of the random uncorrelated contribution, we form an ensemble covariance function for each value of λ, by comparing (correlating) $V(\lambda_1)$ from each scan. Thus we will obtain a number of points on the covariance function determined by the number of frames (scans) and we will obtain a number of covariance functions determined by the wavelength resolution $\Delta\lambda$. If our ensemble then is N, our signal-to-noise ratio is enhanced by a factor $\sqrt{N}$.

However, the simple example with additive noise (addition of coherent and non-coherent components of the signal) is probably not the most realistic one. For example, if the coherent signal appears as an amplitude modulation on the incoherent signal, then it would be more meaningful to cross-

correlate the spectral components of the signals from the two receivers by forming the coherence function instead of the covariance in the C processor.

In order to express this mathematically, we shall use an approach based on work by Kjelaas, Nordal and Bjerkestrand 1977). In the general case we may have both multiplicative and additive noise. If the spectral components of the noise are hot overlapping those of the signal, a simple filtering technique can be employed. If the spectral components do overlap, we shall have to use methods that give us an optimum signal-to-noise ratio. First let us consider the case of additive noise.

If then $S(t)$ be the signal and $n(t)$ the noise, the resultant

$$F(t) = S(t) + n(t)$$

We then assume that there is no correlation between $S(t)$ and $n(t)$. The cross-covariance R_{fs} between the resultant signal f and the signal s is given by

$$R_{fs} = R_{(s+n)s}(t) = R_s(t) + R_{ns}(t) = R_s(t)$$

Similarly the autocovariance is

$$R_f(t) = R_{s+n}(t) = R_s(t) + R_n(t)$$

This can be written in the form

$$[R_s(t) + R_n(t)] \times h(t) = R_f(t)$$

where the symbol $\times$ denotes convolution and $h(t)$ is therefore the impulse response. The transfer function $H(\omega)$, which is the Fourier transform of the $h(t)$ function, is then given by

$$H(\omega) = \frac{P_s(\omega)}{P_s(\omega) + P_n(\omega)} = \frac{P_s(\omega)}{P_f(\omega)}$$

where $P(\omega)$ is the power spectrum so that $P(\omega)$ is the Fourier transform of the autocorrelation function $R(t)$.

Let us consider the case of a multiplicative noise source. The resultant signal may be written as

$$f(t) = S(t) \times h_n(t)$$

and

$$R_f(t) \times h_n(t) = R_{fs}(t)$$

which in terms of the transfer function gives

$$H(\omega) = \frac{R_{fs}(\omega)}{R_f(\omega)}$$

We can now express the transfer function $H(\omega)$ in terms of the coherence

$$coh_{sf}(\omega) = \frac{P_{sf}(\omega)}{P_s(\omega)\ P_f(\omega)}$$

where $P_{sf}(\omega)$ is the cross-spectrum and the transfer function is given by

$$H(\omega) = \frac{P_{sf}(\omega)}{P_f(\omega)}$$

$$= \frac{coh_{sf}(\omega)\ P_s(\omega)\ P_f(\omega)}{P_f(\omega)}$$

$$= P_s(\omega)\ coh_{sf}(\omega)$$

Thus, if we are dealing with additive uncorrelated noise, the signal-to-noise ratio is enhanced by forming the covariance function as implied in the discussion of Fig. 2.38. The operator C in Fig. 2.38 is a correlator giving us the ensemble covariance function. If, however, the noise is multiplicative, we shall have to cross-correlate the spectral components by forming the coherence function.

Concluding the discussion of section A in the symbolic Figure 2.38, we note that the uncorrelated effects of the rough scattering surface are suppressed during the correlation process. All the correlated factors, chemical compound of interest deeply imbedded in all the uninteresting molecular structures, are retained in unaltered proportions. How let us proceed to section B of the diagram.

This section illustrates a method by which we can make use of the detailed information that we possess about the chemical compound of interest (molecular structure, reflectance spectrum) to perform a selective detection:

- The signal preprocessed in section A is "filtered" with the fingerprint (reflectance spectrum) of the chemical compound of interest. In the symbolic diagram of Fig. 2.38 this is achieved by shining part of the energy from the illuminator onto a reflector containing a film of the chemical agent on which we are focusing our attention. The resulting reflectance spectrum contains the fingerprints that give us the basis for the second filtering operation.

- The operation involves a structuring of the original frequency sweep so as to limit the frequency content of the signal resulting from the chemical agent of interest to a delta function in the frequency domain (i.e. to a pure sinusoidal variation in time over the sweep period). In a practical system one would accomplish this by sweeping the transmitter frequency (the illuminator) in a particular manner (not with a saw-tooth as depicted in the schematic diagram above) and at the same time and in synchronism with the frequency sweeping, amplitude modulate the illuminator (see Figs. 2.40 and 2.41).

To illustrate this principle and its merits, let us assume that the ♦ and A operators of Fig. 2.38 is a tape re-

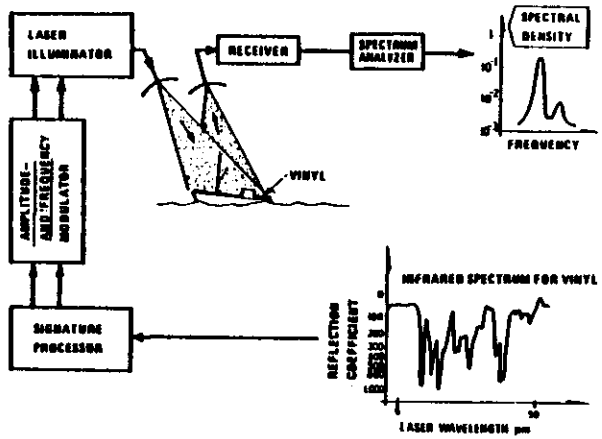

Fig. 2.40 The illumination can be tailored to achieve optimum system sensitivity with minimum interference if detailed information about the absorption spectrum of the chemical compound of interest is available.

corder. The signal is played into the tape recorder in real time and played off successively. The first operator, the "A function", involves an amplitude modulation of the signal so as to adjust the lines of the reflectance spectrum related to the agent of interest to the same level. This involves an amplitude modulation of the reflectance spectrum of interest. The second signal from the processor (the ♦ operator) adjusts the speed of the tape to obtain constant spacing between the lines in the reflectance spectrum of interest. If the interval in the wavelength domain is large between two lines, the tape should be speeded up; conversely, if the distance is small the speed should be slowed. In this manner all the characteristic spectral lines will be equally spaced when originating from the chemical compound of interest and distributed in a disordered manner for all the interferents.

In principle, adjusting both the frequency and the amplitude of the generator illuminating the target of interest in great detail, can transform the signal component originating from our particular chemical compound to a pure sine wave requiring a scan-time limited bandwidth to be detected. In this manner the signal-to-noise level of our system can, in principle, be brought to a very high level. Limiting factors are determined by the available integration time and the degree to which it is practicable to structure the illumination function.

Finally, the basic Figure 2.41 shows the result of a final Fourier analysis of the signal. Our signal of interest is concentrated to a very narrow spectral region, whereas the effect of the interferents is distributed over the spectrum. Before we proceed to consider in some greater detail the character of the noise to be suppressed, we shall give a more realistic example of a selective detection method. Such a method is illustrated schematically in Fig. 2.40.

The illumination (microwaves, IR, visible light, UV) is amplitude and frequency modulated by particular waveforms (see Fig. 2.41). These waveforms are the result of a detailed processing of the molecular signatures (see Fig. 2.40). The processed illumination is then transmitted to the object of interest. Since the illumination is matched to the molecular structure of interest, the signal appearing at the receivers has minimum information bandwidth and the bandwidth of the entire receiving system can be minimized. Minimum bandwidth gives minimum noise contribution. (Gjessing 1978a).

Fig. 2.41 illustrates the A and ϕ operation process. In the top curve of Fig. 2.41 an idealized molecular spectrum is shown (spectrum of absorption, emission or reflectance). The reflectance Γ varies in a triangular manner with wavelength. If the illuminator is linearly frequency modulated, this is what the signal would look like. Amplitude modulat-

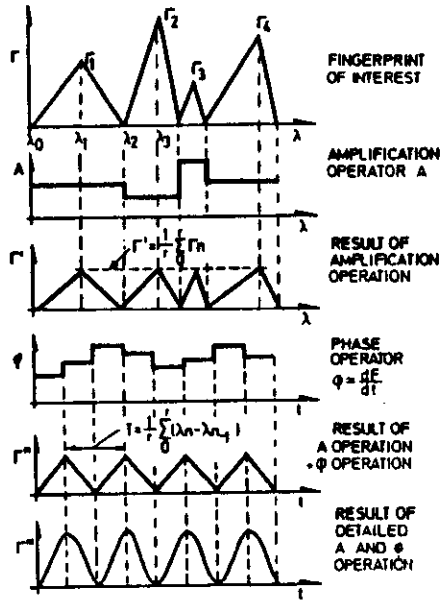

Fig. 2.41 Example of an optimum structuring of the illumination function for the purpose of detecting/identifying a particular molecular structure. (Gjessing 1978a).

ing the illuminator in a manner illustrated in Fig. 2.41, second curve from above, seeking the same strength of all the lines in the reflectance spectrum, gives the results shown.

Referring now to the fourth curve from above, we change the relative position of the maxima and of the minima of the spectrum so as to obtain a periodic function shown in the fifth graphical representation. This is achieved by changing the rate dF/dt at which the frequency is changed. It is

then obvious that if a more detailed A and ♦ operation is applied, the result is a sinusoidal variation, shown at the bottom of Fig. 2.41. To detect this requires only a very small bandwidth.

For the purpose of emphasizing the merits of the technique, some illustrative examples are given in Fig. 2.42. Two different absorption spectra are considered. Type "A" is characterized by eight absorption lines, whereas type "B" has ten absorption lines. Each absorption line is Lorentz shaped.

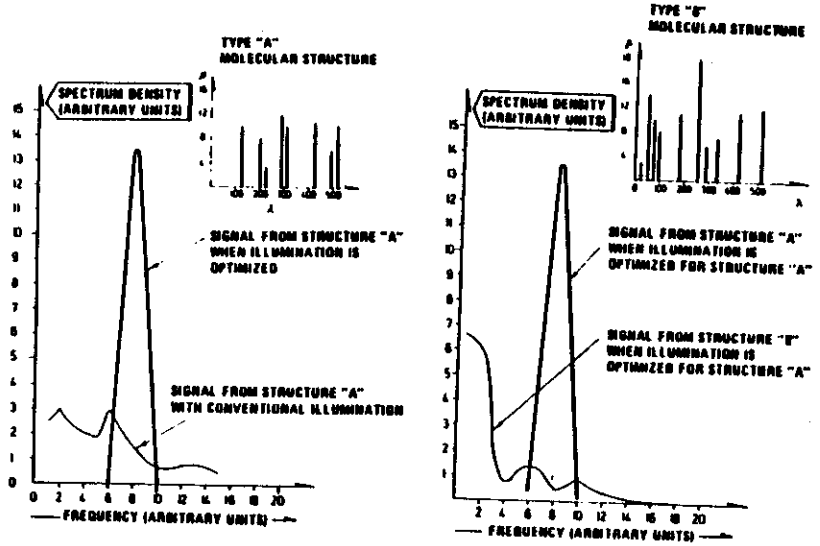

Fig. 2.42 The effect of optimized illumination: theoretical results. (Gjessing 1978a)

Adopting the amplitude- and frequency-modulation scheme illustrated in Fig. 2.41 above, the illumination is structured for type "A" molecules. Fig. 2.42 shows the result of this optimization process. Note that the spectrum density

function associated with optimized illumination is narrow, whereas the spectrum resulting from conventional illumination is wide. Also, if an extensive structuring of the illumination had been accomplished, the resulting signal spectrum would have been a delta function. Fig. 2.42 also shows the discriminating power of the technique (right-hand figure). Here an illumination structured for type "A" molecules is applied to structure "B". Note the marked difference in maximum spectral intensity and the shift in frequency of the peaks.

If a computer simulation program implementing this crude technique that involves "first-order matching" only for three frequently encountered compounds, namely epoxy, vinyl and biphinyl, is used, the result is Fig. 2.43. Note that by

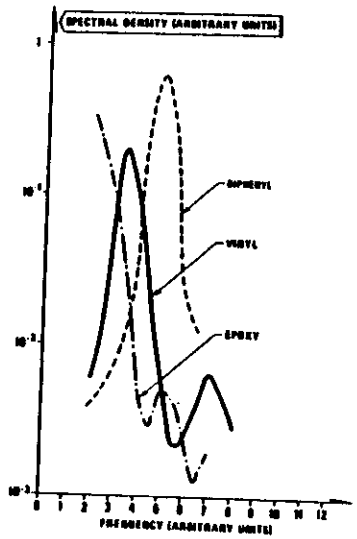

Fig. 2.43 The effect of matched illumination for epoxy, vinyl and biphenyl. The illumination that has been structured for vinyl is applied to epoxy. Similarly, the curve for biphenyl is obtained by structuring the illumination for biphenyl. Computer simulations.

the use of narrow filters as depicted in Fig. 2.40 above, the particular agent of interest can be selected when its absorption spectrum is known.

Let us now express this mathematically. On the basis of information about the absorption spectrum, we search the expression for the manner in which the frequency should be varied so as to give a sinusoidal variation of the received (reflected) signal. This we refer to as matched illumination.

For a linear frequency scan, the frequency as a function of time is given by

$$\omega = \omega_1 t' + \omega_0$$

where ω_1 and ω_0 are constants.

If $f(\omega)$ is the reflection/absorption spectrum, applying linear scanning we have

$$f(\omega) = f(\omega_1 t' + \omega_0)$$

We now want a modified sweep function giving us a periodic output function. Hence, we wish to obtain

$$f(\omega_1 t' + \omega_0) = \hat{f}(t') = g(t)$$

where $g(t)$ is our periodic function. This can be achieved by inverting the $f(t')$ function. Thus, the function should satisfy the condition

$$f^{-1}\hat{f}(t') = t' = f^{-1}[g(t)]$$

Therefore, in order to match the illumination to the agent of interest, a frequency sweep function $f^{-1}(\omega)$, which is the inverse of the reflection/absorption spectrum $f(\omega)$, should be used.

An example will clarify this. Let the absorption spectrum be of an exponential form

$$f(\omega) = e^{-a\omega} = g(t)$$

$$f^{-1}[f(\omega)] \rightarrow \omega = -\frac{1}{a} \ln g(t)$$

$$\omega(t) = -\omega_1 \frac{1}{a} \ln g(t) + \omega_0$$

Having given the general expression for the matched illumination function in terms of functions describing the material of interest, we shall go on to consider the effect of the topography (the surface roughness) in relation to that of surface chemistry. The question we now ask is: how should the transmitting/receiving system be structured in order to give maximum information about the geometrical shape of an object? Or, how should the system be structured to have optimum sensitivity in relation to a given object of known size and shape.

This will be the topic of the subsequent sections.

HYDROSPHERIC DIAGNOSTICS

Atmospheric diagnostic methods involving microwaves

by

Dag T Gjessing

Royal Norwegian Council for Scientific and Industrial Research
Environmental Surveillance Technology Programme

and

University of Tromsö
Institute of Mathematical and Physical Sciences

Radio Science, Volume 4, Number 12, pages 1195–1201, December 1969

Atmospheric structure deduced from forward-scatter wave propagation experiments

Dag T. Gjessing

Norwegian Defense Research Establishment, 2007 Kjeller, Norway

(Received August 6, 1969.)

This review is concerned with the relative potentials of various experimental radio techniques from the point of view of determining the atmospheric fine-scale structure. After having derived a unified set of simple approximate expressions for the 'measured quantity' in terms of parameters describing the refractive-index time-space structure, some of the more important sources of error are discussed. Finally, on the basis of numerous experimental results, the form of the refractive-index spectrum is deduced by using the previously derived theoretical expressions.

1. INTRODUCTION

It is the object of this survey to analyze the results from various transhorizon scattering experiments for the purpose of deducing the fine-scale properties of the refractive-index structure. To justify a comparison of the ensemble of deduced results, it is essential that the set of equations that form the basis for the deductions be based on the same theoretical concept.

During the past decade we have seen a whole spectrum of theories ostensibly explaining the phenomena encountered in any one given scatter experiment. When deducing the refractive-index structure from different experimental techniques for the purpose of comparing the deduced results, it is undesirable to have different theories forming the basis the various deductions. Consequently, in this ·ey the appropriate theoretical relationships are derived in a unified manner from knowledge about the refractive-index structure. Specifically, we express the refractive-index spectrum in the form $\Phi(K) \sim K^{-n}$, and we derive expressions relating the 'measured quantity' (such as field strength correlation distance, bandwidth, delay spectrum, and antenna-to-medium coupling loss) in terms of the exponent n and the appropriate geometrical and electromagnetic quantities. This unified treatment of the scatter-propagation problem enables us to compare the n values deduced from the various experiments.

It will be seen that some experimental techniques give a 'measured quantity' that is strongly dependent on n and weakly dependent on sources of error such as refraction effects, whereas for other techniques the converse is the case. Thus some n deductions have a high level of confidence, whereas others in many cases have an inadequate confidence level. It seems to be of great value to have this information about confidence level when discussing the shape of the refractive-index structure in relation to the dynamics of the atmosphere.

2. ANGULAR SCATTERED POWER SPECTRUM IN RELATION TO REFRACTIVE-INDEX STRUCTURE

Consider a volume element $dv = dx\,dy\,dz = d^3r$ within the scattering volume V, this scattering volume being confined to the spatial region in the troposphere illuminated by the transmitting antenna and 'seen' by the receiving antenna. If the permittivity (refractive index squared) within the elementary volume differs by an amount $\Delta\epsilon$ from the average value of the permittivity ϵ_0, the element of dielectric becomes polarized, giving rise to a dipole moment $d\mathbf{P} = \Delta\epsilon\,dv\,\mathbf{E}_0$ when under the influence of an electric field $\mathbf{E}_0$. At distance R from the scattering element the dipole moment results in a polarization potential $d\pi$ and provided $k^2\pi \gg \nabla\nabla\cdot\pi$ (which requires $R \gg V^{1/3}$), the scattered field strength $\mathbf{E}_s = k^2\pi$, where k is the wave number of the electric field. The scattered field resulting from the integral of elementary scattering elements is then given by

$$\mathbf{E}_s = \frac{k^2}{4\pi R}\int \mathbf{E}_0 I(\mathbf{r}, t) e^{-i\mathbf{K}\cdot\mathbf{r}}\, d^3r \qquad (1)$$

where $\mathbf{K} = \mathbf{k}_s - \mathbf{k}_i$, $\mathbf{k}_s$ and $\mathbf{k}_i$ being the wave numbers of the incident and the scattered fields, respectively,

such that $|\mathbf{K}| = (4\pi/\lambda)\sin\theta/2$, where θ, the scattering angle, is the angle between $\mathbf{k}_i$ and $\mathbf{k}_s$.

Note that (1), which is derived from Maxwell's equation, is perfectly general and does not consider the nature of the refractive-index irregularities described by the function $f_1(\mathbf{r}, t)$. This function may be a stochastic one, in which case the refractive-index field is conveniently described by the spatial autocorrelation function of refractive index, or we may be dealing with an ordered variation in ϵ, say a horizontal layer through which the refractive index varies in a systematic fashion expressible as a well-behaved function.

To ensure a thorough physical understanding of the problem, let us discuss (1) in some detail.

Case A: Let us first assume that the wave incident on the scattering volume is a plane one and that the linear extension of the scattering volume $V^{1/3}$ is very small compared with the distance from the transmitter to the scattering volume (and similarly small compared with the distance R from the scattering volume to the receiving antenna). This means that we must assume that the curvature of the wave front is large, such that the first Fresnel zone in a vertical plane normal to the transmission path is large compared with the linear extension of the scattering volume as measured in this plane. Under such conditions we can exclude the E_0 factor from the integrand of (1), the result being that the scattered field is simply the Fourier transform with respect to space of the $f_1(\mathbf{r})$ function. To obtain an expression for the angular power spectrum of the scattered wave, we shall have to multiply E_s by its complex conjugate, thus obtaining the scattering cross section σ given by

$$\sigma(\theta) = (\pi k^4/2)\Phi(\mathbf{K}) \qquad (2)$$

where $\Phi(\mathbf{K})$ is the spatial 'power spectrum' of the refractive-index irregularities such that $\Phi(\mathbf{K})$ is the Fourier transform of the spatial autocorrelation function of $f_1(\mathbf{r})$. The scattering cross section σ is defined as the mean power in the scattered wave per unit power density of the incident wave in the scattering volume, per unit solid angle in the direction of $\mathbf{k}_s$, per unit scattering volume.

Case B: Now let us consider the opposite case where the incident field E_0 varies far more rapidly with r than does the refractive index. In the extreme case we assume that $f_1(\mathbf{r})$ is a constant throughout the scattering volume. Equation 1 then takes the form

$$E_s = \epsilon \int_v E_0(r) e^{-i\mathbf{K}\cdot\mathbf{r}}\, d^3r \qquad (3)$$

which states that the diffraction field is the Fourier transform of the field strength distribution in the plane in which r is measured. For a symmetrical radio path this plane is the vertical cross-path plane illuminated by the transmitter and seen by the receiver.

In the general case, as already noted, (1) applies, so that the angular spectrum of scattered field strength is the Fourier transform of the product $E(\mathbf{r})\cdot f_1(\mathbf{r})$. It should be quite clear, then, from the foregoing arguments that $E(\mathbf{r})$ can only be excluded from the Fourier integral if the $E(\mathbf{r})$ function is 'wide' in comparison with the $f_1(\mathbf{r})$ function. Now let us consider these two functions in turn.

The 'width' of the $f_1(\mathbf{r})$ function is easily defined if we are dealing with a nonstochastic function, say a layer through which the refractive index varies systematically. The width of the $f_1(\mathbf{r})$ function is then simply the thickness of the layer. If we are dealing with a random function of $f_1(\mathbf{r})$, it seems clear that the width of the $f_1(\mathbf{r})$ function is comparable with the correlation distance L of the refractive-index field. Practical experiments show that L varies with time and position in space. A correlation distance of some 10 meters appears to be the right order of magnitude for L.

Then let us consider the 'width' of the $E(\mathbf{r})$ function. Here there are two factors that must be considered. If we are neglecting the influence of the irregular refractive-index structure on the phase front of the radio beam as this propagates from the transmitter to the common volume, the $E(\mathbf{r})$ function is determined entirely by the curvature of the phase front in the scattering volume, i.e., the 'width' of the $E(\mathbf{r})$ function is essentially the first Fresnel zone as measured in a vertical cross-path plane through the center of the scattering volume. If R_1 is the distance from the transmitter to this plane, then the diameter of the first Fresnel zone is given by

$$l = [(2R_1\lambda)]^{1/2}$$

where λ is the radio wavelength. For $\lambda = 5$ cm and $R_1 = 100$ km, the diameter of the first Fresnel zone is 100 meters. However, for the radio wave to reach the scattering volume, it will have to propagate through the refractive-index irregularities. Hence the phase front in the scattering volume is a perturbed one. In other words, superimposed on the spherical phase front with radius of curvature equal to R_1, we have random phase fluctuations resulting from the fact that the phase at a point P in the scattering volume is given by the refractive-index integral

$$2\pi/\lambda \int_r^r n(x)\, dx$$

where T is the transmitter, and dx a line element.

Introducing, then, the concept of 'phase coherence distance,' which is the distance measured in the vertical cross-path plane at distant R from the transmitter where the coherence is $1/e$, it can be shown [*Fried*, 1966] that the phase coherence distance is given by

$$\rho = (1.84/k^2RC_n^2)^{3/5}$$

where $k = 2\pi/\lambda$, and C_n^2 is Tatarski's scatter coefficient. By letting $\lambda = 5$ cm, $C_n^2 = 10^{-15}$, and $R = 100$ km, we find that the coherence distance is 10 meters. Consequently, the Fresnel zone does not constitute a limiting factor, and the $E(\mathbf{r})$ function is limited by the antenna beams.

In conclusion, therefore, we note that in general it is permissible to exclude the $E(\mathbf{r})$ term from the integrand. Hence, if we write the refractive-index spectrum (see equation 2) in the form $\phi(K) \sim K^{-n}$, the angular power spectrum of the scattered wave is given by $P(\theta) \sim \theta^{-n}$, when we assume an isotropic refractive-index field.

Although it has been made clear that the mathematical treatment is a general one that does not assume a particular atmospheric structure, it may be helpful to give some illustrative examples. Basing our mathematical treatment solely on the basic equation 1, we shall calculate the scattering cross section (the form of the $\Phi(K)$ spectrum) appropriate to three different plausible atmospheric conditions.

2.1. *Scattering by homogeneous isotropic turbulence*

The theory of small-scale turbulence developed by Kolmogorov, Oboukhov, and others and based on natural physical ideas, gives quite definite conclusions on the spatial spectra of air velocity fluctuations. A close relationship is also established between the spectrum of air velocity fluctuations and that of temperature and humidity. Since there is a simple relationship between refractive index N and temperature T and humidity e, the spatial refractive-index spectrum can be represented as a linear combination of the T and e spectra.

In the wave-number range (K range) corresponding to the inertial subrange, the refractive-index spectrum $E(K)$ can, according to turbulence theory, be written in the form

$$E(K) \sim \langle \delta\epsilon^2 \rangle_{av} l^{-2/3} K^{-5/3}$$

where $\langle \delta\epsilon^2 \rangle_{av}$ is the standard deviation of permittivity fluctuations, and l = input scale (i.e., $l = 2\pi/K_m$ where K_m is the wave number for maximum $E(K)$).

The spectrum $E(K)$ is the one-dimensional 'power' spectrum obtained from an integration of $\phi(\mathbf{K})$ over all directions of $\mathbf{K}$.

If the refractive-index field is isotropic, then $E(K) = 4\pi K^2\phi(\mathbf{K})$. In the inertial subrange we therefore have the following expression for the refractive-index spectrum:

$$\langle \delta\epsilon^2 \rangle_{av}\phi(K) = 0.03 C_n^2 K^{-11/3}$$

where $C_n^2 = 5.3\langle \delta\epsilon^2 \rangle_{av} l^{-2/3}$ as introduced by *Tatarski* [1961] on the basis of structure-function considerations.

The expression for the scattering cross section (see equation 2) then takes the form

$$\sigma = 0.03 C_n^2 \lambda^{-1/3} (\sin\theta/2)^{-11/3} \qquad (4)$$

Then let us consider the other extreme case where we are dealing with a layered atmospheric structure.

2.2. *Scattering from a layer through which the refractive index varies systematically*

To illustrate the principles involved, let us consider one horizontal layer through which the refractive index varies according to the function $f_1(z)$, where z is the vertical coordinate. Writing (1) as

$$E_s = (k^2 E_0/4\pi R) A(\mathbf{K})$$

we can express $A(\mathbf{K})$ as

$$A(\mathbf{K}) = \int_{-\infty} f_1(\mathbf{r}) \cdot \exp\left[-i(K_x x + K_y y + K_z z)\right] dx\, dy\, dz$$

But with a horizontal layer, $f_1(\mathbf{r})$ reduces to $f_1(z)$, the permittivity being constant in the x and y directions. Thus we have

$$A_1(\mathbf{K}) = \int_{-\infty} f_1(z) e^{-iK_z z}\, dz \int_{-\infty} e^{-iK_x x}\, dy \int_{-\infty} e^{-iK_y y}\, dx$$

The integrals having x and y arguments are immediately recognized as the Fourier integral representations of the Dirac delta function, so that this expression may be written

$$A(\mathbf{K}) = \left[\int_{-\infty} f_1(z) e^{-iK_z z}\, dz\right] \delta(K_y) \delta(K_x)$$

The function $A(\mathbf{K})$, and thus E_s, then vanishes unless both K_x and K_y are zero. Hence $A(\mathbf{K}) = 0$ unless $\mathbf{K}$ is normal to the layer boundary.

To obtain an expression for the scattering cross section, we form the product $A_1(K)A_1^*(K)$, obtaining

$$\sigma = \frac{\pi k^2}{2}\left|\int f_1(z)e^{-iKz}\,dz\right|^2 \qquad (5)$$

since $f_1(z)$ is a known real function.

The flat layer, however, constitutes the simplest, and most unrealistic, of the models involving systematic layers. To include the case of a rippled layer, we shall have to consider beam focusing effects, complicating the issue considerably [*Gjessing et al.*, 1964]. In this survey, however, this case will not be included. Now let us replace the smooth layer by a turbulent one.

Scattering from a turbulent layer

The turbulent layer to which we here refer is the case where the intense turbulence affecting radio wave propagation is confined to one or more strata of extremely limited vertical extent, as opposed to the case treated in section 2.1, where it was assumed that the scattering occurred within a great vertical depth of the atmosphere. A distinct difference between this type of layer and that just discussed is that when we are dealing with turbulent strata, the layer boundaries are not likely to be smooth (smooth in terms of radio wavelength). This means that mirror reflection as inferred in section 2.2 will not take place. Now, these atmospheric layers are generally associated with a large degree of local stability. Hence it is reasonable to expect the mean temperature and humidity, and hence also the mean refractive index, to vary in a systematic fashion through the layer. On this systematic refractive-index profile the random fluctuations of refractive index caused by turbulence are superimposed. Thus there are *two factors* contributing to the scattered radio power. One is the scattering from the mean profile (partial reflection), as discussed in section 2.2; the other is the scattering from the random refractivity fluctuations caused by turbulence. Since the two contributions to the scattered field bears a random phase relationship, the total resulting scatter field is obtained by simple summation. If, then, the random refractivity fluctuations obey the inertial subrange $K^{-11/3}$ law and if the mean refractive-index profile can be expressed by the function $f_1(z)$, where z is the vertical coordinate, the resultant scattering cross section is given by the sum of (4) and (5). Thus

$$\sigma_T = 0.03C_n^2\lambda^{-1/3}(\sin\theta/2)^{-11/3} + \frac{\pi k^2}{2}\left|\int f_1(z)e^{-iKz}\,dz\right|^2$$

The relative importance of the two terms of this equation depends on

a. the relative magnitude of the rms random refractivity fluctuations and the degree to which the mean refractive index varies through the layer,

b. the thickness of the layer in relation to the quantity $\lambda/\sin(\theta/2)$, and

c. the radio wavelength λ in relation to the input scale l of the turbulence field.

If the layer thickness L is comparable with the scale $2\pi/K$, which contributes to scattering at a particular wavelength λ and a particular scattering angle $\theta[K = (4\pi/\lambda)\sin\theta/2]$, then the layer has a pronounced effect on the scattered angular power spectrum. Accordingly, when we deduce the refractive-index spectrum $\Phi(K)$ from radio experiments, we may essentially be measuring the profile of the refractive index through layers. If, however, the layers are horizontal, they will only affect the scattering in a great-circle plane as we have seen from section 2.2. By performing an experiment where we vary the orientation in space of the plane in which scattering takes place, i.e. vary the direction of $\mathbf{K}$, it is possible to measure the extent to which horizontal strata contribute to the deduced $\Phi(K)$ spectrum [*Gjessing*, 1962; *Bolgiano*, 1963; *Gjessing*, 1964*b*; *Atlas et al.*, 1969*b*].

From these radio experiments, however, there is no clear evidence of any dominating contribution from *horizontal* layers. Tilted, or undulating layers, on the other hand, may well contribute to the deduced $\Phi(K)$ spectrum. It should be emphasized that in this survey we shall not discuss in detail special experiments from which factors such as anisotropy and inhomogeneity can be deduced. We shall largely be concerned with the large group of experiments measuring the $\Phi(K)$ spectrum for $\mathbf{K}$ vertical; however, reference will be made to specific experiments revealing factors such as anistropy and inhomogeneity.

3. DETERMINATION OF REFRACTIVE-INDEX AND AIR-VELOCITY SPECTRA FROM RADIO MEASUREMENTS

As seen from the above, Fourier transforms enter directly into the equations for scattered field strength and scattered angular power spectrum. This strongly suggests that it would be simpler to work in terms of spatial wave-number spectra ($\mathbf{K}$ space) rather than

in terms of spatial correlation functions (physical space). In addition it is well known that the shape of the whole tail-end of the wave-number spectrum effects the autocorrelation function near the origin only. Since the quantities we measure in radio experiments (field strength or power) for high radio-frequency work are directly dependent on the tail-end of the spectrum, the expression for the scattered angular power spectrum is very sensitive to assumptions made about the shape of the autocorrelation function near the origin. Finally, since the topic of the current colloquium is 'spectra of meteorological variables,' it seems particularly pertinent to work in terms of wave-number spectra throughout this contribution. By doing so, it is possible to make a direct comparison between the potentialities of the various experimental techniques that have been used for the purpose of obtaining information about the atmospheric structure.

Inspecting the numerous sets of refractive-index spectra deduced from radio experiments, we find that the dependence of spectrum density on wave number varies tremendously. Accordingly, it does not seem justified to discuss the shape of any one spectrum in great detail. We find that one set of spectra can be described by a simple power law, others by a Gaussian expression, and still others by an exponential. On the basis of these observations it is probably fair to say that if a single form of the refractive-index spectrum is to be used as the basis for a comparison with the experimental result, the simple power law is as good as any. In addition, the fluid dynamicist postulates a refractive-index spectrum of the form $\Phi(K) \sim K^{-11/3}$ for the inertial subrange portion of the turbulence spectrum. In the following, therefore, we shall base our calculations on the assumption that the refractive-index spectrum can be written in the form $\Phi(K) \sim K^{-n}$. Our aim is then to determine the exponent n, and indeed when possible the constant of proportionality, from radio experiments.

For the purpose of ensuring a physical understanding of the phenomena encountered, we shall first assume that the refractive-index structure is isotropic and homogeneous, and we shall neglect the effect of refraction. These factors will be discussed shortly.

3.1. *Determination of refractive-index spectrum $\Phi(K)$ from beam-swinging experiments*

Consider first the experiment involving the synchronous 'swinging' of narrow transmitting and receiving beams in such a way as to change the scattering angle θ. In this simple treatment we shall consider two beam-swinging experiments only: a synchronous beam-swinging in the vertical great-circle plane and a synchronous beam-swinging in the azimuth plane.

Beam-swinging in the vertical plane. We have seen that the scattering cross section per unit scattering volume is proportional to the refractive-index spectrum $\Phi(\mathbf{K})$. Furthermore, the wave number $|\mathbf{K}|$ is given by $|\mathbf{K}| = (4\pi/\lambda)\sin\theta/2$, where λ is the wavelength.

For small values of the scattering angle, we can thus write the following expression for the power received via the scatter circuit

$$P \sim \Phi(K)V \sim K^{-n} \sim \theta^{-n}V \qquad (6)$$

where V is the scattering volume. For narrow beams it can be shown [*Gjessing*, 1964*a*] that the volume $V \sim \theta^{-3}$. Hence

$$P \sim \theta^{-(n+3)} \qquad (7)$$

The minimum scattering angle θ_0 is determined by the angle between the earth's tangent planes; i.e. $\theta_0 = d/a$, when d is the path length and a is the earth's radius.

The maximum scattering angle at which measurable received power can be obtained is determined by factors such as the transmitted power, the path length, and the antenna gains. We denote the maximum elevation angle relative to the earth's tangent plane by α, and thus the *measured quantity* in beam-swinging experiments, namely the ratio of the power received with a scattering angle of $(\theta_0 + 2\alpha)$ to the power received at the minimum scattering angle θ_0, is given by

$$[P(\theta)/P(\theta_0)] = [1 + (2\alpha/\theta_0)]^{-(n+3)} \qquad (8)$$

Note that this assumes vertical homogeneity. If the atmosphere is not homogeneous, the deduced spectrum slope n will have to be modified in order to take the effect of inhomogeneity into consideration. This problem is dealt with in section 3.10.

Figure 1 shows the measured quantity plotted logarithmically to the basis of the exponent n. Note that the expression is normalized so as to give zero decibels when $n = 6$. This is done to facilitate a direct comparison of the potential usefulness of the various experimental techniques. In the particular

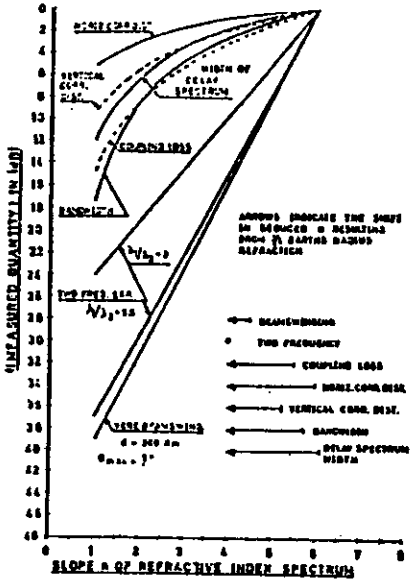

Fig. 1. The theoretical relationship between the measured quantity and the slope n of the refractive-index spectrum [$\Phi(K) \sim K^{-n}$]. The curves show the degree to which the spectrum slope affects the measured quantity. Length of the arrows shows the effect of refraction on the n deductions.

plot in Figure 1, typical values of α and δ_0 have been used, namely $2\alpha = 9°$ and a path length d of 200 km.

Beam-swinging in the horizontal plane. Swinging the beams synchronously in azimuth only, the power versus the azimuth angle relationship is given by

$$P(\beta)/P(0) = [1 + (\beta/d/2a)]^{-(n-2)/n} \qquad (9)$$

This gives rise to a measured quantity $(P(\beta))/P(0)$ versus n relationship very similar to that of the vertical beam-swinging case when substitution is made for $\beta = 5.3°$.

3.2. *Determination of $\Phi(K)$ from multifrequency experiments*

Consider now the experiment involving simultaneous transmission and reception on two widely separated frequencies and scaled antennas. If the antenna beams are narrow such that the scattering volume is determined by the beam geometry rather than by the scattering mechanism, then the scattering volumes for the two frequencies are identical. Accordingly, the ratio of the power received on the two frequencies is given by the ratio of the corresponding scattering cross section as presented in (2). In this case, therefore, the 'measured quantity' is the ratio of power received on the two frequencies given by

$$[P(\lambda_1)/P(\lambda_2)] = (\lambda_1/\lambda_2)^{n-2} \qquad (10)$$

In Figure 1 the power ratio is plotted logarithmically to the basis of n and normalized for $n = 5$.

Two different wavelength ratios are used, namely $\lambda_1/\lambda_2 = 3$ and $\lambda_1/\lambda_2 = 5.5$. If for some practical reasons (e.g. ground reflections) the effective gain of the two scaled antennas are not exactly identical, an error is introduced. It can be shown, however [*Gjessing*, 1968], that the error is proportional to the square root of the antenna gain ratio only. Note that the term wavelength dependence often refers to the case where the received power is normalized with respect to free-space transmission loss. This normalized power ratio then takes the form

$$[(P/P_{FS})(\lambda_1)]/[(P/P_{FS})(\lambda_2)] = (\lambda_1/\lambda_2)^{n-4} \qquad (11)$$

3.3. *Determination of $\Phi(K)$ from measurement of field-strength correlation distance*

In this section attention is focused on the spatial field-strength correlation properties of a scattered radio wave. We have a wide-beam transmitter radiating its power essentially in a horizontal direction. The scattered wave resulting from this transmitter impinges on two nearly identical, small-aperture, receiving antennas positioned beyond the horizon relative to the transmitter. The antennas are spaced vertically or horizontally such that the center line through the receiving antennas is normal to the center line through the transmitter T and the receivers R. We measure the normalized complex correlation of the voltages induced in the antennas.

It can readily be shown [*Gjessing and Bjørresen*, 1968] that this spatial field-strength correlation function is the Fourier transform of the angular power spectrum of the wave reaching the receiving antennas. Specifically, if the antennas are spaced horizontally, thus giving us information about the correlation properties of field strength along a horizontal direction, this correlation function is determined by the angle-of-arrival spectrum as measured in a horizontal plane. If the antennas are spaced vertically, it is the angle-of-arrival spectrum in the vertical plane that matters. Specifying the angle of arrival of a particular scattered wave by an elevation angle α (relative to the center line through T and R) and an azimuth angle β (relative to a great circle plane through T and R), we have in the same manner as above that a refractive-index spectrum $\Phi(K) \sim K^{-n}$ gives rise to an angular power spectrum of the form

$$P(\alpha, \beta) \sim (\beta^2 + \alpha^2)^{-n/2} \qquad (12)$$

The horizontal correlation of field strength is thus obtained by a Fourier transformation of P with respect to β, whereas the vertical correlation is obtained from the $P(\alpha)$ relationship.

A rigorous Fourier transformation of expression 12, however, lends itself to numerical computations only. In our case, we need a simple approximate expression. This can be obtained if we approximate $P(\alpha)$ and $P(\beta)$ by a sin x/x function, thus giving us a simple expression for the Fourier transform. This is a procedure well known in antenna theory. From antenna theory we know that if L is the width of the illuminating field-strength distribution, then the 1/2-power width of the resulting angular power spectrum (beam width) is given by

$$\theta_{1/2} = 0.88\lambda/L \qquad (13)$$

where λ is the radio wavelength. By applying these results to our problem, we find that the 3-decibel width of the scattered beam as measured in the vertical plane is given by

$$P_{\alpha_{1/2}}/P_0 = 1/2 = (\alpha_0 + \alpha_{1/2}/\alpha_0)^{-n} \qquad (14)$$

where $\alpha_{1/2}$ is the 3-decibel beam width of the scattered beam, $\alpha_0 = d/2a$, d is the path length, and a is the earth's radius.

By solving for $\alpha_{1/2}$ and substituting this in (13), we find that the vertical correlation distance of field strength is given by

$$L_V/\lambda = 0.44(a/d)/(2^{1/n} - 1) \qquad (15)$$

Similarly, the horizontal correlation distance is given by

$$L_H/\lambda = 0.44(a/d)/(4^{1/n} - 1)^{1/2} \qquad (16)$$

These approximate expressions are in very good agreement with the results based on rigorous numerical transformations of the scattered angular power spectra [*Gjessing and Bjørresen*, 1968]. Figure 1 shows the measured quantities (vertical and horizontal correlation distances, respectively) plotted logarithmically to the basis of the slope n of the refractive-index spectrum.

Note, however, that the measured quantity is only very weakly related to the spectrum slope and that refraction effects play a dominating role. Thus, as a means of gaining knowledge about the refractive-index fine-scale structure, the space correlation technique is not very powerful.

3.4. *Determination of $\Phi(K)$ from measurement of antenna-to-medium coupling loss*

From basic antenna theory we know that the free-space antenna gain is proportional to the antenna aperture $G = 4\pi A\lambda^{-2}$. When dealing with large antennas in connection with scatter propagation, however, this linear relationship no longer holds. If the antenna aperture is increased by a factor k, the received power is generally increased by a factor that is less than k. This apparent gain degradation is commonly referred to as antenna-to-medium coupling loss. The phenomena can be explained in several different ways. We may base the discussion either on the width of the angular power spectrum of the scattered wave relative to the angular-reception capability of the receiving antenna, or on the spatial correlation distance of the received scattered field strength relative to the dimension of the antenna aperture. In this review we shall use the latter method for the purpose of illustrating the principles involved and to get an expression relating the 'measured quantity' to the slope n of the refractive-index spectrum, rather than to seek an expression of optimum accuracy.

By basing our computations on the results of the previous section, we note that at the receiving site, the area (normal to the direction of propagation) over which the field strength is correlated is given by $L_V L_H$. This area may then be considered as being the effective receiving antenna aperture, provided that the actual aperture is larger than $L_V L_H$. If the actual area $A < L_V L_H$, we do not experience a gain degradation.

The effective antenna gain is thus

$$G_{\text{eff}} = 4\pi L_V L_H \lambda^{-2} \qquad (17)$$

whereas the plane-wave gain is

$$G = 4\pi A\lambda^{-2}$$

The gain loss is thus

$$G_L = \frac{A}{L_T L_R} = \frac{5(2^{1/n} - 1)(4^{1/n} - 1)^{1/2} A}{(a/d)^2 \lambda^2} \quad (18)$$

Figure 1 shows the gain loss plotted against the refractive-index spectrum slope n. It should be emphasized that (18) is based on the assumption of isotropy, as are indeed all the expressions for the measured quantity.

If the atmospheric structure is a horizontally layered one (strongly anisotropic), the spectrum slope n associated with K vertical will be very much different from that associated with K horizontal. Therefore, to calculate the gain loss from (18), we shall have to use different values of n for the two directions.

3.5. *Determination of $\Phi(K)$ from measurement of time delay (pulse-transmission experiment)*

In this section our aim is to deduce the refractive-index spectrum from measurement of time delay. Using wide-beam antennas on either end so that the multipath transmission is governed by the scattered mechanism rather than by the beam geometry, we first seek an expression relating path length l and the position in space of the scattering element; i.e., we require an expression relating l and the scattering angle θ. If d is the length of the chord between T and R, then simple geometrical calculations give the required result, namely

$$\theta = 2[(l/d)^2 - 1]^{1/2} \quad (19)$$

If we transmit a short radio pulse, the power that reaches the receiver has traveled through a wide spectrum of different paths.

By substituting for θ in the expression for the scalar power spectrum ($P \sim \theta^{-n}$), we get the spectrum relating power and path length. Normalizing this power with respect to the power received via the shortest propagation path l, namely that determined by the earth's tangent planes, $l_0 = d[1 + (d/2a)^2]^{1/2}$, the power spectrum takes the form

$$[P(l)/P(l_0)] = (4a^2/d^2)^{-n/2}[(l/d) - 1]^{-n/2} \quad (20)$$

Expressing this spectrum in terms of the path length Δl, which is in excess of the minimum path length l_0 (i.e. writing $l = l_0 + \Delta l$), we find that the power spectrum referred to l_0 is given by

$$[P(\Delta l)/P(l_0)] = [1 + (8a^2/d^2)\,\Delta l]^{-n/2} \quad (21)$$

And since $\Delta l = \tau C$, where C is the velocity of light, the delay spectrum referred to τ_0 (the shortest time delay) is given by

$$[P(\tau)/P(0)] = [1 + (3a^2\tau C/d^3)]^{-n/2} \quad (22)$$

The $1/e$ width of this delay spectrum is then given by

$$\Delta\tau = (d^3/8a^2C)(e^{2/n} - 1) \quad (23)$$

The measured quantity in this experiment is the 1/2 width, $\Delta\tau$, of the time-delay spectrum. This quantity is plotted versus n in Figure 1.

3.6. *Determination of $\Phi(K)$ from measurement of bandwidth (frequency-sweep experiment)*

Our interest is now focused on the bandwidth properties of a scattered wave in relation to the shape of the refractive-index spectrum. The wavelength dependence in the way first discussed thus has no direct bearing on our problem. As before, we consider wide antenna beams such that it is primarily the $\Phi(K)$ function for K vertical that governs the bandwidth. The transmitter frequency is varied over a small frequency band (some 1% frequency deviation) at a rate that is large compared with the rate at which the atmospheric structure changes. At the receiver we measure the power as a function of frequency, sweep-by-sweep, and we find that this is in general a strongly varying function.

The data thus obtained can be analyzed in two ways:

a. At the receiver we can have a bank of bandpass filters measuring the average power from each filter output, thus obtaining the average power-versus-frequency relationship.

b. By using the ensemble of frequency sweeps as a base, we may compute the autocorrelation function in the frequency domain of field strength versus frequency.

By analyzing alternative *a* first, we can use the results of simple network theory to obtain a simple approximate result. We know that the response to a delta pulse of a network is known as the impulse response $V(\tau)$ of the network. Furthermore, the Fourier transform of the impulse response is known as the transfer function $F(\omega)$ of the network. By multiplying this transfer function with its complex conjugate, we obtain the power spectrum that we are seeking. From the previous section we obtain the expression for the impulse response by taking the square root of equation 22. Analyzing this function, we find that it closely resembles an exponential function of the form $P(\tau) = \exp(-a\tau)$. The $1/a$ width of the impulse response is given by

$$\Delta\tau = d^3(e^{2/n} - 1)/8aC \quad (24)$$

To simplify the Fourier transformation, we assume an exponential impulse response such that $\Delta\tau = 1/a$ (when we introduce only a small error). The Fourier transform of the exponential impulse response $\exp(-a\tau)$ is given by

$$F(\omega) = (a + j\omega)^{-1} \quad (25)$$

The power spectrum is then given by

$$W(\omega) = F(\omega)F^*(\omega) = (a^2 + \omega^2)^{-1} \quad (26)$$

substituting for a as obtained from (24) and normalizing the resulting equation for $\omega = 0$, we find that the 1/2 power width of the power spectrum is given by

$$\Delta\omega = 8a^2Cd^{-3}(e^{2/n} - 1)^{-1} \quad (27)$$

In Figure 1 the 'measured quantity,' namely bandwidth, is plotted versus the exponent n of the refractive-index spectrum.

Now let us compute the autocorrelation function in the frequency domain ($R(\Delta\omega)$). The voltage V_1 at frequency ω is given by $V_1 = F(\omega) = (a + j\omega)^{-1}$. Similarly, the voltage V_2 at frequency $(\omega + \Delta\omega)$ is given by $V_2 = F(\omega + \Delta\omega) = [a + j(\omega + \Delta\omega)]^{-1}$. The normalized complex autocorrelation of these two voltages is then given by

$$\rho(\Delta\omega) = \frac{\int_{-\infty}^{\infty} [1/(a + j\omega)][1/(a - j(\omega + \Delta\omega))]\,d\omega}{\int_{-\infty}^{\infty} [1/(a^2 + \omega^2)]\,d\omega} \quad (28)$$

By solving this integral we get the following expression for the modulus of the autocorrelation function

$$R(\Delta\omega) = [1 + (\Delta\omega/2a)^2]^{-1/2} \quad (29)$$

The width of this autocorrelation function is obtained by letting $R(\Delta\omega) = 1/2$, thus obtaining

$$\Delta\omega_{1/2} = 16(3)^{1/2}a^2Cd^{-3}(e^{2/n} - 1)^{-1} \quad (30)$$

Note that the width of the autocorrelation in the frequency domain is $2(3)^{1/2}$ times the 1/2-power width of the power spectrum. When plotted as in Figure 1, however (normalizing with respect to $n = 6$), the two curves coincide.

3.7. *Determination of $\Phi(K)$ from measurement of Doppler spread*

In this section we shall very briefly discuss the possibilities of determining $\Phi(K)$ from measurement of the fading spectrum. First, the post-detection signal is subjected to a frequency analysis, and then the width of the resulting power spectrum is measured.

If k_0 is the wave number of the wave incident on the scattering element the velocity of which is V and if k, is the wave number of the scattered wave, then the Doppler shift of this wave is given by

$$F = 1/2\pi(k_0 - k_s)\cdot V = (1/2\pi)K\cdot V \quad (31)$$

Since the vector K is determined by the position of the scattering element within the effective scattering volume, the Doppler displacement is determined by the position of the scattering element as well as by its velocity.

If all the scattering elements move with the same velocity, then the width of the Doppler spectrum is determined by the size of the scattering volume contributing to the field strength at the receiver; i.e. the width is determined by the size of the effective scattering volume. By using wide beams, this scattering volume is determined by the width of the $\Phi(K)$ function. For small values of θ, K is given by $K = 2\pi\theta/\lambda$, such that the variation in K within the effective scattering volume is $\delta K = (2\pi/\lambda)\beta$, where β is the effective beamwidth given by $\beta = (W/d/2)$, and W is the effective width of the scattering volume as measured in the direction of wind motion in a plane normal to the path. The length of the path is d. Hence, with constant wind velocity, the width of the Doppler spectrum is

$$\delta F = (V/\lambda)\beta \quad (32)$$

The effective beamwidth is calculated from the $\Phi(K)$ function as indicated in section 3.5.

Now we will consider the other extreme case where the scattering volume is extremely small (achieved by the use of very narrow beams) such that K is a constant. If, then, δV is the spread in velocity of the scattering elements, then the width of the Doppler spectrum resulting from the fluctuating component of the air velocity is given by

$$\delta F = (\delta V/\lambda)\theta \quad (33)$$

By combining (32) and (33), we find that the Doppler broadening resulting from a mean wind velocity on which a fluctuating component is super-

imposed is given by

$$\delta F = 1/\lambda(V\beta + \delta V\theta) \tag{34}$$

See *Gjessing* [1962] for details.

Thus we see that if the $\delta V\theta$ term is small compared with the $V\beta$ term, then in principle we can obtain information about β, and hence $\Phi(K)$, from measurement of the Doppler spread and from knowledge about the mean cross-path wind velocity. This, however, does not appear to be a very promising method (since the term $\delta V\theta$ in general contributes considerably), and will hence not be subjected to a detailed analysis in this survey.

It should be emphasized that the current treatment of the Doppler problem largely refers to the case where we have spatial homogeneity of wind as well as of refractive index within the scattering volume. If radio beams that have a large vertical extent are used, the mean cross-path wind velocity must be expected to vary considerably within the scattering volume. Similarly, the intensity of the scattering elements may vary considerably with height. The width of the Doppler spectrum will then tend to be dominated by some compromise between the strongest scattering elements (scattering layers) and those having the largest cross-path wind velocity.

If the long-term frequency stability of the local oscillators in the transmitter and the receiver is sufficiently good to permit measurement not only of Doppler spread but also of the exact location of the Doppler spectrum on the frequency axes, then the potential of the current method as a means of determining $\Phi(K)$ is greatly improved [*Birkemeier et al.*, 1968*b*].

3.8. *Determination of air velocity from Doppler measurements*

Hitherto, the basis for our discussions has been the spatial refractive-index structure $\Phi(K)$. We now wish to discuss what information we can obtain pertaining to the air motion, i.e. the time variation of the refractive-index structure (mean wind and turbulence). Equation 34 sums up the information that can be obtained on the basis of measurement of the Doppler spread, i.e. from an analysis of the fading envelope. This equation can be generalized to include the case of an anisotropic air-velocity field [*Gjessing*, 1962].

Note that the post-detection intensity-fluctuation spectrum $S(F)$ referred to is symmetrical around zero frequency where it has a primary maximum. If $S(f)$ is the pre-detection spectrum (Doppler spectrum), then the measured fluctuation spectrum [*Atlas*, 1969] is given by

$$S(F) = \int_{-\infty}^{\infty} S(f)S(f + F)\,df$$

By denoting the direction of the $\mathbf{K}$ vector as measured in a vertical cross-path plane by γ relative to the vertical direction, our expression for the Doppler spread becomes

$$\delta F = 1/\lambda[V\beta + \delta V(\gamma)\theta] \tag{35}$$

By using narrow beams such that the beamwidth β is a known quantity (independent of the scattering mechanism), information about V (the mean cross-path component of the wind) and the fluctuating component of the wind $\delta V(\gamma)$ can be obtained from beam-swinging experiments varying θ and γ, respectively, in a controlled fashion and by measuring the corresponding Doppler spectrum [*Gjessing*, 1962].

If we have access to the absolute frequency at the receiver, i.e., if we can measure the Doppler shift, it is clear from (31) that if the mean cross-path wind is essentially horizontal, the mean Doppler shift is given by

$$F_0 = (1/2\pi)KV\sin\gamma \tag{36}$$

since γ measures the direction of $\mathbf{K}$ relative to the vertical direction and since the direction of $\mathbf{V}$ is assumed to be 90° relative to the vertical.

Furthermore, since $K \simeq (2\pi/\lambda)\theta$, the mean Doppler shift is given by

$$F_0 = (2V/\lambda)\alpha \tag{37}$$

where α is the azimuthal angle of the small scattering volume from the great circle. By pointing narrow-beam antennas off the great-circle bearing by a known amount α, we can obtain information about the horizontal cross-path component of the mean wind velocity [*Birkemeier*, 1963*a*; *Atlas et al.*, 1969*a*]. But to avoid the contamination due to a possible horizontal specular surface, the angle α should be at least a couple of beamwidths.

3.9. *The effect of refraction on the $\Phi(K)$ deductions*

We have seen that in most of the expressions relating the slope n of the refractive-index spectrum to the measured quantity, the minimum scattering angle d/a is a parameter. But, although the path length d is generally known accurately, the effective earth's radius a is not, since it is strongly dependent on refraction. In order to deduce n from a particular experiment, therefore, we need information about the refraction.

Figure 1 shows the effect of refraction on the n deduction. The arrows indicate the shift in deduced n value resulting from refraction corresponding to a 4/3 a effective earth radius. We see, for example, that if a refractive-index spectrum $\Phi(K) \sim K^{-4}$ is deduced from measurement of the time-delay spectrum assuming no refraction, the actual refractive-index spectrum is proportional to K^{-4} if we are including the effect of the 4/3 earth-radius refraction.

3.10. *The effect of spatial inhomogeneity on the $\Phi(K)$ deductions*

It is generally observed that the scattering ability of the atmosphere changes with height, whereas the conditions are more constant horizontally [*Gjessing*, 1964*a*]. We therefore generalize our expression for the scattering cross section (refractive-index spectrum) to read

$$\sigma \sim \nu(z)\Phi(K)$$

where $\nu(z)$ is the homogeneity function, z being the vertical coordinate. We have seen that most of the experiments measure the combined effect of the ν and Φ functions, since for scattering in a great-circle plane, $|\mathbf{K}|$ is proportional to the height of the scattering element. To determine the Φ function, therefore, we must have information about the ν function. This can be obtained by experiments of a more specialized nature [*Gjessing*, 1964*a*] and is therefore not considered as being within the scope of this presentation.

Let us now discuss the influence of the ν function on the n deductions. To illustrate this influence let us base our discussion on the vertical beam-swinging experiment, bearing in mind that the results obtained are directly applicable to the deductions of n made from the measurements of the pulse delay, the bandwidth, the coupling loss, and the vertical and horizontal correlation distance. Indeed, of the experimental techniques that we have discussed it is only the multifrequency experiment that is not directly affected by a lack of spatial homogeneity.

Experiments show [*Bøerresen and Gjessing*, 1969] that in general the ν function can be written in the form $\nu(z) = 10^{-[\text{constant}]z}$, where m is expressed in db/km. Since $z_{av} = (d/2)\theta_e/2$ and $z = d/2(\theta_e + 2\alpha)/2$, our expression for the normalized angular power spectrum takes the form

$$[P(\alpha)/P_0] = [1 + (2\alpha)/(d/a)]^{-n}10^{-[md/20]4\alpha} \tag{38}$$

By analyzing this expression, we find that it is similar to the familiar power law. We thus want to compare the above expression with an expression of the form

$$[P(\alpha)/P_0] = [1 + (2\alpha)/(d/a)]^{-n'} \tag{39}$$

so as to be able to find a relationship between n and n'. To obtain this relationship we equate equations 38 and 39 for $[P(\alpha)/P_0] = 1/10$ when $2\alpha/(d/a) = [10^{1/n'} - 1]$.

The result is the following relationship

$$n = n' - (md^2/40a)n'[(10)^{1/n'} - 1] \tag{40}$$

The function $n'[10^{1/n'} - 1]$, however, is a slowly varying function.

To simplify the final expression we put $n'[10^{1/n'} - 1] = 2.75$, introducing a negligible error if $|n'| > 6$ and a 20% error in the $n'[10^{1/n'} - 1]$ factor for $3 < n' < 6$. Our relationship between n and n' then becomes $n \approx n' - 1.07 \times 10^{-4}md^2$. Using, then, a typical value for m, namely 3 db/km, we find that the error Δn in the deduced value of n resulting from inhomogeneity for various values of the path length d is as given in Table 1.

It should be mentioned that, whereas the results from most forward-scatter experiments suggest an exponential fall-off with the height of the scattering intensity, radar backscatter experiments often indicate the occurrence of discrete scattering layers. If the atmospheric structure is predominantly layered, the exponential ν function adopted in this survey is probably not well justified.

4. DETERMINATION OF $\Phi(K)$ ON THE BASIS OF SPECIFIC EXPERIMENTAL RESULTS

In this section we shall consider some specific experimental results from which we shall deduce the refractive-index spectrum. The results have generally been made available by the appropriate experimentalist (either through publications or by correspondence) in their original form such that we

TABLE 1. Error in deduced n resulting from a vertical inhomogeneity of 3 db/km

d, km	500	300	200	100	50
Δn	8	2.9	1.3	0.3	0.03

have at our disposal, for example, the histogram giving the frequency of occurrence of the vertical correlation distance for a given path length and a given radio frequency. On the basis of these basic results and on the basis of our set of equations relating the refractive-index spectrum to the measured quantity, we shall calculate the cumulative distribution function for n. Note that n, as before, is the exponent in the power law $\Phi(K) \sim K^{-n}$.

This treatment of experimental findings (deductions) should not be regarded as comprehensive and complete. Results from many powerful experiments of a somewhat special nature will not be mentioned. The reasons for omitting these are the shortage of space and the fact that some of the results that have been made available do not readily lend themselves to the deduction scheme adapted in this survey. Examples of such results are some of those of *Fehlhaber* [1965]. Fehlhaber generally works in physical space rather than in K space, and he draws conclusions about the correlation distance in space of the refractive index (scale length in the vertical and in the cross-path horizontal direction). He concludes that the spatial correlation function of refractivity is a Norton function of the order of 1/3 such that the one-dimensional wave-number spectrum takes the form $E(K) \sim K^{-5/3}$.

4.1. *Deductions from beam-swinging experiments*

The cumulative distribution function of Figure 2 shows the results from two recent beam-swinging experiments serving as examples from this group of experiments. Table 2 shows the median values deduced from several other beam-swinging experiments. Referring to the results of *Bull and Neisser* [1963], we see that the probability distribution of spectrum slope n is a normal distribution with a median value of 4.1 and a range from 2.2 to 6. The results of *Gjessing et al.* [1969] also give a normal probability distribution for n with a median value of 3.3. Note that the effect of refraction and the lack of vertical homogeneity on the n deductions have been accounted for in this experiment. This is made possible by using radiosondes from which the vertical N profile is deduced and by using a supplementary beam-swinging experiment [*Bjørresen and Gjessing*, 1969]. The radio frequency used is 6 GHz.

Table 2, which summarizes the results, presents two very recent n deductions made by G. Bull and J. Neisser (private correspondence, 1969), where a mean value of $n = 3.8$ is obtained from beam-swinging experiments using a radio frequency of 2.4 GHz, and a mean value of $n = 3.6$ is obtained by using 9.4 GHz. Bull and Neisser are in the process of relating their n deductions to the Richardson number. H. Jeske (private correspondence, 1969) has completed beam-swinging experiments between Bremerhaven and Heligoland on two frequencies, namely 16.5 and 7.5 GHz, obtaining a median value of $n = 3.6$ for both wavelengths. *Cox and Waterman* [1968] conclude on the basis of phase and amplitude measurements of transhorizon microwaves that n varies from 4 to 10. They included only cases that can be described by a model predicting a smooth decrease of scattered power with scattering angle.

4.2. *Deductions from multifrequency experiments*

The deductions made from multifrequency experiments are shown in Figure 3. *Eolgiano's* [1964] summer measurements give a median n value of 3.5, whereas the winter measurements give $n = 4.7$. The wavelength dependence is obtained from measure-

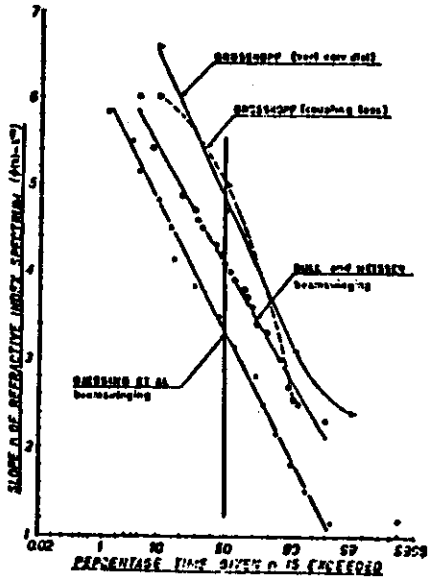

Fig. 2. Probability distributions of the spectrum slope n as deduced from recent beam-swinging radio experiments [$\Phi(K) \sim K^{-n}$].

TABLE 2. Deductions of the slope n of the refractive-index spectrum [$\Phi(K) \sim K^{-n}$].*

Type of Experiment	Investigator	n	No.
Beam-swinging experiments	Bull and Neisser	3.6 3.8 4.1	1
	Gjessing et al.	3.3	2
	Jeske	3.6	3
	Waterman et al.	Varies from 4.0 to 10.0	4
Multifrequency experiments	Eolgiano	3.5 4.7	5
	Eklund and Wickerts	4.4	6
Vertical field-strength correlation	Grosskopf	4.8	7
Coupling loss	Grosskopf and Fehlhaber	4.5	8
	Grosskopf	5.0	9
Delay spectrum width	Barrow et al. (Few exp. only)	Varies from 2.7 to 8.0	10
Bandwidth	Waterman et al.	3.8	11

* Note that all n values are median values except results no. 4 and 10.

ments on three wavelengths: $\lambda = 3.3$ cm, $\lambda = 10.7$ cm, and $\lambda = 35.7$ cm. The exponent n is deduced by averaging the wavelength dependence obtained from the ratio $P(\lambda = 10.7)/P(\lambda = 3.3)$ and that obtained from the ratio $P(\lambda = 35.7)/P(\lambda = 10.7)$.

Finally, the measurements of *Eklund and Wickerts* [1968] give an n value of 4.4. Their results (shown in Figure 3) are obtained by using two radio frequencies, namely 1 and 3 GHz.

4.3. *Deductions from vertical field-strength correlation measurements*

Whereas the relationship between measured quantity and n in the case of beam-swinging and multifrequency experiments is very simple, and the deductions are straightforward with a high level of confidence, we see from Figure 1 that the correlation distance is very loosely related to the slope n of the refractive-index spectrum. We also see that refraction effects are important. On the basis of some of Grosskopf's experimental results from measurements of vertical field-strength correlation distance [*Grosskopf*, 1963], the probability distribution of the slope n is deduced. The results are shown in Figure 2.

4.4. *Deductions from measurements of antenna-to-medium coupling loss*

The question of relating the coupling loss to parameters describing the atmospheric state appears to be a very controversial topic. There are several theories and considerable disagreement. With this in mind, the task of deducing an atmospheric structure from coupling loss measurements does not appear to be a promising one. For the sake of completeness, however, and for the purpose of illustrating the variability of the spectrum slope n rather than determining its median value very accurately, we shall include n deductions from coupling loss measurements. The equation for coupling loss given above assumes a small-aperture transmitter and a receiving aperture the dimensions of which are large in comparison with the field-strength correlation distance (i.e. $D_T > L_T$ and $D_R > L_R$, where D and L are the antenna dimension and the correlation distance, respectively). These conditions may not be satisfied for all values of n. For low values of n we may find that the vertical correlation distance of field strength is larger than the antenna diameter, whereas the horizontal is not. This has to be taken into consideration when deducing n from measurements of

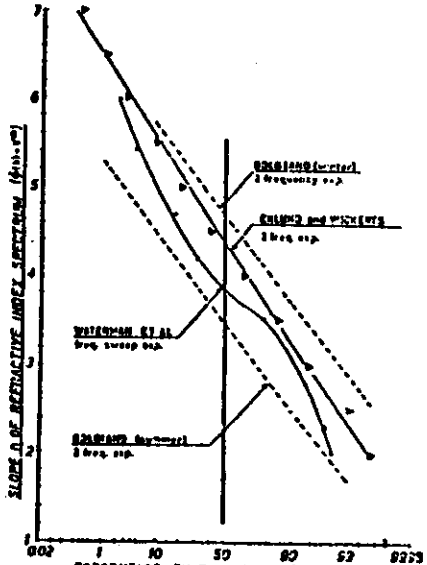

Fig. 3. Probability distributions of the spectrum slope n as deduced from multi-frequency radio experiments [$\Phi(K) \sim K^{-n}$].

coupling loss. To measure antenna loss in practice, we will have to compare the power received on a large antenna with that received on a smaller one. The smaller antenna used as the reference may suffer a coupling loss for low values of n but not for high values. Finally, if we use a large transmitting antenna for practical reasons instead of a small one, this large antenna may not have the same effect on the coupling loss of the two receiving antennas.

The results of *Grosskopf* [1963] and *Fehlhaber and Grosskopf* [1968] are used as the basis for the n deductions shown in Figure 2. The equation for coupling loss given above is used as the basis for calculation of loss on both the receiving antennas. The measured quantity, which in this case is the difference in coupling loss experienced on the two antennas, is then obtained. Note the close agreement between the n deductions made from Grosskopf's vertical correlation measurements with those made from his coupling loss measurements. These two sets of measurements were made on the same path (Hamburg-Darmstadt) and at the same time. Note also that the horizontal correlation distance and the coupling loss are affected by atmospheric anisotropy, whereas this is not the case with the remaining experiments discussed. Since our n deductions from measurements of coupling loss assume isotropy, it is probable that the ones we present in Figure 3 are in error.

4.5. *Deductions from measurements of delay spectra*

The measurement of time delay (and Doppler shift) using the Rake troposcatter technique [*Barrow et al.*, 1963] looks very promising. Since this particular experiment measures not only the pulse broadening (width of delay spectrum) but also the absolute delay experienced on a given path, we can draw conclusions about the refraction and thus improve the accuracy of the n deduction. Although, as we have seen from Figure 1, the influence of n on the measured quantity is not among the strongest, the fact that we can get information about the refraction effects adds substantially to the potential usefulness of the technique.

Unfortunately, the amount of data available for this survey is limited. Consequently no complete distribution function of the exponent n in the power law can be given. On the basis of the few sets of experimental data available, it can be concluded that the n values deduced are in general agreement with the other experiments investigated. See Table 2 for details.

4.6. *Deductions from measurement of band width (frequency-sweep experiments)*

In this survey we shall confine ourselves to the results from only one more investigation, namely, one based on the measurement of correlation distance in the frequency domain. Several such experiments have been performed. However, most of these do not lend themselves to n deductions, since the bandwidth is governed by the transmitter and receiver beamwidth rather than by the $\Phi(K)$ function.

As an example from the large group of frequency-sweep experiments, Waterman's experiments will be given [*Waterman et al.*, 1961]. Figure 3 shows the cumulative probability distribution of n. Note that the curve does not suggest a normal distribution. This is probably a result of a limited ensemble (37). We see that the range of variation of deduced n is in accord with the other experimental results, and we also see that the median value of n is 3.8. Table 2 summarizes the essential data pertaining to the n deductions.

5. CONCLUSIONS

Expressions for the characteristic properties (measured quantity) of a scattered radio wave have been derived in terms of parameters describing the tropospheric refractive-index structure. On the basis of this set of equations (which have been derived in a unified manner), deductions regarding the slope n of the refractive-index spectrum [$\Phi(K) \sim K^{-n}$] are made from specific measurements of

a. Angular scattered power spectrum.
b. Power received at different wavelengths.
c. Vertical correlation of field strength.
d. Antenna-to-medium coupling loss.
e. Width of time-delay spectrum.
f. Bandwidth of scattering mechanism.

Probability distributions of the exponent n are given on the basis of the distribution functions of the measured quantity. It is found that the width of the distribution functions is very much the same irrespective of experimental technique. The exponent n varies from approximately -2 to -6. The median value varies from experiment to experiment, the range of variation being from -3.3 to -5. This variation can not be interpreted as being due to errors introduced in the measurements. By performing experiments having a high level of confidence and by accounting for factors such as refraction and lack of spatial homogeneity, it is found that the median value of the exponent n varies substantially from summer to winter. It varies also with geographical position. It thus seems manifest that the slope n of the refractive-index spectrum is indeed a variable quantity.

It should be emphasized, however, that we have not shown that homogeneous, isotropic turbulence does not always obey the $-5/3$ law ($n = 11/3$) in what is believed to be the inertial subrange portion of the spectrum. It may well be that the deviation from 11/3 in our n deduction is a result of thin turbulent strata in the troposphere such that the 11/3 fluctuation spectrum is superimposed on a systematic refractive-index profile. If the layer is [illegible] and the change in mean refractive index through the layer is large, then the contribution from the mean profile to the $\Phi(K)$ spectrum that we measure by radio methods may be large [*Gjessing*, 1968]. This may well be the reason that wintertime and nocturnal measurements indicate larger n values than do summer and daytime observations.

One may perhaps also argue that intermittency (in time) of an 11/3 law turbulence field may lead to n values such as those measured, or one may introduce the effect of buoyancy and anisotropy. Answers to these questions, however, are beyond the scope of this paper.

Acknowledgments. The author gratefully acknowledges the help given to him by a large group of individuals who have supplied information to this survey. Their prompt reply to requests, their conscientious considerations of particular questions, and their generosity in providing basic material have been of great value.

REFERENCES

Atlas, D. (1959), The measurement of crosswind by noncoherent dual arm bistatic radio tropo-scatter techniques, *Tech. Rep. 10*, Laboratory for Atmospheric Probing, University of Chicago, Ill.

Atlas, D., R. C. Srivastava, R. E. Carbone, and D. H. Sargeant (1969a), Doppler crosswind relations in radio troposcatter beam-swinging for a thin scatter layer, *Tech. Rep. 8*, Laboratory for Atmospheric Probing, University of Chicago, Ill.

Atlas, D., R. C. Srivastava, and W. S. Marker, Jr. (1969b), The influence of specular reflections on bistatic tropospheric radio scatter from turbulent strata, *Tech. Rep. 9*, Laboratory for Atmospheric Probing, University of Chicago, Illinois Institute of Technology, Chicago, Ill.

Barrow, B. B., et al. (1963), Indirect atmospheric measurements utilizing rake tropospheric scatter techniques, paper presented at 1963 URSI fall meeting, Boston, Massachusetts (University of Wisconsin Rep., Madison).

Birkemeier, W. P., P. F. Duvoisin, A. H. Faustine, and D. W. Thomson (1963a), Radiometeorological interpretation of rake channel sounding observations, paper presented at the URSI fall meeting, Boston, Massachusetts (University of Wisconsin Rep., Madison).

Birkemeier, W. P., H. S. Merrill, Jr., D. H. Sargeant, D. W. Thomson, G. M. Beamer, and G. T. Bergemann (1963), Observation of wind-produced Doppler shifts in tropospheric scatter propagation, *Radio Sci.*, *3*(4), 309–317.

Bolgiano, R. Jr. (1963), Evidence of anisotropy in tropospheric microstructure, *J. Geophys. Res.*, *68*, 4873–4874.

Bolgiano, R. Jr. (1964), A study of wavelength dependence of transhorizon radio propagation, *Cornell Univ. Res. Rep. 133*, Ithaca, N. Y.

Børresen, J. A., and Dag T. Gjessing (1969), Homogeneity of the tropospheric refractive-index structure, *Radio Sci.*, *4*(12), this issue.

Bull, G., and J. Neisser (1968), Untersuchungen der atmosphärischen Feinstruktur mit Hilfe von Ausbreitungsmessungen im Mikrowellenbereich, *Beitr. Geophys.*, *77*(5), 394–410.

Cox, D. C., and A. T. Waterman, Jr., (1963), Phase and amplitude measurements of transhorizon microwaves with a multibeam-gathering antenna array, *AGARD Conf. Proc. 37*, 18–1 to 18–16.

Ekland, P., and S. Wickerts (1968), Wavelength dependence of microwave propagation far beyond the radio horizon, *Radio Sci.*, *3*(11), 1065–1074.

Fehlhaber, L. (1966), Diversity Abstand auf scatter Strecken im Frequenzbereich zwischen 1 GHz und 10 GHz, *Tech. Berichi 3531*, Fernmeldetechnisches Zentralamt, Deutschen Bundespost.

Fehlhaber, L., and J. Grosskopf (1963), Messung der Gewinnminderung bei 1715 MHz auf einer 403 km langen scatter-Versuchsstrecke, Fernmeldetechnisches Zentralamt, Deutsche Bundespost, *FTZ, A455, Th 7, Okt.*

Fried, D. L. (1966), Limiting resolution looking down through the atmosphere, *J. Opt. Soc. Amer.*, *56*(10), 1380.

Gjessing, Dag T. (1962), Determination of permittivity variations in the troposphere by scatter propagation methods, *Proc. IEE, London C*, *109*, 446–456.

Gjessing, Dag T. (1964a), An experimental study of the variation of the tropospheric scattering cross-section and air velocity with position in space, *IEEE Trans. Antennas Propags.*, *12*(1), 65–73.

Gjessing, Dag T. (1964b), Determination of the isotropy properties of the tropospheric permittivity and wind velocity fields by radio-propagation methods, *J. Geophys. Res.*, *69*(4), 569–581.

Gjessing, Dag T. (1968), Scattering of radio waves from regular and irregular time varying refractive-index structures in the troposphere, *AGARD Conf. Proc. 37*, 15–1 to 15–17.

Gjessing, Dag T., and J. A. Børresen (1968), The influence of an irregular refractive-index structure on the spatial field-strength correlation of a scattered radio wave, *IEE (London) Conf. Pub. 45*, 43–50.

Gjessing, Dag T., and F. Ingens (1964), On the scattering of electromagnetic waves by a moving tropospheric layer having sinusoidal boundaries, *IEEE Trans. Antennas Propaga.*, *12*(1), 51–64.

Gjessing, Dag T., A. Kielsen, and J. Nordø (1969), Spectral measurements and atmospheric stability, *J. Atmos. Sci.*, *26*,462–468.

Grosskopf, J. (1968), Investigation of the receiving field for scatter propagation, *AGARD Conf. Proc. 37*, 22-1 to 22-11.

Tatarskii, V. I. (1961), *Wave Propagation in a Turbulent Medium*, McGraw-Hill, New York.

Waterman, A. T., Jr., Dag T. Gjessing, and C. L. Liston (1961), Statistical analysis of transmission data from a simultaneous frequency-and-angle scan experiment, paper presented at the URSI spring meeting, Washington, D. C.

ON THE USE OF FORWARD SCATTER TECHNIQUES IN THE STUDY OF TURBULENT STRATIFIED LAYERS IN THE TROPOSPHERE

DAG T. GJESSING

Norwegian Defence Research Establishment, P.O. Box 25, N-2007 Kjeller, Norway

(Received 15 August, 1972)

Abstract. This review paper considers the potentials of forward scatter radio techniques as a diagnostic tool in the study of stratified turbulent layers. Seven classes of experimental techniques have been considered (beamswinging, multifrequency, vertical and horizontal field strength correlation, coupling loss, pulse delay and bandwidth measurements). All these techniques with the exception of bandwidth and delay experiments measure directly or indirectly the irregularity spectrum of refractive index. Bandwidth hand delay distributions are determined by the vertical distribution of the refractivity irregularities. Thus for the purpose of obtaining information about a layered structure where our interest is focused on the vertical refractivity distribution rather than on the averaged spectral properties of the structure, the last two categories of experiments appear to represent a powerful tool. If one is interested in the spectral properties, multifrequency and beamswinging experiments are of great potential value whereas other experiments such as that measuring coupling loss are largely influenced by pure refraction effects.

1. Introduction

It is the object of this survey to discuss the potentials of forward scatter radio techniques in the study of stratified turbulent layers. The survey represents to a large extent a continuation and an extention of the review given at the preceding IUCRM Colloquium (Gjessing, 1969). In that previous review, emphasis was placed on the study of an essentially homogeneous atmospheric structure in the sense that it was assumed that the form of the refractive index spectrum remains invariant within the spatial atmospheric region under investigation. The variance of the refractivity fluctuations, however, was assumed to be a function v of position in space (x, y, z). Furthermore it was assumed that the three-dimensional spectrum of the refractive index fluctuations can be written in the form $\Phi(K) \sim K^{-n}$ such that the scattering cross-section σ is given by

$$\sigma \sim v(x, y, z)\, K^{-n}.$$

Finally, the treatment was based on the assumption that the mean refractive index decreases systematically with height z such that this decrease can be taken into account by introducing a parameter a (effective Earth radius) given by

$$\frac{1}{R} = \frac{1}{a} + \frac{\mathrm{d}n}{\mathrm{d}z},$$

where R is the actual earth radius and $\mathrm{d}n/\mathrm{d}z$ is the vertical mean refractive index gradient.

The previous review, on which the current contribution is largely based, considered the influence on the quantities measured in trans-horizon propagation (correlation distance of field strength, bandwidth, pulse distortion, etc.) of the slope n of the refractive index spectrum, the refractive index gradient a, and the inhomogeneity factor v. The relationship between the measured quantities and n, a and v was calculated in a unified manner so as to enable us to compare the values of n, a and v deduced from the various experiments. Deducing then the spectrum slope n from various experiments, specifically beamswinging experiments, bandwidth measurements, measurement of vertical correlation distance of field strength, antenna coupling loss and two frequency experiments, it was found that the widths of the essentially Gaussian n-distribution curves were very much the same for the different experiments. These distribution curves are shown in Figures 1 and 2.

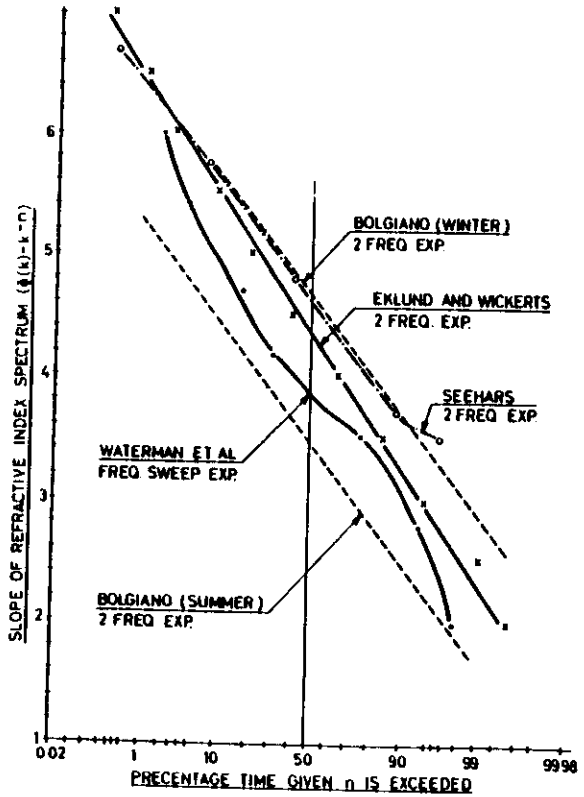

Fig. 1. Probability distributions of the spectrum slope n as deduced from two-frequency and frequency sweep experiments.

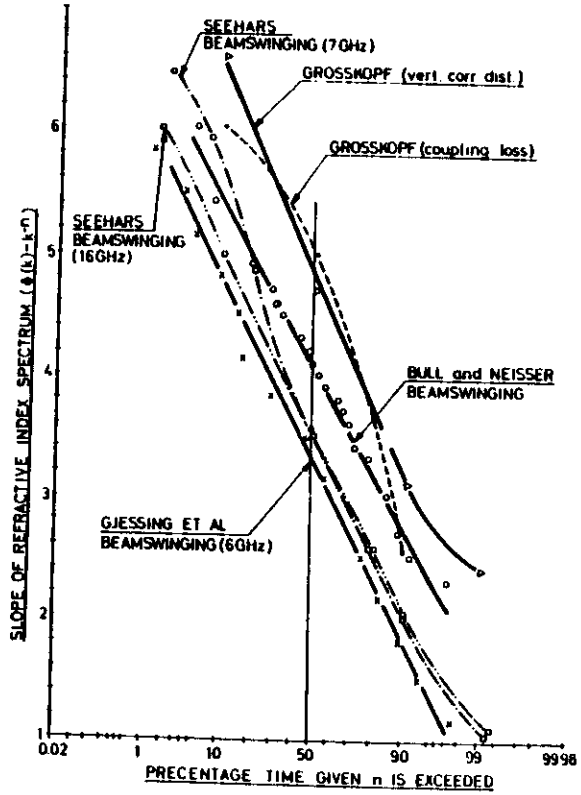

Fig. 2. Probability distributions of the spectrum slope n as deduced from beamswinging, coupling loss and field strength correlation experiments.

It should be emphasized that in order to review the rather large field under consideration within a reasonable number of pages and in order for the review to serve its purpose in the present context, the treatment will be limited to a statistical one. If one were to include single isolated experiments or case studies such as the earlier rapid beamswinging experiments of Waterman (1958b), the conclusion regarding the potential of forward scatter techniques would be different and in some cases more favourable. Since such a treatment no doubt would complicate the issue, it is not considered justified in this review paper.

As we know, in forward scatter experiments it is a very particular spectral component in the refractive index irregularity spectrum that contributes and is responsible

for the scattering of the electromagnetic wave, namely the wave number K given by

$$K = \frac{4\pi}{\lambda} \sin \theta/2,$$

where λ is the radio wavelength and θ the scattering angle. Most tropospheric experiments, and certainly all those referred to in Figures 1 and 2 make use of irregularity spectral wave numbers within the region corresponding to the inertial subrange portion of the turbulence spectrum. For isotropic and homogeneous turbulence, we should therefore be dealing with the $-\frac{5}{3}$ law portion of the spectrum such that our spectrum slope n would be $-\frac{11}{3}$.

Figures 1 and 2 show that although the median value of spectrum slope n is close to that corresponding to the inertial subrange, the variability in n is very large. This variability may indicate the dominance, or at least notable contribution, of stratified layers in the troposphere. The current survey has the objective of serving two purposes:

(i) To seek an explanation of the n variability shown in Figures 1 and 2, basing the analysis on the assumption of thin turbulent layers embedded in a background of turbulence.

(ii) To investigate the relative potentials of the forward scatter techniques when used as a diagnostic tool in the study of waves and turbulence in stratified layers.

Following the procedure adopted in the previous review (Gjessing, 1969) and to some extent basing the work on the results of this contribution, we shall study the major techniques individually with a view to establishing to what extent a stratified atmospheric structure influences the quantities measured in the individual experiments.

First in Section 2 let us define what we mean by the term 'stratified turbulent layers'.

2. The Atmospheric Structure Under Investigation

For the purpose of illustrating the physics and the fundamental principles of the problem at hand, we shall discuss the effect of three idealized atmospheric structures on the characteristic properties of a trans-horizon scatter signal and restrict ourselves to these structures. In this context we therefore define the term 'stratified turbulent layers' as follows:

Referring to Figure 3 we have pictured:

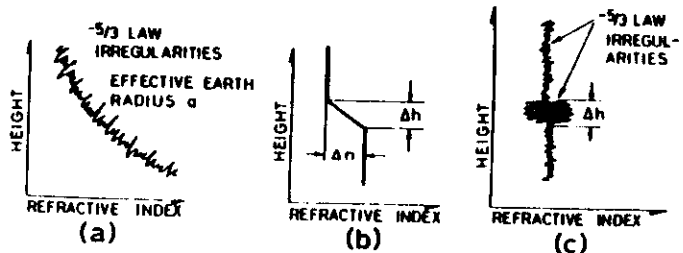

Fig. 3. The categories of atmospheric structures under consideration.

(a) A homogeneous $-\frac{5}{3}$ law irregularity structure superimposed on a mean refractive index gradient characterized by an effective Earth radius a.

(b) A layer model with a linear n-profile. Layer thickness is Δh, the change in mean refractive index through the layer is Δn.

(c) A spatial intermittent irregularity field. We have $-\frac{5}{3}$ law irregularities throughout the depth under consideration, but large variance fluctuations are restricted to a small height interval Δh. The variance is $\overline{\Delta n^2}$ within the turbulent layer and $\overline{\delta n^2}$ outside.

In the real atmosphere we may have the superposition of all three structures. A shear zone such as that in (b) will sharpen the boundaries of the turbulent layer, increase the variance of n within the layer and ultimately decrease the gradient of the mean refractive index within the layer. The contribution to the resultant scatter field from the (a), (b) and (c) structures are randomly phased and can thus be added on a power basis (Gjessing, 1969). It is therefore permissible to treat the structures individually and add the individual results.

This we shall now set out to do.

3. Scattering from a Turbulent Layer Embedded in a Background of Turbulence

Although we have seen a very large number of troposcatter experiments performed with a view to obtaining information about the tropospheric refractive index structure, most, if not all, fall within 7 main categories:

(1) Experiments involving beamswinging in horizontal and vertical planes.

(2) Multifrequency experiments, i.e., comparisons of time-averaged power on several radio frequencies.

(3) Measurement of vertical correlation distance of field strength.

(4) Measurement of horizontal correlation distance of field strength.

(5) Measurement of antenna-to-medium coupling loss.

(6) Time delay experiments (Rake techniques).

(7) Bandwidth measurements (Frequency sweep experiments).

Basing our work on the atmospheric structure referred to above, we shall now investigate to what degree of detail and to what level of confidence we can determine the characteristic properties of this structure on the basis of the seven classes of forward scatter experiments.

3.1. Structure Deductions from Beamswinging Experiments

Consider first the experiment involving the synchronous 'swinging' of narrow transmitting and receiving beams in a vertical plane in such a way as to change the scattering angle θ. With the beams in a vertical great-circle plane, it is the vertical component of the three-dimensional refractive index spectrum that contributes to the received power.

We must therefore consider the irregularities along the vertical direction within the scattering volume. This volume is that illuminated by the transmitting beam and 'seen' by the receiving beam, i.e., the volume common to two intersecting cones.

We shall now investigate the relative contribution to the angular power spectrum from the three groups of structures referred to in Figure 3.

(a) The scattering cross-section per unit scattering volume defined as the mean power in the scattered waves per unit power density of the incident wave in the scattering volume, per unit solid angle in the scattered direction θ is given by

$$\sigma = \frac{\pi k^2}{2} |f_s(z)\, e^{-jKz}\, dz|^2 \tag{1}$$

$$= \frac{\pi k^4}{2} \Phi(K), \tag{2}$$

where k is the wave number $= 2\pi/\lambda$ (λ being the radio wavelength), and $f_s(z)$ is the variation of refractive index along a vertical direction z.

$K = k_i - k_s$

k_i = wave number of incident field

k_s = wave number of scattered field

such that

$$|K| = \frac{4\pi}{\lambda} \sin \theta/2 \tag{3}$$

since θ is the angle between k_i and k_s.

If then the random refractivity fluctuations (background turbulence) obey the inertial subrange $K^{-5/3}$ law, the three-dimensional spectrum $\Phi(K)$ will be proportional to $K^{-11/3}$ and the scattering cross-section σ given by

$$\sigma = \frac{0.03\, C_n^2}{\lambda^{1/3} (\sin \theta/2)^{11/3}}, \tag{4}$$

where C_n^2 is Tatarski's scatter coefficient. The power received from a scattering volume V is then

$$P \sim \Phi(K)\, V \sim \theta^{-11/3} V \tag{5}$$

and since for narrow beams $V \sim \theta^{-1}$, we have

$$P \sim \theta^{(1+11/3)}. \tag{6}$$

As seen from Equation (3) above, we can probe the $\Phi(K)$ spectrum in a range of K determined by the minimum scattering angle θ_{min} and the maximum θ_{max}.

The angle θ_{min} is governed by the angle between the tangent planes through the transmitter and the receiver, respectively, so that $\theta_{min} = d/a$ where d is the path length and a the effective Earth radius. The maximum scattering angle θ_{max} is determined by the power level relative to the noise level at the receiver. Thus the relative received

power is given by

$$\frac{P(\theta)}{P(\theta_0)} = \left(1 + \frac{\theta}{d/a}\right)^{-(1+11/3)} \tag{7}$$

and the power received at any given scattering angle is determined by C_n^2 and the scattering volume. We see that in order to determine the influence of the background random irregularities on the scattered field strength, we must know the mean refractive index gradient, i.e., the effective earth radius a. The validity of the $-\frac{1}{3}$ law inertial subrange cannot be determined from beamswinging experiments without knowledge about the parameter a. For details the reader is referred to Gjessing (1969).

(b) We shall now address ourselves to the problem of scattering (specular reflection) from a non-turbulent atmospheric layer. The discussion will be limited to a layer within which the refractive index varies linearly as shown in Figure 3b.

The angular power spectrum of the wave scattered (reflected) from a systematic refractive index profile is obtained by simple Fourier transformation of the refractive index profile within the scattering volume as indicated in Equation (1) above.

This procedure has been substantiated by several authors (e.g., Wait 1964, Gjessing *et al.*, 1964 and Gjessing, 1969). In this contribution we shall largely limit ourselves to Wait's results, which essentially are the same as those of Saxton *et al.* (1964). A somewhat generalized treatment of Wait's results are shown in Figure 4.

For the particular layer profile under consideration (linear decrease of refractive index Δn over a height interval Δh), the power reflection coefficient is given by

$$|\varrho|^2 = \left| \frac{\Delta n}{2 \sin^2 \theta/2} \left(\frac{\sin X}{X}\right) \right|^2, \tag{8}$$

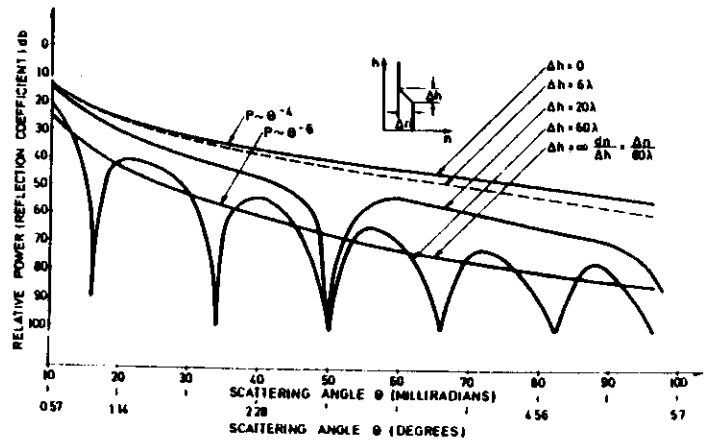

Fig. 4. Angular power spectrum of a scattered wave resulting from a layer of thickness Δh.

where

$$X = \frac{2\pi\Delta h}{\lambda} \sin\theta/2 .$$

The two limiting cases are an infinitesimally thin layer ($\Delta h = 0$) and an infinitely thick layer ($\Delta h = \infty$). For $\Delta h = 0$ it can readily be verified that the power reflection coefficient is given by

$$|\varrho|^2 = \left| \frac{\Delta n}{2 \sin^2 \theta/2} \right|^2 \tag{9}$$

i.e., $$P(\theta) \sim \theta^{-4} . \tag{10}$$

We see that an infinitesimally thin layer (discontinuity in n) gives rise to a scattering-angle dependence of scattered power which is very close to the $-\frac{11}{3}$ law obtained for homogeneous isotropic inertial subrange turbulence. A layer of finite thickness results in an oscillatory dependence of the reflection coefficient on the scattering angle. The thicker the layer is, the more rapid are the oscillations. When the layer thickness approaches infinity, i.e., when we remove the upper knee of the profile, the oscillatory angular dependence disappears since we no longer get interference between the two boundaries. The result is a smooth angular spectrum given by

$$|\varrho|^2 = \left(\frac{dn}{dh} \frac{\lambda}{8\pi \sin^3 \theta/2} \right)^2 \tag{11}$$

i.e., $$P(\theta) \sim \theta^{-6} .$$

We may conclude, therefore, that a single atmospheric layer gives rise to angular dependences varying from θ^{-4} - θ^{-6} depending on the layer thickness. The power scattered in a given direction is determined by layer thickness and by the change in refractive index through the layer.

However, no single layer can give an angular dependence weaker than that corresponding to the θ^{-4} law. Referring to Figures 1 and 2, we see that the single layer assumption allows us to explain approximately 50% of the experimental results. The results giving a scattering angle dependence weaker than the θ^{-4} law cannot be explained on the basis of a single-layer model.

(c) Finally we shall consider the spatially intermittent type structure shown in Figure 3c. We shall see to what extent such a structure influences the angular power spectrum.

In order to simplify the treatment, we shall assume that the variance of the refractivity irregularities through the turbulent stratum is given by a $(\sin x)/x$ relationship and that the spectrum of the irregularities can be written in the form K^{-n}.

The resultant spectrum is a convolution integral where the K^{-n} spectrum is convolved with the spectrum of the $(\sin x)/x$ filter function. The spectrum of the $(\sin x)/x$ filter is a rectangular function. The width of this rectangular filter spectrum is taken to be $2K'$ and the density A is taken as $\frac{1}{2} K'$ such that the integral of the filter spectrum

becomes unity. The power spectrum of such a turbulent stratum then becomes

$$E(K) = \int_{K-K'}^{K+K'} ACK^{-n} \, dK .$$

Solving this simple integral we get

$$E(K) = AC\left[2K'K^{-n} + \frac{2}{3!}(1-n)(-n-1)K'^3K^{-n-2} + \frac{2}{5!}[(1-n)(-n-1)(-n-2)(-n-3)K'^5K^{-n-4}] \right].$$

Choosing then $n = 4 \approx \frac{11}{3}$ we get

$$E(K) = K^{-4}\left[1 + 10/3\left(\frac{K}{K'}\right)^{-2} + 7\left(\frac{K}{K'}\right)^{-4} + \cdots \right]. \tag{12}$$

Figure 5 shows a graphical representation of this equation. We see that unless the thickness of the stratum is less than 2 or 3 times the projected wavelength $\lambda/\sin\theta/2$, the spatial intermittency of the refractive index irregularities has no influence on the angular spectrum of the scattered wave.

Furthermore, we know that all irregularities within the scattering volume contribute to the scattered field strength at the receiver. A very thin turbulent layer must therefore have a very large variance in order to give a contribution which is comparable with that of the background turbulence in which the stratum is assumed to be embedded.

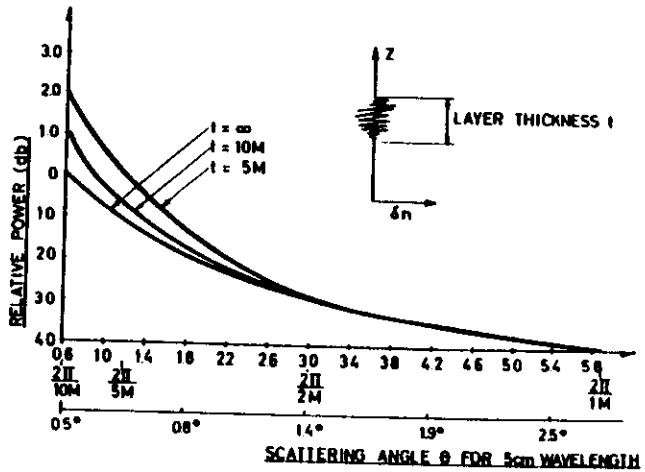

Fig. 5. Angular power spectrum of a scattered wave resulting from a thin stratum of intense turbulence.

Finally, we see from Figure 5 that the existence of one turbulent layer results in a spectrum slope which is steeper than that one would have with $-\frac{1}{3}$ law homogeneous turbulence. Thus we are still not able to explain all the weak angular dependence results of Figures 1 and 2.

Before proceeding to discuss the potential of other forward scatter techniques we shall investigate what beamwidth requirements are related to a beamswinging experiment (angle of arrival measurements) for this to be meaningful. One requirement, obviously, is that the beamwidth of the probing antenna must be smaller than the width of the scattered beam.

If n be the exponent of the angular power-spectrum θ^{-n} and $a_{1/10}$ the 10-db width of the scattered beam, then this beamwidth is given by

$$a_{1/10} = \frac{d}{2a}(10^{1/n} - 1), \tag{13}$$

where d is the path length and a the effective Earth radius. Taking d, as an example, to be 200 km and $a = 6.3 \times 10^3$ km, we find that

$$a_{1/10} = 0.9(10^{1/n} - 1)\,\text{deg}.$$

Considering then a narrow angular spectrum corresponding to $n = 6$, we find that

$$a_{1/10} = 0.5^\circ$$

The relationship between beamwidth a and antenna aperture diameter D is given by

$$a = \frac{\lambda}{D}\,\text{rad}.$$

In order to achieve a 0.5° beamwidth, therefore, a 100-wavelength aperture is needed.

However, as we have seen, it is likely that unless we make the vertical extent of the scattering volume comparable with the thickness of the layer that we wish to investigate, the background turbulence, or the inclusion of several layers, is likely to mask the effect of the phenomenon that we are investigating. Therefore, in order to sort out the single layer by beamswinging techniques, we shall have to resolve a volume the vertical extent of which is limited to perhaps a few tenths of meters. With a 200-km path length we shall then need a beamwidth

$$a = \frac{10\text{ m}}{100\text{ km}} = 10^{-4}\,\text{rad}.$$

This will require a 10^4 wavelength aperture or an interferometer arrangement with a $10^4\ \lambda$ baseline. Such an arrangement obviously is not very practical.

In conclusion, we note that the spatial resolution of a forward scatter beamswinging experiment is very much inferior to that of a vertically pointing backscatter radar arrangement where the vertical resolution essentially is determined by the pulse width of a pulsed radar (15 m for a 0.1 μs pulse radar) and by the bandwidth of a random noise radar or FM-CW radar.

One important feature of the forward scatter system, however, is its superior sensitivity. The sensitivity of a forward-scatter system is a factor $\theta^{n}/2$ better than that of a backscatter system. Here n again is the slope of the irregularity spectrum. For $n = 4$ and a typical scattering angle of a few degrees, we see that the forward scatter system can detect irregularities some 40–50 db weaker than those of a back-scatter system, all factors being equal.

It should be pointed out that in so far as the above discussion is related to a practical beamswinging experiment performed in the vertical plane, the discussion is somewhat hypothetical. Obviously, in order for a simple beamswinging experiment to give information about the cross-sectional structure of a layer, this layer must be inside the scattering volume for all the scattering angles employed. With regard to a purely vertical beamswinging experiment, this cannot be achieved with one set of antennas.

The current discussion should therefore largely be regarded as a discussion of the influence of a given layered structure on the angular power spectrum of the scattered wave. As such, it forms the basis of the subsequent sections.

3.2. Multifrequency Experiments

Consider now the experiment involving simultaneous transmission and reception on two widely separated frequencies and scaled antennas. If the antenna beams are narrow such that the scattering volume is determined by beam geometry and not by the scattering mechanism, then the scattering volumes for the two frequencies are identical. Measuring then the ratio of the power received on the two frequencies, we get information about the refractive index spectrum along a vertical direction within the scattering volume. Writing this spectrum as $\Phi(K) \sim K^{-n}$, the power ratio is simply given by

$$\frac{P(\lambda_1)}{P(\lambda_2)} = \left(\frac{\lambda_1}{\lambda_2}\right)^{n-2} \tag{14}$$

If the received power is normalized with respect to the free-space transmission loss, the corresponding power ratio becomes

$$\frac{\dfrac{P}{P_{FS}}(\lambda_1)}{\dfrac{P}{P_{FS}}(\lambda_2)} = \left(\frac{\lambda_1}{\lambda_2}\right)^{n-4} \tag{15}$$

We see that atmospheric refraction does not enter the equation in this case. This is a feature which makes the multi-frequency experiment a very attractive one in the study of the characteristic properties of the irregularity structure. Note, however, that as in the beamswinging case, we measure the combined effect of background turbulence, the contribution from whatever layer structure may be present within the scattering volume and from localized strata of intense turbulence. Even if we employ large antennas, the vertical region in the atmosphere inherently involved is large.

3.3. Field strength correlation measurements

We have a wide-beam transmitter radiating its power essentially in a horizontal direction. The resulting scattered wave is received by two nearly identical, small aperture, receiving antennas positioned beyond the horizon relative to the transmitter.

The antennas are spaced vertically or horizontally such that the centre line through the receiving antennas is normal to the line through the transmitter and the receivers. We measure the normalized complex correlation of the voltages induced in the antennas.

It can readily be shown (Gjessing and Børresen, 1968) that this spatial field-strength correlation function is the Fourier transform of the angular power spectrum of the wave reaching the receiving antennas. Thus if the antennas are spaced vertically, the correlation distance of field strength gives us information about the angle-of-arrival spectrum in the vertical plane. Similarly, horizontally spaced antennas give us information about the angular spectrum in a horizontal plane.

It is important to note that in this experiment we cannot use narrow beams. If we do, we shall essentially be measuring our own beamwidths. Referring to Gjessing (1969) for details, it can be shown that the vertical correlation distance is given by

$$\frac{L_v}{\lambda} = 0.44 \frac{a}{d}(2^{1/n} - 1)^{-1} \tag{16}$$

and the horizontal correlation distance

$$\frac{L_H}{\lambda} = 0.44 \frac{a}{d}(4^{1/n} - 1)^{-1/2}, \tag{17}$$

where a is the effective Earth radius (i.e., refraction effects are important), d the path length and n the slope of the irregularity spectrum within the scattering volume ($\Phi(K) \sim K^{-n}$). The vertical correlation distance is determined by the vertical component of the three-dimensional spectrum whereas the horizontal correlation distance is governed by the spectrum along a direction which is determined by the length of the path. For a line of sight path (if a scatter experiment could be realized on such a path), it is the horizontal component of the three-dimensional spectrum that matters. If the path length is large, it is the component along a direction which is close to being vertical that has the dominating influence (Gjessing, 1962).

In conclusion we note:

(a) Refraction effects have a marked influence on the structure deductions in a field-strength correlation experiment (see Equations (16) and (17)).

(b) A correlation experiment measures inherently the spectral characteristics of the structure averaged over a large volume in space. One single sharp discontinuity in refractive index will, as we have seen, give a θ^{-4} angular power spectrum and hence essentially the same vertical correlation distance as that resulting from homogeneous isotropic inertial subrange turbulence.

3.4. Coupling loss measurements

From basic antenna theory we know that the free space antenna gain is proportional to the antenna aperture ($G = 4\pi A/\lambda^2$).

When dealing with large antennas on a troposcatter circuit the linear relationship no longer holds. The reason is the limited correlation distance of field strength over the receiving aperture. If the correlation distance of field strength is smaller than the antenna aperture, the antenna no longer behaves as a normal aperture antenna, and we are experiencing a gain deficit. This apparent gain degradation is commonly referred to as antenna-to-medium coupling loss.

It can readily be shown (Gjessing, 1969) that this loss is inversely proportional to the product of the vertical and horizontal correlation distances. The gain loss G_L is given by

$$G_L = \frac{A}{L_v L_H} = \frac{5(2^{1/n} - 1)(4^{1/n} - 1)^{1/2} A}{(a/d)^2 \lambda^2} \tag{18}$$

Note that this equation is based on the assumption that the transmitting antenna beam is broad both in azimuth and elevation and the receiving beam narrow in both planes. This condition is necessary for the influence of the atmospheric structure on the gain loss to be a maximum.

For other antenna configurations see Waterman (1958a).

As regards the potential of this technique as a diagnostic tool in the study of turbulent layers, the same arguments apply as those presented when discussing correlation distance measurements. We note, however, that in the case of coupling loss measurements, the influence of refraction is very marked (the effective Earth radius a appears in the second power) so that it becomes imperative to know the mean refractive index gradient in order to determine the spectral characteristics from the measurement of coupling loss.

3.5. Time delay measurements

The experiments we have discussed so far, all measure, directly or indirectly, the angular power spectrum of the scattered wave. We have seen that the two extreme structure categories, homogeneous $-\frac{1}{3}$! law turbulence and single, infinitesimally thin layer, give angular spectra which for all practical purposes are indistinguishable.

Admittedly there are special sets of e.g., beamswinging experiments, that at least in principle can reveal the differences (see e.g., Gjessing, 1962) but on the basis of simple single experiments and reasonable beamwidths, it is very difficult to analyse a single-layer structure.

The two remaining experiments to be discussed, time delay and bandwidth measurements, do not rely on the angular power spectrum but on the delay spectrum. Using wide-beam antennas on either end such that the multipath transmission is governed by the scattering mechanism rather than by beam geometry, we seek an expression relating path length l and the position in space of the scattering element (layer). Note

that the loci of constant delay in a forward scatter experiment are concentric ellipsoidal surfaces having the transmitting and receiving points as foci. Discussing then layers which are predominantly horizontal, we see that those in the neighbourhood of the mid-path point of interest in a forward-scatter experiment coincide with the constant-delay surface. It is thus essentially the vertical distribution of scatterers we resolve in a pulse-delay experiment.

Simple geometry shows that if θ is the scattering angle corresponding to a given path length l, and d the length of the chord between the transmitter and the receiver, then l and θ are related by the following equation

$$\theta = 2\left[\left(\frac{l}{d}\right)^2 - 1\right]^{1/2}. \tag{19}$$

Differentiating this equation so as to get an expression for $dl/d\theta$, we find the following relationship between $\Delta\theta$ and Δl.:

$$\Delta\theta = \frac{4l}{d^2\theta}\,\Delta l. \tag{20}$$

Neglecting second-order terms and putting $\Delta\theta = \Delta z/(d/2)$ and $\theta = d/a$, where Δz is the height coordinate measured from the intersecting point of the two tangent planes through T and R, and a, as usual, is the effective Earth radius, we get the following expression

$$\Delta l \approx \frac{2d}{a}\,\Delta z. \tag{21}$$

We see that in a pulse-delay experiment (bistatic radar) the space resolution is a factor $2d/a$ inferior to a backscatter radar experiment. Note however that the sensitivity of the bistatic radar is a factor $\sin^n\theta/2$ (where n is the exponent of the three-dimensional refractive index spectrum $\Phi(K)\,K^{-n}$) better than backscatter radar. Thus the forward-scatter experiment will reveal much weaker irregularities than the back-scatter experiment. If then the refractive index irregularities are limited to a layer or thin strata of thickness Δz, then a delta pulse transmitted at T will appear as a broadened pulse, or a spectrum of delta pulses at R, and the width of this delay spectrum is given by

$$\Delta\gamma = \frac{\Delta l}{c} = \frac{2d}{ac}\,\Delta z, \tag{22}$$

where c is the wave velocity.

As an example, consider a 200-km path and a thickness of the turbulent strata of 10 m. From Equation (21) we then see that path length difference Δl will be

$$\Delta l = \tfrac{1}{5}\Delta z$$

i.e., the space resolution is degraded by a factor of 15 relative to a back-scatter radar. The width of the delay spectrum $\Delta\gamma$ associated with a 10-m thick stratum will then be

$$\Delta\gamma \approx 2 \times 10^{-3}\ \mu\text{s}.$$

In order to resolve this layer, we shall thus need a transmitted pulse which is shorter than 2 ns. Using a random noise modulated radar transmitter and coherent detection techniques, we shall need a noise bandwidth which is in the order of

$$\Delta F = \frac{1}{\Delta\gamma} = 500\ \text{MHz}.$$

Assume now, as we have done previously, that the thin layer is embedded in a background of turbulence and that this turbulence gives rise to a $-\frac{1}{3}!$ law refractive index irregularity spectrum. We have previously shown (Gjessing, 1969) that the $1/e$ width of the delay spectrum resulting from a homogeneous irregularity spectrum is given by

$$\Delta\gamma = \frac{d^3}{8a^2c}\left(e^{2/n} - 1\right), \tag{23}$$

where n is the slope of the irregularity spectrum. This should be $\frac{1}{3}!$ for homogeneous isotropic inertial subrange turbulence. Using the same path geometry as in the above example, we find from Equation (23) that the width of the delay spectrum resulting from the background turbulence is

$$\Delta\gamma = 60 \times 10^{-3}\ \mu\text{s}.$$

This is a factor 30 relative to the delay spectrum width resulting from a 10-m thick layer. The background turbulence, however, will give a particular decrease in intensity with increasing delay whereas a thin layer of large refractive index variance will give a well defined peak in the delay spectrum. Given a sufficiently short transmitted pulse, therefore, it should in principle be possible to identify a thin layer in a background of turbulence.

The results from rake tropospheric scatter techniques are promising in this respect (Birkemeier, 1972).

3.6. Bandwidth measurements (frequency sweep experiments)

Our interest is now finally focused on the bandwidth properties of a scattered wave in relation to the particular atmospheric structures under consideration. The transmitter frequency is varied over a small frequency band at a rate which is large by comparison with the rate at which the atmospheric structure changes. At the receiver we measure the power as a function of frequency, sweep by sweep, and we find that this in general is a strongly varying function.

The data thus obtained can be analysed in several ways. One method involves computing the autocorrelation function in the frequency domain by using the ensemble of frequency sweeps as a basis. Another involves measuring simultaneously the average power at a large number of frequencies within the range over which the

frequency is varied, thus obtaining the average power-vs.-frequency relationship.

We have previously shown (Gjessing, 1969) that there is a simple relationship between the width of the delay spectrum and the bandwidth. If $\Delta\gamma$ is the width of the rectangular delay spectrum resulting from a layer of thickness Δz, then the bandwidth Δf is given by

$$\Delta f = \frac{1}{\Delta\gamma} = \frac{c}{\Delta l}.$$

From Equation (22) above then, we get

$$\Delta f = \frac{ac}{2d\Delta z}. \tag{24}$$

On the basis of the previous example with a 10-m thick layer within the scat ering volume limited by broad beams and a 200-km path, we find that the bandwidth

$$\Delta f = 500\ \text{MHz}.$$

Thus, in order to resolve a 10-m thick layer by a frequency sweep experiment, we shall have to change the frequency rapidly over a 500 MHz band.

Then let us consider the bandwidth limitation resulting from the background turbulence. Referring to Gjessing (1969) for details, it can be shown that this bandwidth is given by

$$\Delta f = \frac{8a^2c}{2\pi d^3(e^{4/n} - 1)}. \tag{25}$$

For $n = \frac{1}{3}$ (inertial subrange turbulence) we find that the bandwidth corresponding to a 200-km path is

$$\Delta f = 1.2\ \text{MHz}.$$

We see that the contribution to the bandwidth of the background turbulence is very small compared with that of a thin layer.

3.7. Measurement of Air Velocity from Doppler Measurements

A discussion of the potentials of forward scatter techniques in the study of turbulent layers is not complete unless Doppler measurements are included. Doppler measurements are only discussed elsewhere (Ottersten *et al.*, 1973; Birkemeier, 1972) and will therefore be mentioned very briefly in this presentation.

When discussing Doppler measurements, one must distinguish between the post-detection intensity-fluctuation spectrum $S(F)$, which essentially is a measure of the Doppler spread, and the pre-detection spectrum $S(f)$ which includes the Doppler shift.

The relation between the two spectra is given by (Atlas, 1969) as:

$$S(F) = \int_{-\infty}^{\infty} S(f)\,S(f + F)\,df.$$

The Doppler spread gives us information about the combined effect on the Doppler broadening of the cross-path component of the mean wind V and the spatial variation of the wind δV within the scattering volume. It can be shown (Gjessing, 1962) that the Doppler broadening is given by

$$\delta F = \frac{1}{\lambda}(V\beta + \delta V\theta),$$

where β is the beamwidth if the scattering volume is homogeneously filled with scatterers. If the scattering is constrained to a thin layer of thickness Δz, then β is essentially $\Delta z/(d/2)$, where d is the path length.

If, however, we have access to the absolute Doppler frequency at the receiver, i.e., we can measure not only the Doppler spread, but also the shift F_0, we can obtain information about the mean cross-path wind by pointing narrow-beam antennas off the great-circle bearing by an amount α which should be at least a couple of beamwidths.

The horizontal cross-path component of the mean wind is then given by

$$F_0 = \frac{2V}{\lambda}\alpha.$$

On the basis of the rake delay and Doppler measurements, we can in principle measure the Doppler shift (i.e., the mean wind) associated with any given delay (i.e., vertical position of scattering element) and thus get information about the vertical velocity distribution of the scatterers (wind shear). The degree to which this Doppler technique is powerful in the study of turbulent layers depends on the delay- and Doppler resolution. New random-pulse Doppler radar techniques appear to be very promising and could conceivably also be applied in forward-scatter experiments (McGillem *et al.*, 1969).

4. Conclusions

Table I summarizes the theoretically obtained relationships pertaining to forward scattering from turbulence and from stratified layers.

We have seen that the first six groups of experiments (viz., beamswinging, multi-frequency experiments, correlation experiments and experiments involving the measurements of coupling loss) all essentially measure the angular power spectrum of the scattered wave. Furthermore, when comparing the effect on the scattered wave of background homogeneous $-\frac{1}{3}$ law turbulence with that of the limiting case of a thin layer, namely a step-discontinuity in the vertical refractive index profile, we see that the angular power spectra are essentially identical ($P(\theta) \sim \theta^{-11/3}$ and $P(\theta) \sim \theta^{-4}$, respectively). Hence by means of the group of experiments in their simplest form here discussed, one cannot distinguish between a thin layer and homogeneous turbulence. There are experimental refinements, such as beamswinging refinements (Gjessing, 1962) which increase the diagnostic potential of the simple techniques considerably. Still, the six techniques do not appear to lend themselves readily to the

TABLE I

Some theoretical relationships pertaining to forward scattering from turbulence and stratified layers

	Type of structure / Type of experiment	Background turbulence	Thin layer
Measure angular power spectrum of scattered wave	Beamswinging	$\frac{P(\theta)}{P(\theta_0)} = \left(1 + \frac{\theta}{d/a}\right)^{-(11/3+1)}$	$\frac{P(\theta)}{P(\theta_0)} = \left(1 + \frac{\theta}{d/a}\right)^{-4}$
	Multifrequency	$\frac{P(\lambda_1)}{P(\lambda_2)} = \left(\frac{\lambda_1}{\lambda_2}\right)^{11/3+2}$	$\frac{P(\lambda_1)}{P(\lambda_2)} = \left(\frac{\lambda_1}{\lambda_2}\right)^{4+2}$
	Vertical E-correlation	$\frac{L_v}{\lambda} = \frac{0.44\,a}{d(2^{2/11}-1)}$	$\frac{L_v}{\lambda} = \frac{0.44\,a}{d(2^{1/4}-1)}$
	Horizontal E-correlation	$\frac{L_H}{\lambda} = \frac{0.44\,a}{d(4^{2/11}-1)^{1/2}}$	$\frac{L_H}{\lambda} = \frac{0.44\,a}{d(4^{1/4}-1)^{1/2}}$
	Coupling loss	$G_L = \frac{5A(2^{2/11}-1)(4^{2/11}-1)^{1/2}}{(a/d)^2\lambda^2}$	$G_L = \frac{5A(2^{1/4}-1)(4^{1/4}-1)^{1/2}}{(a/d)^2\lambda^2}$
Measure vertical distribution of scatterers	Pulse delay	$\Delta\tau = \frac{d^2}{8a^2c}(e^{\theta/11}-1)$ 200-km path $\Delta\tau = 60$ ns	$\Delta\tau = \frac{2d}{ac}\Delta h$ 200-km path, $\Delta h = 10$ m $\Delta\tau = 2$ ns
	Bandwidth	$\Delta f = \frac{8a^2c}{2\pi d^2(e^{\theta/11}-1)}$ 200-km path $\Delta f = 1.2$ MHz	$\Delta f = \frac{ac}{2dh}$ 200-km path, $h = 10$ m $\Delta f = 500$ MHz

study at hand. We have also seen that increasing the layer thickness (the way the layer is defined in this presentation) leads to an increase in the spectrum slope. Making the layer very thick in terms of the wavelength, we get a scattering angle dependence approaching the θ^{-6} law.

The existence of a layer, or layers, through which the mean refractive index varies linearly, will therefore explain all the steep-slope spectra observed experimentally (Figures 1 and 2). Such layers will not, however, explain the spectra corresponding to a scattering-angle dependence weaker than that corresponding to the θ^{-4} law. Neither can we explain the weak slope on the basis of thin turbulent strata (space intermittent turbulence) since such strata modify the spectrum only if the thickness is comparable with the projected wavelength and then the stratum adds to the steepness of the spectrum slope. In order to explain the weak scattering-angle dependences, we must have components contributing to the high wave-number end of the spectrum,

i.e., intensity enhancement at scales $2\pi/k$ in the order of fractions of a meter. A large number of layers with a predominant separation of less than a meter will result in slopes weaker than that corresponding to the $-\frac{1}{3}$ law. Whether such layers, from a fluid dynamics point of view, can exist is a matter which is outside the scope of this presentation.

Referring to Table I again we see that the effect of atmospheric *refraction* in some cases is of dominant importance (see e.g., horizontal correlation distance where the influence of a is comparable with that of n). This means that unless we measure the mean refractive index profile from the ground up to the top of the scattering volume, in some manner, we cannot draw definite conclusions regarding the slope n of the irregularity spectrum. The distribution curves of Figures 1 and 2 may therefore, depending on the value of the refraction parameter a, have to be shifted along the n-axes. However, the two-frequency experiments referred to in Figure 2 are not affected by a. Similarly, in the beamswinging experiments of Gjessing *et al.* (1969) the refraction effects have been taken into consideration. We are therefore still faced with the problem of explaining the results giving n-values which are smaller than 4 and see from Figures 1 and 2 that 50% of the results give such n-values.

The two last groups of experiments listed in Table I (delay and bandwidth measurements, respectively) measure essentially the vertical distribution of the scatterers and not the angular power spectrum.

In a study of layered structure where our interest is focused on the vertical refractivity distribution rather than on the averaged spectral properties of the structure, this last category of experiments appears to represent a powerful tool. We have seen that a 10-m thick layer will give rise to a delay spectrum the width of which is some 2 ns, whereas that of $-\frac{1}{3}$ law turbulence will give us 60 ns on a 200-km path. Similarly a 10-m layer will give us a 500-MHz bandwidth whereas the background turbulence is responsible for only some 1–2 MHz.

Therefore, if we can transmit very short pulses, or subject the transmitter to wideband frequency modulation, we can in principle resolve these layers in a background of turbulence. The limiting factor will probably be that of sensitivity. Unless the receiver is turned in synchronism with the FM transmitter, we shall need a very wideband receiver and suffer a corresponding loss in sensitivity. Similarly, in order to receive, by conventional techniques, a short pulse, we shall need a large receiver bandwidth. Modern coherent, or correlation detection techniques, however, constitute a remedy for many of these shortcomings.

References

Atlas, D.: 1969, 'The Measurement of Crosswind by Noncoherent Dual Beam Bistatic Radio Tropo-Scatter Techniques', Tech. Rep. 10, Laboratory for Atmospheric Probing, University of Chicago, Ill.

Birkemeier, W. P.: 1972, 'A Study of Tropospheric Refractive Structure and Winds Using Over-the-Horizon Rake Radar', Tech. Rep. 10, Laboratory for Atmospheric Probing, University of Chicago, Ill.

Bolgiano, R. Jr.: 1964, 'A Study of Wavelength Dependence of Transhorizon Radio Propagation', Cornell Univ. Res. Rep. 188, Ithaca, N.Y.

Bull, G. and Neisser, J.: 1968, 'Untersuchungen der Atmosphärischen Feinstruktur mit Hilfe von Ausbreitungsmessungen im Mikrowellenbereich', *Beitr. Geophys.* 77, 394–410.
Eklund, F. and Wickerts, S.: 1968, 'Wavelength Dependence of Microwave Propagation far Beyond the Radio Horizon', *Radio Sci.* 3, 1066–1974.
Gjessing, D. T.: 1962, 'Determination of Permittivity Variations in the Troposphere by Scatter Propagation Methods', *Proc. IEE, London* 109, 446–456.
Gjessing, D. T.: 1964, 'Determination of the Isotropy Properties of the Tropospheric Permittivity and Wind Velocity Fields by Radio-Propagation Methods, *J. Geophys. Res.* 69, 569–581.
Gjessing, D. T. and Irgens, F.: 1964, 'On the Scattering of Electromagnetic Waves by a Moving Tropospheric Layer Having Sinusoidal Boundaries', *IEE Trans.* 12, 51–64.
Gjessing, D. T. and Borresen, J. A.: 1968, 'The Influence of an Irregular Refractive Index Structure on the Spatial Field-Strength Correlation of a Scattered Radio Wave', *IEE (London) Conf. Pub.* 48, 43–50.
Gjessing, D. T.: 1969, 'Atmospheric Structure Deduced From Forward Scatter Wave Propagation Experiments', *Radio Sci.* 4, 1195–1210.
Gjessing, D. T., Kjelaas, A. G., and Nordo, J.: 1969, 'Spectral Measurements and Atmospheric Stability', *J. Atmos. Sci.* 26, 462–468.
Grosskopf, J.: 1968, 'Investigation of the Receiving Field for Scatter Propagation', *AGARD Conf. Proc.* 37, 22-1 to 22-11.
McGillem, C. D., Cooper, C. R., and Waltman, W. B.: 1969, 'Use of Wideband Stochastic Signals for Measuring Range and Velocity', *Easton 69 Record*, 305–311.
Ottersten, H., Hardy, K. R., and Little, C. G.: 1973, 'Radar and Solar Probing of Waves and Turbulence in Statically Stable Clear-Air Layers', *Boundary-Layer Meteorol.*, this issue, p. 87–89.
Saxton, J. A., Lane, J. A., Meadows, R. W., and Matthews, P. A.: 1964, 'Layer Structure of the Troposphere', *Proc, IEEE* 111, 2.
Seehars, H. D.: 1970, 'Investigation of the Dielectric Turbulence and Wind Stratification in the Troposphere by Means of SHF Beamswinging Experiments over Sea', Berichte Nr. 18 des Instituts für Radiometeorologie und Maritime Meteorologie an der Universität Hamburg.
Wait, J. R.: 1964, 'A Note on VHF Reflection from a Tropospheric Layer', *Radio Sci.* 7, 84–848.
Waterman, A. T., Jr., Gjessing, D. T. and Liston, C. L.: 1961, 'Statistical Analysis of Transmission Data From a Simultaneous Frequency- and Angle Scan Experiment', Paper presented at the URSI Spring Meeting, Washington, D.C.
Waterman, A. T., Jr.: 1958a, 'Some Generalized Scattering Relationships in Transhorizon Propagation', *Proc. IEE* 46, 1842–1848.
Waterman, A. T., Jr.: 1958b, 'A Rapid Beamswinging Experiment in Transhorizon Propagation', *IRE Trans.* 6, 338.

HYDROSPHERIC AND ATMOSPHERIC DIAGNOSTIC METHODS BASED ON ELECTROMAGNETIC WAVES

A brief description of a set of experimental methods

by

Dag T Gjessing

Royal Norwegian Council for Scientific and Industrial Research
Environmental Surveillance Technology Programme

and

University of Tromsö
Institute of Mathematical and Physical Sciences

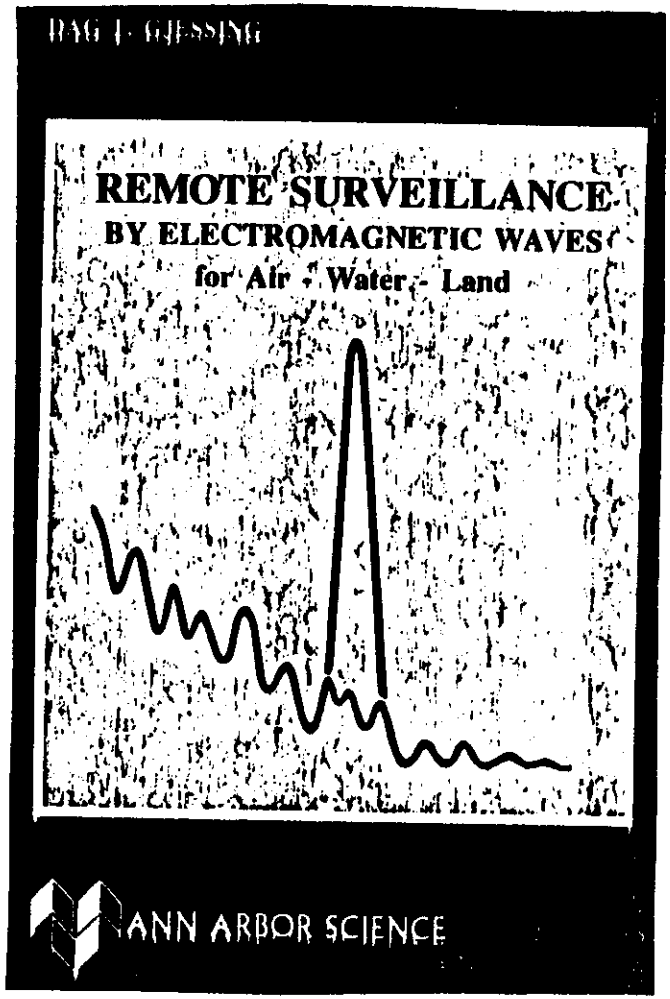

CHAPTER 6

PRESENT STATE-OF-THE-ART A DESCRIPTION OF A SET OF ENVIRONMENTAL SURVEILLANCE METHODS

In Chapter 5 on methodology, we discussed general asepcts of remote sensing. On the basis of a set of methods developed in the field of radio science, we have presented a methodology for remote sensing of environmental factors. To complete the picture, a representative set of available environmental surveillance methods must be presented. Obviously, to give a comprehensive account of the techniques available today would require a great deal of space. The objective of this chapter is to give a condensed review of a selected set of important techniques. This does not necessarily imply that a technique which is important from the user's point of view, in that it solves important problems, will be given the greatest emphasis. The selection is made on the basis of the novelty of the technique and on the degree to which it is exciting to the author. Clearly then, the selection will be a subjective one; some readers will no doubt search in vain for techniques they consider important. The author hopes, however, that only a few of the interesting remote probing methods have been omitted and that the reader, like the author, will be fascinated by most of those mentioned.

This author believes that the progress in the field of environmental surveillance by radio science methods is remarkable and most stimulating, probably because there is an urgent demand for such methods and at the same time the means to satisfy the demand have been acquired. The tools at our disposal are, to a

large extent, inherited from the radio scientist who addressed himself to problems in the troposphere (radio meteorology) and beyond into space.

Finally, it should be noted that the brief survey in this chapter is not the result of a comprehensive literature study. It is based largely on personal interviews with individual scientists who are experts in this field. However, it is hoped that the chapter will stimulate the reader and that it will be of aid to environmental researchers who are seeking powerful methods for environmental surveillance.

6.1 SEA SURVEILLANCE

Remote probing techniques aimed at measuring the conditions at or in the immediate vicinity of the sea surface will be considered.

6.1.1 Wind Close to Sea Surface

1. *Multifrequency Radiometry*
   (Dr. T. T. Wilheit, NASA Goddard Space Flight Center)

A nearly all-weather capability for measuring wind speed at the air/sea boundary can be obtained using a set of multifrequency radiometers at microwave frequencies. There are several factors affecting the radiance as viewed with microwave radiometers: the sea surface temperature, the roughening of the sea surface by the wind, and the composition and temperature of the intervening atmosphere. Each of these factors has its own characteristic spectrum and polarization properties.

This principle is to be exploited in the scanning multichannel microwave radiometer (SMMR) to be flown on the SeaSat-A and Nimbus-G satellites in 1978. These instruments will measure the microwave radiance at 6.6, 10.7, 18, 21 and 37 GHz at a nadir angle of 48° and in two linear polarizations. Sea surface wind accuracies of better than 2 m/s at standard height (19.5 m) are expected with a resolution of about 100 x 100 km. Aircraft-borne radiometric measurements of wind speed have been reported by Wilheit and Fowler and Webster *et al.* [30,31].

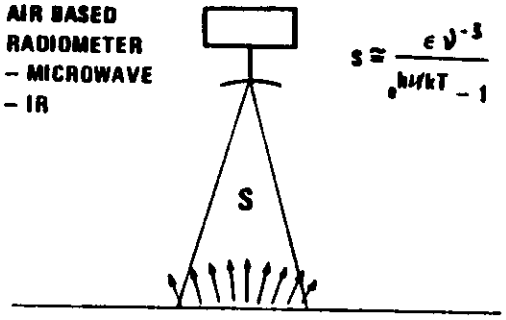

Figure 6.1 Principle of the radiometer for sea surface investigations. Emission coefficient ϵ is determined by surface structure and surface chemistry. Relative dependence varies with frequency. T is temperature and ν radiation frequency.

2. *Scatterometer*

In addition to the radiometer techniques, an active scatterometer is proposed for the measurement of surface wind speed. Whereas the radiometer system is most sensitive to wind speed in excess of 5 ms^{-1} (it responds to foam cover), the scatterometer is useful for wind speeds in the range 3-15 ms^{-1}. A combined scatterometer and radiometer will be flown in NASA SeaSat-A in 1978 [32].

The scatterometer operates at 14.6 GHz and illuminates the sea surface. The interference patterns received are analyzed in much the same way as in previous measurements of ionospheric irregularities. From this, wind speed can be deduced (range 3-15 m/s) The scatterometer illuminates the sea surface with four lobes, two lobes on either side of the spacecraft. By means of these sets of lobes information about the degree to which the sea surface motion is "frozen" can be measured.

6.1.2 Sea Surface Temperature
(Dr. T. T. Wilheit, NASA Goddard SPFC)

Microwave radiometers at five frequencies (6.6, 10.7, 18, 21 and 37 GHz) and two polarizations give a set of information on the basis of which sea surface temperature is obtained. The

accuracy in a satellite application is expected to be 1.5°K. The system offers all-weather capability. The sea surface resolution cell will be determined by the lowest frequency (6.6 GHz) and will be approximately 150 x 150 km. The five-frequency radiometer is based on a direct mixing superheterodyne receiver (*i.e.*, no RF preamplifier) with a noise factor of 5 dB. Long period averaging of received signals is essential. The sea surface temperature is essentially that at the surface, down to a millimeter or so. The reflection and transmission properties of the atmosphere must be taken into consideration (the emissivity of the sea at these frequencies is approximately 0.5, hence the reflectivity is also 0.5) [31].

Sea surface temperature is commonly measured by high resolution IR radiometry in the atmospheric window regions. Figure 6.2 illustrates its high variability, spatially and in time [33].

6.1.3 Sea Surface Salinity
(Dr. B. Kendall, NASA Langley Research Center)

NASA Langley (Bruce Kendall and H-J. C. Blume) measures sea surface salinity and temperature by the use of two airborne microwave radiometers (S- and L-band, respectively). The brightness temperature (power received at the radiometer) is a function of molecular temperature and salinity. In the S-band (2.65 GHz), temperature is the dominating parameter, whereas salinity dominates in the L-band (1.43 GHz). Using both frequencies and compensating for the influence of cosmic radiation, intervening atmosphere, sea surface roughness, and antenna beamwidth, accurate information about both temperature and salinity is obtained. The spatial resolution on the sea surface is approximately 3/10 of the height of the observation platform (the aircraft). Demonstrated absolute accuracy (by comparison with sea truth measurements) is 1/1000 for salinity and 1°K for temperature [34,35].

6.1.4 Atmospheric Surface Pressure Over Sea
(Dr. G. E. Peckham, Heriot-Watt University)

A method making use of the atmospheric transmission within the 5-mm oxygen absorption band is suggested by G. E. Peckham

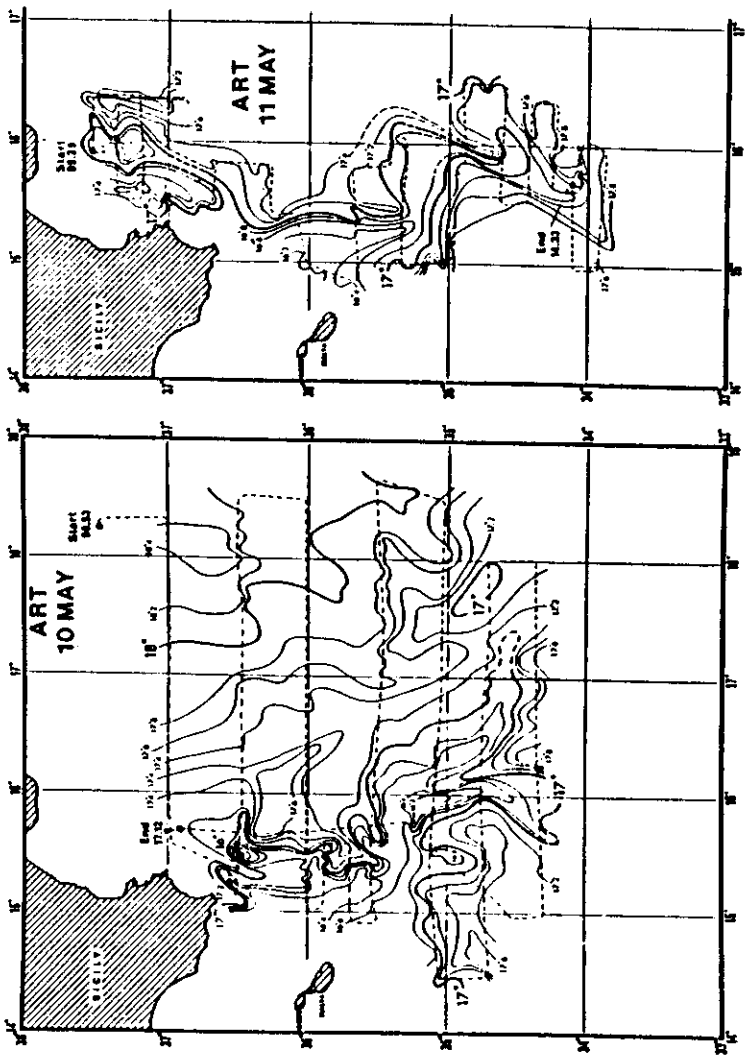

Figure 6.2 Corrected sea surface isotherms from ART measurements, May 10 and 11, 1972. After Briscoe, Johannessen and Vincenzi [33].

and D. A. Flower, Heriot-Watt University, Scotland (information from NASA). Intensities of signals at several frequencies in the 50 GHz region as reflected from the sea surface are used to allow for the variation in surface reflectivity and cloud and water vapor transmissivity. The method suggested could, when referred to accurate *in situ* measurements of pressure at certain points on the surface, give global coverage. Supplemented with information about atmospheric temperature as obtained by passive IR and microwave radiometers, the entire atmospheric pressure field can be deduced using the equation of hydrostatic balance. Based on a rather crude instrumentation (source power 3 W, antenna 30-cm diameter, receiver bandwidth 100 kHz, noise factor 10 dB) there appears to be no fundamental reason why ± 3 mb should not be achieved [36].

6.1.5 Precipitation Over Sea
(Dr. T. T. Wilheit, NASA Goddard SPFC)

Microwave radiometry viewing the sea surface from above (Nimbus 5) at 19.35 GHz gives information about rain rate with accuracy of about a factor of 2. The principle on which the method relies is emission from precipitation using the cold sea surface as reflector.

6.1.6 Surface Structure of the Sea

Present techniques for measuring sea state are centered on the use of HF radar for measuring sea state over an area of approximately 2 x 10 km² from a single station. It is anticipated that systems will be operational in the near future. Satellite techniques (see Section 6.3.2 on wind speed) based on combined microwave radiometer/scatterometer observations are under investigation, but considerable research is still needed, and a 10-to-15-year effort may be anticipated before this evolves into an operational system. About two years of experimental data gathering are required to complete the development stage of the HF system and to enable a decision on whether to implement it operationally. The two techniques are complementary in that the HF system has been shown to be cost-effective, even on a short-term basis; hence it

could fill in the gap before the satellite system becomes operational [37,38].

1. *Microwave Altimeter*
(Dr. A. Loomis, JPL)

NASA SeaSat-A will be performing studies of the general ocean current and dynamics. From these studies (dynamic topography) ridges as high as 1.5 m above mean sea level are to be expected (D. W. Van Arx, Woods Hole).

An altimeter designed at JPL has the following characteristics:

- Frequency is 13.9 GHz
- Pulse compression techniques give a range resolution of 10 cm
- Beamwidth enables spatial resolution of 1-km diameter on the sea surface. Taking the motion of the satellite into account, the resolution cell is 1 km x 7 km.

This system gives good waveheight statistics and absolute height calibration.

2. *Synthetic Aperture Radar (SAR) Imager*
(Dr. A. Loomis, JPL)

The SeaSat-A synthetic aperture radar imager has been mounted in a 990 Convair aircraft and has the following characteristics:

- Frequency is 1.275 GHz
- The system is focused, *i.e.*, it corrects for wavefront curvature
- Integrates up to one second (300-1000 pulses)
- Looks 20° from the vertical
- Resolution is 25 m in both directions
- Phase resolution is 3°
- Range to object (sea surface) to be imaged is up to 30,000 ft.

A laser is used with this instrument to measure slope distribution of ocean waves [32].

3. *Land-Based HF Radars*
(Dr. D. E. Barrick, WPL, NOAA)

The use of shore-based radars that propagate via the ionosphere appears to be an ideal solution to the problem of wide-area routine sea state monitoring. For example, a single backscatter radar located in Kentucky could observe sea scatter over the entire Atlantic coast out to a range of about 1200 nautical miles. The dominant (first-order Bragg scattering) contribution to the echo

from the sea surface at MF and HF arises from the ocean waves whose wavelength is exactly half that of the radar wavelength. Since these deepwater ocean waves have a phase velocity that bears a direct relationship to the wavelength L of the ocean wave ($v = \sqrt{gL/2\pi}$, where g is the acceleration of gravity), there is a particular Doppler shift Δf associated with the particular ocean wavelength L. This Doppler shift is given by

$$\Delta f = \pm\sqrt{\frac{g}{\pi\lambda}}$$

where λ is the HF wavelength since $L = \lambda/2$.

Finally it has been shown [37,38] that the strength of the first order echo (associated with a wavelength $L = \lambda/2$ and a Doppler shift Δf) is proportional to the height of the ocean wave. The following accuracies are expected: wave direction ± 15°, RMS height error 10%, wavelength 15%.

In order to obtain the whole spectrum of ocean waves, the HF frequency will be swept over an appropriate frequency range. The effect of the ionosphere is noticeable, all the frequency range to be used is obtained on the basis of ionograms. The influence of the ionosphere is under investigation. An example of a surface wave spectrum thus obtained is shown in Figure 6.3 [29,39].

4. *Two-Frequency*
Microwave Radar

The principles of the multifrequency technique were explained in Section 5.5. Dr. W. J. Plant, of the Naval Research Laboratory, Washington, D.C., has recently published experimental results using this technique. He used a coherent, dual-frequency CW X-band radar. The frequency difference Δf between sidebands could be adjusted between 7 and 150 MHz. The power spectrum of $E_1 E_2^*$ (product of the two detected signals) shows a low-frequency peak corresponding to the appropriate ocean wave component, plus a broad background (~ 100 Hz width) corresponding to the convolution of the single-frequency returns. The height of the low-frequency peak is a measure of the amplitude of the corresponding water wave. Figure 6.3 shows the wavespectra inferred. They correspond roughly to those determined by a wave gauge.

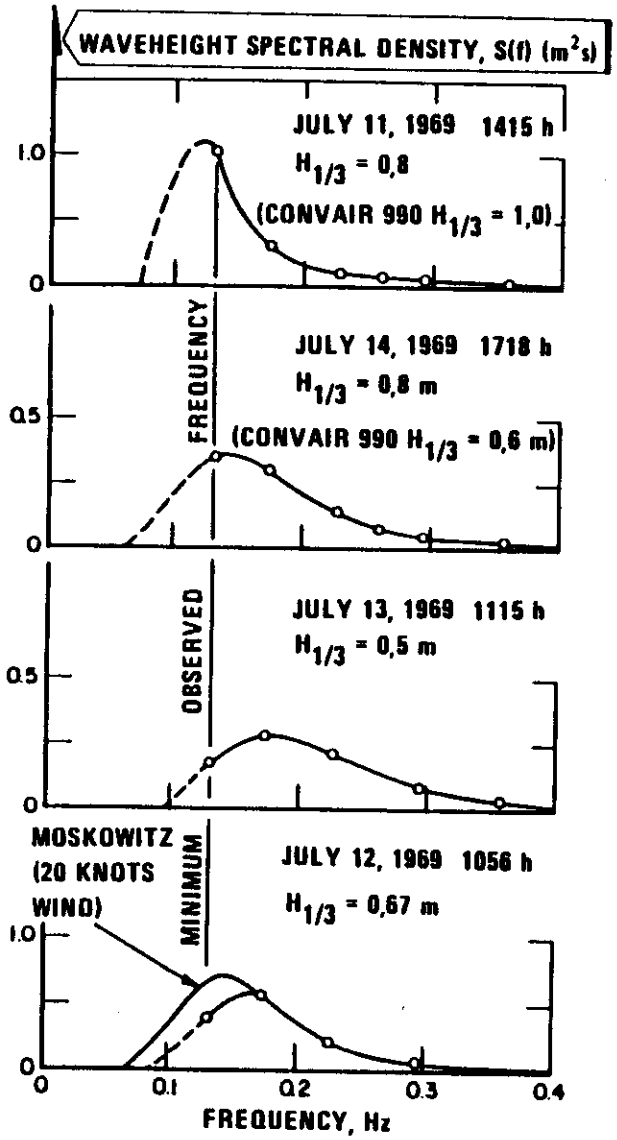

Figure 6.3 Temporal waveheight spectra deduced from MF/HF ground wave backscatter observations. After Crombie, 1971 [39].

Before the multifrequency principle can be applied to routine ocean observations, a better quantitative understanding must be gained about what influences the magnitude of the modulation signal. The primary backscatter comes from the capillary waves. Their interaction with the long gravity waves varies strongly. Thus, in Figure 6.4b the open circles indicate measurements after a change in wind direction. This change did not influence the gravity waves, so the wave spectrum component studied did not change. The modulated signal, however, increased by more than a factor of 2 [27,28].

6.1.7 Sea Surface Currents
(Dr. D. E. Barrick, WPL, NOAA)

Surface currents cannot be determined today by using the ionosphere as the reflector. Direct waves (ground waves), however, in the HF region, may be used (20 MHz). A small transportable system for rapid evaluation of the signals received out to a range of some 70 km has been developed. The spatial resolution is 3 km. This is obtained by range-gating (20 μs pulse width) and by measuring the phase and amplitude at four array elements of the receiving antenna, thus obtaining direction. It takes two different stations placed along the coast of interest to obtain the magnitude and direction of the current. The ocean coverage with a baseline of 40 km is 70 x 70 km (see Figure 6.5).

The system, which is referred to as CODAR (Coastal Ocean Dynamics Application Radar), has a peak transmitted power of 2.5 MW (average power 50 W) and the beamwidth is 180° with a three-element Yagi antenna. The system is controlled by a minicomputer (PDP 1134). To obtain good ground plane conditions for surface wave propagation, the antenna should be mounted close to the beach. This method enables measurement of the current at the sea surface to a depth approximately equal to $\lambda/8\pi$. With a frequency of 20 MHz this corresponds to 60 cm. The Doppler resolution capability of the system is 1/100 Hz, giving a surface current resolution of about 10 cm/s. These amplitude and current measurements open up the possibility of detailed studies of the dynamics of the ocean.

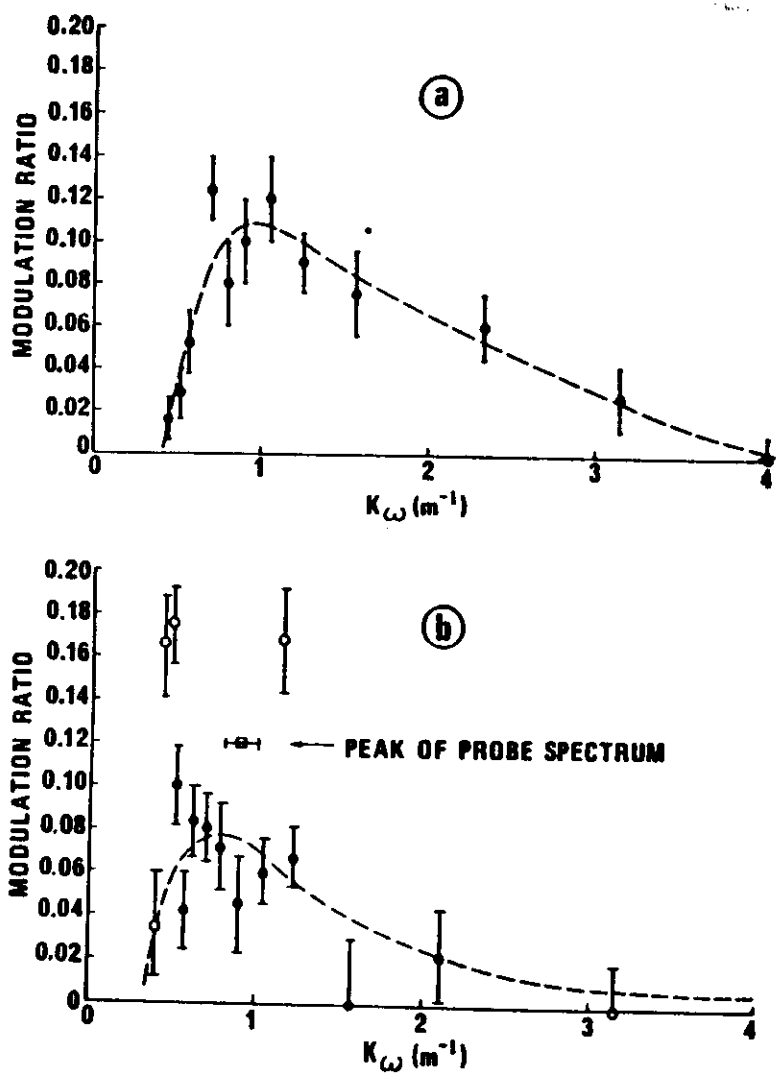

Figure 6.4 Intensity of gravity waves vs water wavenumber. (a) Data of April 10, 1975; (b) Data of June 11, 1975. Dashed lines are empirical. Square indicates wavenumber of peak of probe spectrum; its vertical placement is arbitrary. After W. J. Plant [27].

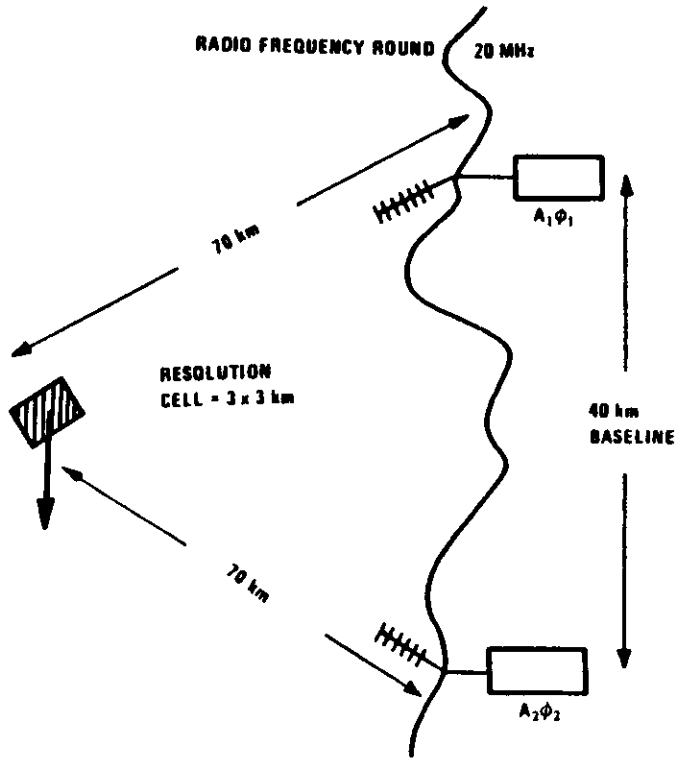

Figure 6.5 Remote probing of sea surface currents. Spatial resolution is 3 x 3 km; current resolution is approx. 10 cm/s.

6.1.8 Water Pollution

Several methods of potential interest will be presented.

1. *The Laser Fluorescence Methods*
   (Dr. M. Bristow, EPA, Las Vegas)

The area under investigation is illuminated with blue or ultraviolet radiation and the reemitted fluorescence is analyzed both in time and spectrally. The method is powerful for many applications:

- Study of plankton, algae and hence the effect of pollution due to domestic use of water, *i.e.*, phosphorus compounds.

- Remote sensing of oil spills: presence, extent and identification and characterization.
- Organic compounds in general in water. The total burden of organic compounds is measured (TOC). The Raman backscatter from water (which is relatively intense) is used as a reference standard with which to compare the fluorescent backscatter from pollutants. The fluorescence spectrum from pollutants in water does not possess a detailed "fingerprint." The spectrum is very broad and featureless.
- Water acidity (the pH value) can have an effect on the fluorescent spectrum. It could be that this is not a direct effect, but rather a secondary one. Acidity affects the organic compounds, which again are analyzed by laser fluorescence spectroscopy.
- For the purpose of tracking the motion of pollutants in a given area (effluent from rivers), fluorescent dyes are added to the water. These can be traced effectively even at very small concentrations with this method. The depth of penetration into the water is determined by the characteristic attenuation length and is generally about one meter. The fluorescence from sea water is much less pronounced than that from freshwater. Examples of spectroscopic measurements making use of the fluorescent mode are shown in Figure 6.6 [40-44].

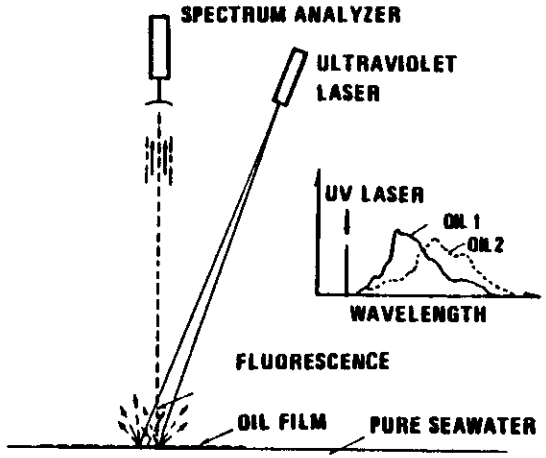

Figure 6.6 Study of surface water pollutants by the use of laser-induced fluorescence.

2. *Detection of Oil Spills by Radar*
(J. Nilsson, Swedish Defense Research Establishment)

It has been established experimentally that relatively small amounts of oil distributed on the ocean surface have a pronounced

effect on the ocean capillary waves and hence on the scattering of microwaves from the sea surface. Specifically, modifying the video processor in a conventional airborne weather and ground mapping radar results in the following typical detection performance of the radar.

- With a sufficient quantity of capillary waves (wind speed between 3 and 13 m/s) oil films of thickness of 3 μm can be detected.
- Wind statistics from the North Sea (1970) show that wind speed is less than 3 m/s 7.5% of the total time. For 11.5% of the time wind speed is above 13 m/s. Under such conditions of high wind speed most, if not all, detection methods fail.
- The radar will operate satisfactorily under all cloud conditions. Flying at a height of 3000 ft enables coverage of an area 100 km wide in one flight leg when viewing the sea surface with a depression angle greater than 1°. Until now, maximum detection range for oil has been 20-30 km.

Best contrast between an oil slick and pure sea water is obtained with upwind illumination favoring a side-looking radar configuration. Detection criteria based on polarization and on the time correlation properties and amplitude distribution statistics of the sea echo are being studied by H. Parr and A. Kjelaas, who are working with the author [45-49].

3. *Alternative Methods for Oil Spill Detection*

Ultimately, surveillance of oil spills will be based on multisensor systems because of the many possible interferents and the large variations in environmental conditions. Such an instrumental package may consist of:

- *Laser fluorosensor*
- *High-resolution TV* (an active, range-gated system is being developed for the U.S. Coast Guard by Naval Air Development Center).
- *Infrared linescan.* IR-imagery of oil slicks relies on differences in emissivity or temperature. Temperature differences between oil slick and sea water may be due to absorption of sunlight or vaporization of the lighter oil fractions.
- *Imaging microwave radiometer.* The elimination of capillary waves reduces the apparent emissivity in regions with thin (μm) continuous oil slicks. Thicker portions of the slick will increase the emissivity by acting as an antireflection coating. When the "optical" thickness exceeds a quarter wavelength, the emissivity decreases again, and still increasing thickness will give a periodic modulation of emissivity. A two-frequency radiometer can determine oil thickness up to a

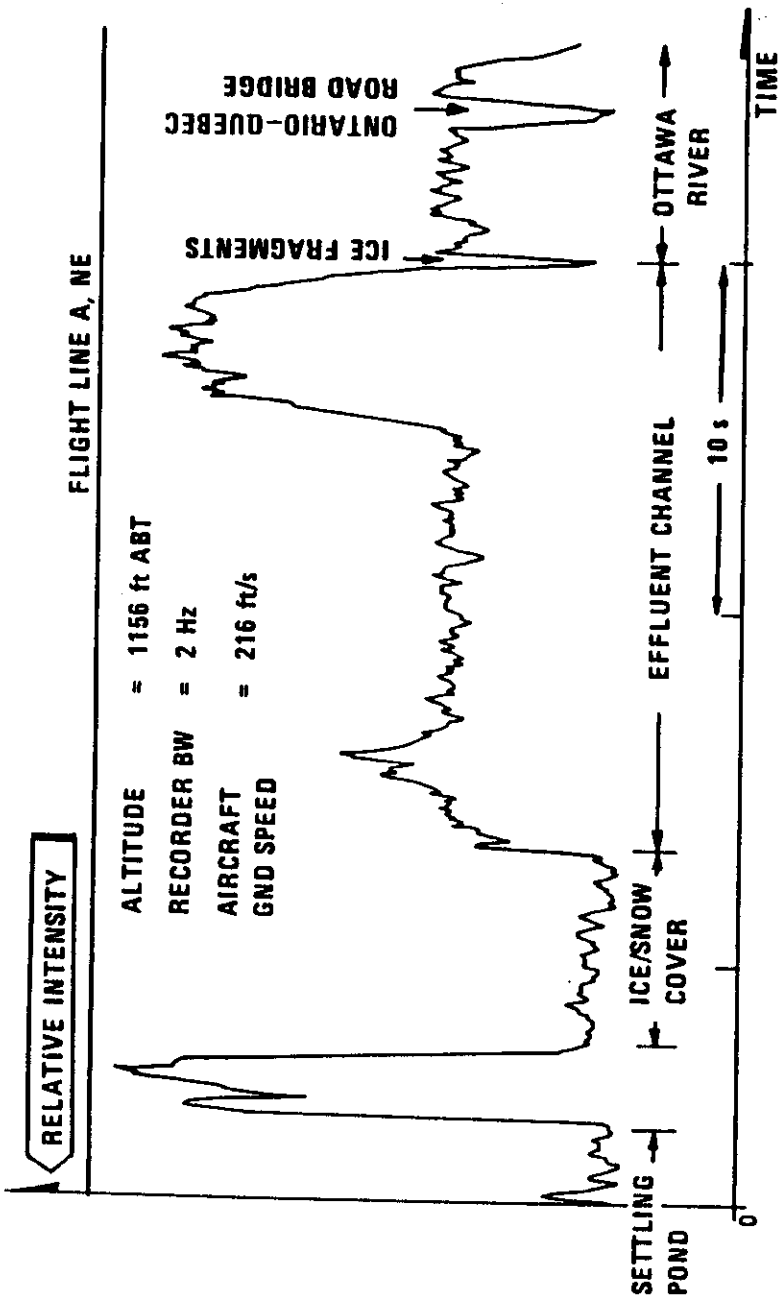

Figure 6.7 Fluorescence profile of pump mill settling pond and effluent channels. After M. Bristow [41].

quarter wavelength with adequate accuracy without previous knowledge about the dielectric constant of the particular oil type.

J. P. Hollinger from the Naval Research Laboratory, Washington, D. C., has led the efforts directed towards practical application of this principle. The NRL practical work is very advanced. Airborne measurements at 19.3 GHz, 31 GHz and 69.8 GHz have been carried out for a series of controlled oil spills [50]. Figure 6.8 shows the apparent temperature recorded when flying over an oil spill. Notice how the thick part of the spill shows up as a strong increase in emissivity, while the thin, outer part of the slick yields a slight reduction because of the missing capillary waves. Recently, the NRL operated an imaging version of the equipment. Coupled with computer processing, this permits rapid contouring of the thickness distribution of the slick to about 0.1-mm accuracy [51].

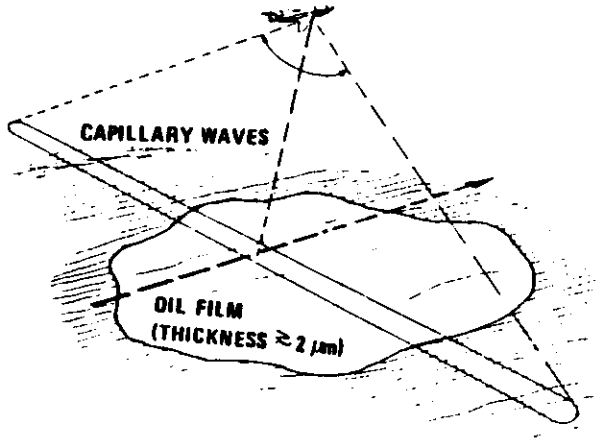

Figure 6.8 Detection of oil spills by side-looking radar (SLAR). The oil film suppresses capillary waves that have a dominating effect on the radar echo.

- *An IR Reflectometer.* This unit is based on characteristic anomalous dispersion in the index of refraction of both water and oil in the 2-4 μm band. Only stationary "across the river" installations are in use [52].

6.3 ATMOSPHERIC SURVEILLANCE

The atmosphere (troposphere and stratosphere) is the medium that has been subjected to the most extensive investigation. When studying techniques in connection with remote surveillance of the atmosphere, the following aspects are of importance:

- Measurement of atmospheric pollutants
- Measurement of the mechanisms responsible for the spreading of pollutants in the atmosphere: mean wind and turbulence
- Measurement of the parameters describing the dynamics of the atmosphere on which the spreading model relies: temperature distribution, precipitation.

These will now be summarized.

6.3.1 Atmospheric Constituents; Air Pollution

A laser has many advantages over a conventional thermal source of radiation for spectroscopy. It is highly monochromatic, it is coherent and highly directional, and its spectral brightness is greater by a factor of about 10^{16}. In the past the laser has suffered from a fatal disadvantage for many purposes—it could not be continuously tuned.

Various types of tunable coherent sources are now becoming available. In the visible and near infrared there are dye lasers, parametric oscillators and semiconductor diode lasers that cover the spectrum to about 30 μm. It is possible to mix the outputs in nonlinear media and thereby extend the frequency range. The spin-flip Raman laser, operating at 5 and 10 μm, is an example of a tunable laser. It is excited by a CO or CO_2 pump laser, the energy from which is directed into a cooled InSb sample. The radiation is scattered by a Raman process in which electrons reverse their spins in a magnetic field. The sample forms a cavity so that the Raman scattering takes place coherently with efficient

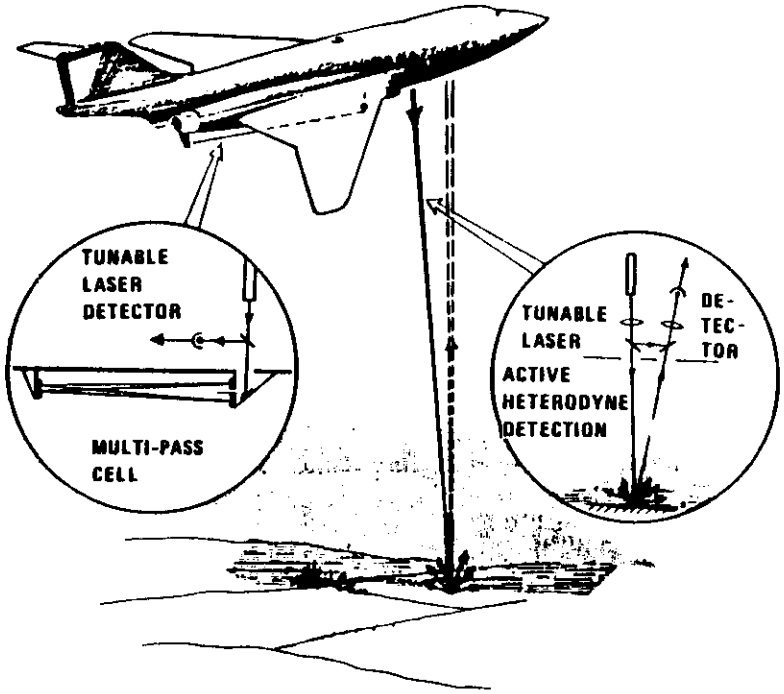

Figure 6.11 Measurement of air pollution by the use of an aircraft.

energy conversion into the scattered beam. The output frequency is controlled by varying the magnetic field in the sample.

6.3.1.1 A Brief Description of Some Important Spectroscopic Techniques (Dr. E. D. Hinkley, JPL, Dr. R. T. Menzies, JPL, Dr. F. Allario, NASA Langley)

1. *The differential absorption method* is presently one of the most powerful means of measuring small concentrations of particular pollutants averaging over an appropriate path that may be approximately a kilometer. There are several methods on the basis of

which the absorption coefficient, and hence the total gas concentration over a given path, can be measured:

- A pulsed laser can be used. The laser transmits wavelengths λ_1 and λ_2 alternatively. Wavelength λ_1 is in the absorption band, while λ_2 lies outside this band. At the receiving site (bistatic arrangement or a monostatic arrangement making use of a retroreflector) the ratio of the power received at the two frequencies $P_R(\lambda_2)/P_R(\lambda_1)$ is measured. Today it is possible to stabilize the laser system so as to be able to measure variation in $P(\lambda_1)/P(\lambda_2)$ down to 0.3%. The limiting factor with regard to detection sensitivity is then constituted by atmospheric turbulence in the absence of interfering gases. An example illustrating the potential of this technique is shown in Figure 6.12 [55-57].

2. *The derivative technique* is based on a frequency modulated laser (usually a diode laser). The laser frequency is centered on the slope of the appropriate absorption curve or line. A small frequency deviation allows the slope $dP/d\lambda$ to be measured. From this the concentration is derived. Using a high sweep rate (modulation frequency) and real time compensation of extinction fluctuations by monitoring the received power, the effect of turbulence can be minimized.

Typical sensitivities obtained with 1-km path length are as follows [58,59]:

Gas	CO	O_3	NO	SO_2	C_2H_4
Sensitivity, ppb	1.3	3	1.5	15	0.8

3. *The spectrophone* (Figure 6.13) measures the gas concentration at a point in the *in situ* manner. It is often referred to and should therefore be included in this survey. The laser is normally pulsed. The pulsed laser power gives rise to pulsed heat dissipation in the absorbing gas contained in the enclosure (shaded area on the figure). These heat pulses cause pressure variations that are measured by the microphone. Optimum sensitivity is achieved by a coherent detecting process. The advantage of this system relative to many other spectroscopic methods is that the sensitivity is proportional to the laser power. Typically 100 mW of power is used, giving parts per billion sensitivities.

The spectrophone appears to be a simple, noncritical instrument that presents an efficient solution to many problems. Whereas it was previously claimed that an acoustically resonant system is

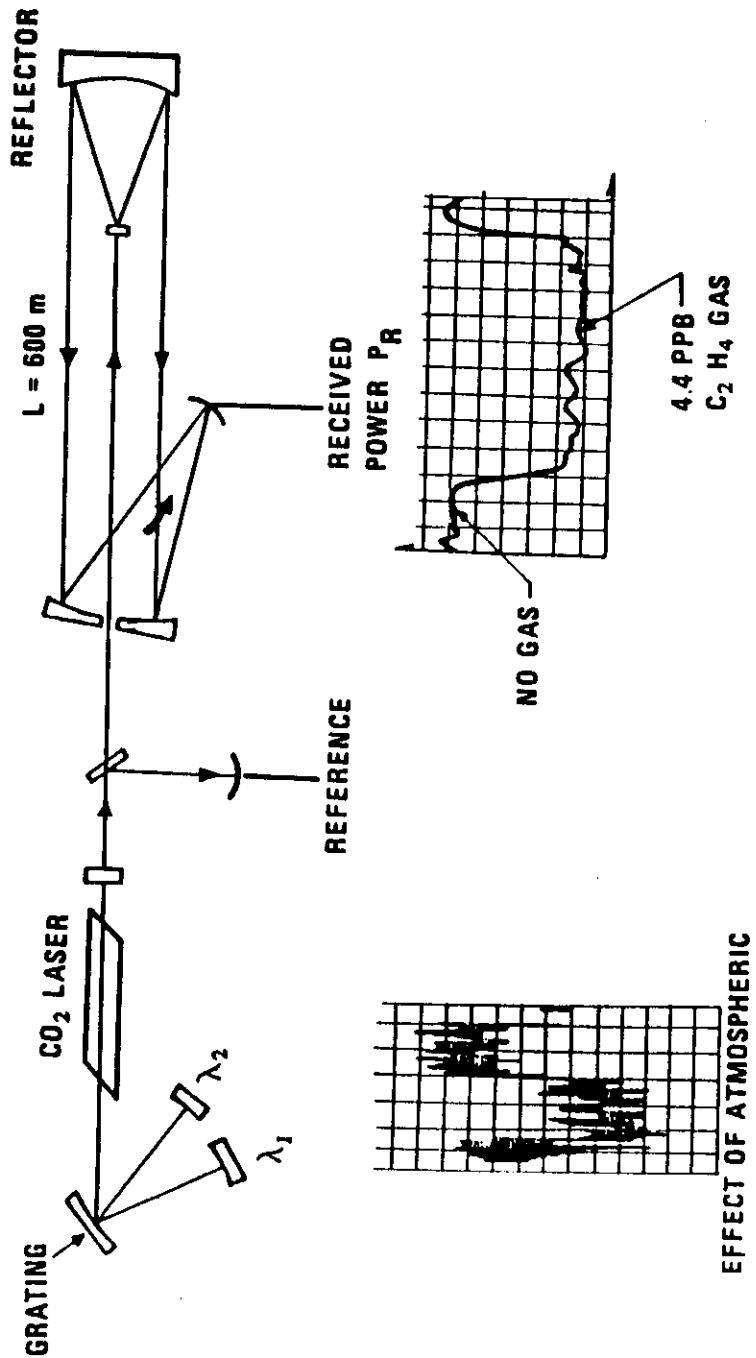

Figure 6.12 Results obtained with a dual wavelength CO_2 laser at the Norwegian Defence Research Establishment. S. O. Kanstad *et al.* [57].

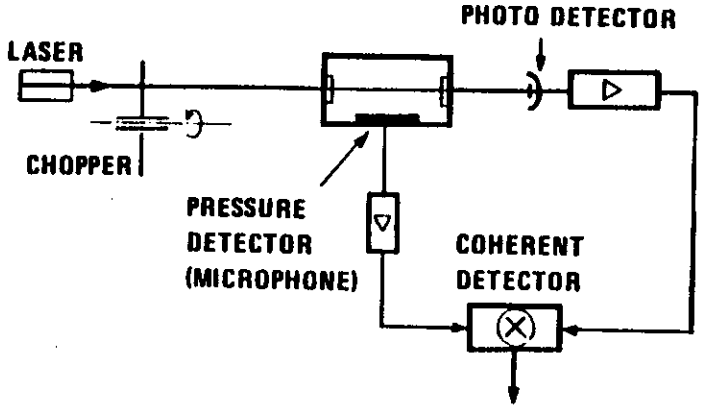

Figure 6.13 The principle of operation of a spectrophone

essential for high sensitivity, there are now many highly sensitive, nonresonant systems operating with a variety of simple microphone configurations [58-62]. The spectrophone will probably have an even greater impact on the spectroscopy of solids and liquids. Powder samples may be used and information about thermal diffusivity may be obtained by pulse rate response studies [63].

4. *Heterodyne receiving techniques* offer great improvements in system sensitivity relative to that of direct detection (order of 10^6), in particular in the infrared. Considerable progress is being made in heterodyne laser detection techniques. Limiting factors appear to be the stability of the local oscillator if this is to be a tunable one, in addition to various local oscillator noise effects. With fixed frequency local oscillators, a mixing efficiency of 0.5 is obtained; with less ideal sources (*e.g.*, a tuned diode laser) a 10 dB loss may be incurred. NASA Langley Research Center (Dr. Allario), in cooperation with the Airborne Instrument Laboratory in Melville, New York, has measured the vertical profile of atmospheric NH_3 from the ground to 15 km using a dual photomixer, dual local oscillator, and Infrared Heterodyne Spectrometer (IHS). The photomixers have a measured total bandwidth of 1.5 GHz, and a multi-IF channel, Dicke-switched output. Fixed frequency CO_2 lasers using the $C^{13}O_2^{16}$ isotope were used as local oscillators,

and the instrument was used in a solar pointing mode. The IHS was also used with waveguide $C^{12}O^{16}$ laser local oscillators to perform measurements of the vertical distribution (10-40 km) of stratospheric O_3 from an aircraft platform, the NASA CV-990. Preliminary measurements have been reported [64] and final reduction of the data is being compared to correlative O_3 chemical measurements from simultaneous balloon launches. Laboratory measurements are currently being performed at NASA Langley Research Center to study degradation factors in the signal-to-noise ratio and mixing efficiency when utilizing tunable diode lasers as local oscillators. Measurements on heterodyne noise effects induced by mode competition and cryogenic cooler instabilities are currently being studied [64-67].

6.3.1.2 Some Examples of Practical Results Obtained

1. *SO_2, N_2O, O_3; lidar techniques (J. M. Hoell, NASA Langley)* The differential absorption technique using a UV laser system and utilizing natural atmospheric particles as reflectors appears to have a great potential. NASA Langley uses a commercial flashlamp-pumped, frequency-doubled dye laser, a 0.25-m diameter receiver telescope, and a minicomputer for control, data acquisition and processing. The laser output is typically 100 μJ per pulse at 15 pulses per second for wavelengths coincident with the peaks and valleys in the SO_2 absorption spectrum from 296.0 to 300.1 nm. The difference in absorption coefficient for each pair of transmitted wavelengths is monitored using a satellite beam from the laser. The system is directed in a manner so as to record the SO_2 emitted from a steam plant in the neighborhood With the wind blowing in the appropriate direction, a suitable pollution source is obtained.

Through the use of near simultaneous pulses, the sensitivity of the system when averaging 100 pulses at each frequency in succession is about 10 ppb over a distance of 0.8 km. The system sensitivity is expected to be improved so as to give a 4-ppb sensitivity over a 1-km path. The only interferent gas is O_3, and the effect of this is small. See Figure 6.14 [68-70].

2. *Gases, CO_2 laser (Dr. R. T. Menzies, JPL).* A compact waveguide CO_2 laser system has been assembled at JPL for the

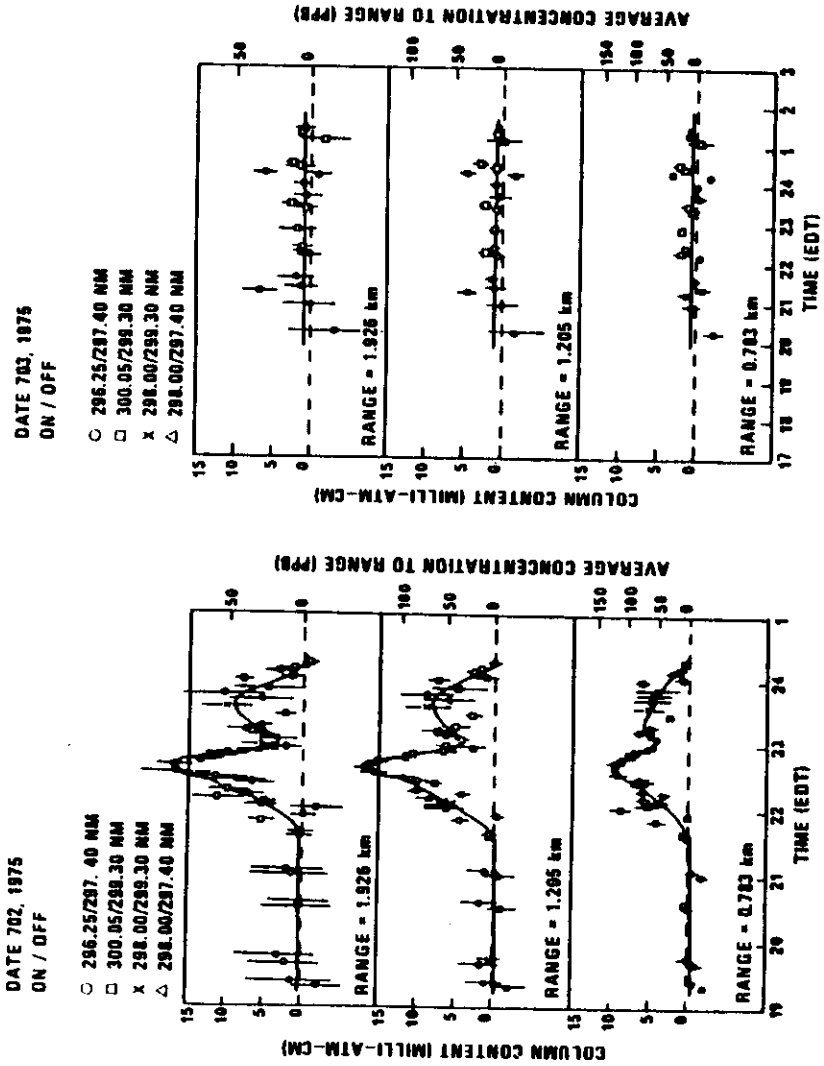

Figure 6.14 Time history of atmospheric sulfur dioxide concentration along measurement path to three ranges. After J. M. Hoell *et al.* [68].

measurement of O_3, C_2H_4 and NH_3, among others, using the ground as the reflector. The laser has been vibration-tested and clearly is remarkably robust (developed by Dr. R. L. Abrams, Hughes Research Laboratory). By means of this aircraft-mounted system the atmosphere will be measured using the ground as reflector. The system, which is based on heterodyne detection, is expected to measure variations in atmospheric absorption (measured signal) down to some 3% [71]. This figure is to be compared with the 0.3% obtained by Hinkley, MIT Lincoln Laboratory, using a ground-fixed installation with a retroreflector and diode tuning [58].

A system based on two separate CO_2 TEA lasers is being developed for an airborne application. The laser will be fired downwards from the aircraft. By using the ground as reflector, the total burden of a given pollutant (O_3) between ground and the aircraft is measured (Dr. Melfi, EPA):

- by direct detection method
- by transmitting the two frequencies in succession 12 μs apart in time
- by measuring the ratio of the power received at the two frequencies.

Note: no averaging is performed before the ratios are taken.

It is very probable that this system will be highly susceptible to the geometrical structure of the reflector, the ground. Since the power at the two frequencies is compared almost instantaneously in time (12 μs apart), the effect of turbulence is not likely to be important. A cassegranian telescope receiving system with a heterodyne detector based on a CO_2 waveguide laser is available commercially (Honeywell, Inc.).

3. *Particles; temperature inversions; laser scattering (Dr. J. A. Eckert, EPA).* EPA, Las Vegas, use an aircraft-mounted pulsed ruby laser looking downwards. The Lidar receiver echoes scattered from particles in the air and from the ground. This method localizes the boundary layer (temperature inversion) by increased backscatter due to its trapping of atmospheric particles. The system is also able to track plumes originating from industrial areas. The laser is pulsed at a rate of 1 pulse every 20 seconds. The spatial resolution is about five meters. A very detailed structure (isolines of reflectivity) is obtained; these look very similar

to the isoplates of temperature obtained from acoustic backscatter systems (Sodars) (see Figure 6.15). The system is bulky and heavy (600 pounds) [72].

A new compact system (90 x 30 x 40 cm) based on a *dye laser* that can be fired once every second has now been developed. This system displays the data in real time on board the aircraft, making the device particularly useful for tracking plumes.

Finally, a neodynium YAG laser is under development. This will give spatial resolution of some 15 ft and it will have facilities for two-frequency operation. This will make it possible to obtain some information about particle size distribution.

NASA Langley is investigating techniques for the measurement of *particle size distribution* up to a height of some 20 km in the atmosphere. The experimental scattering cross section versus frequency relationship shows a fine-scale structure (interference effects) that is not fully revealed by the Mie theory (Dr. Allario).

To learn something about the mechanisms involved, microwave simulation techniques are used. Objects with shapes and dielectric constants similar to those of natural aerosols are produced (scaled from laser wavelengths to microwave wavelengths). The results of these scatter model experiments are scaled back to practical laser cases. These simulated results are then compared with the results from atmospheric laser experiments. Based on this method the atmospheric particle size distribution is synthesized.

4. *Stratospheric hydrochlorides (C. R. Farmer and Associates, JPL).* Farmer uses a high resolution Fourier transform interferometer spectroradiometer (FTS) in the 1800-5600 cm^{-1} with a spectral resolution of 0.13 cm^{-1} [73].

An aircraft is used as the platform at 60,000 ft and limb scanning is performed (Concordes in cooperation with UK and France, and U2 in the USA). Measuring the profile of HCl from the ground and up to 21 km revealed that the concentration decreased from approximately 1 ppb near the ground to a very much smaller value at the height of the tropopause. From this height the concentration increased again and reached 0.6 ppb at 21-km height. Later balloon experiments have confirmed this. At 37 km the observed mixing ratio is 1.7 ppb.

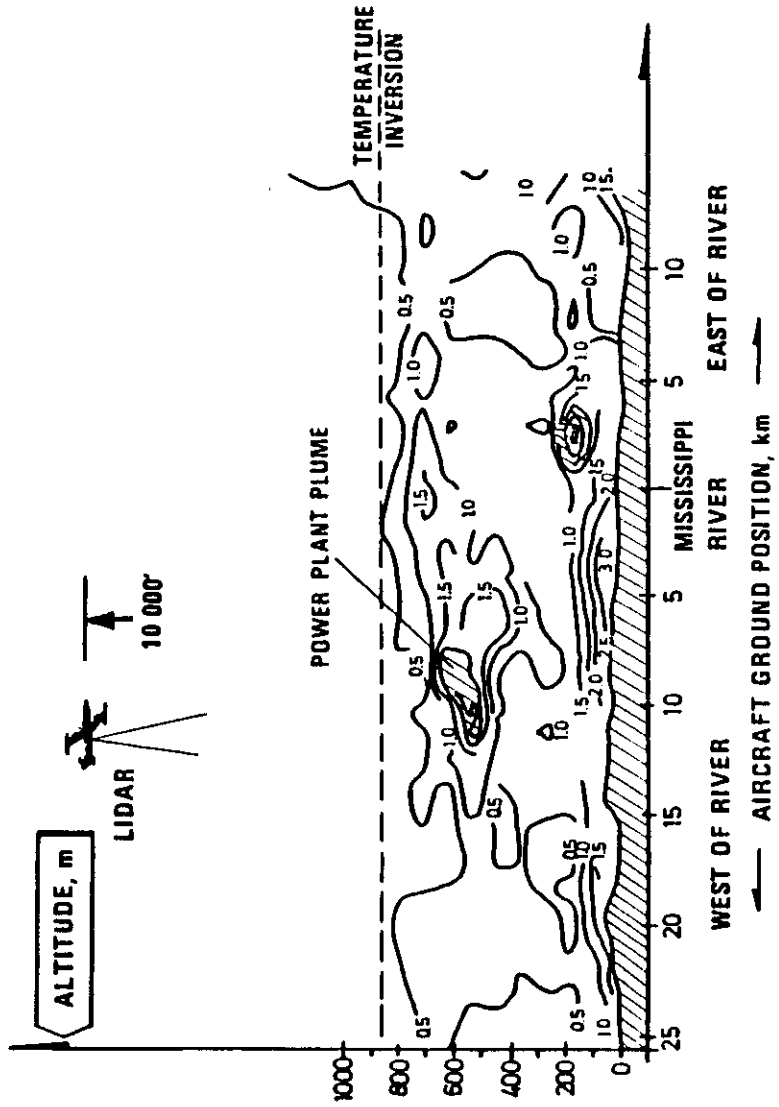

Figure 6.15 Isoscattering contour plot. After Eckert, EPA [72].

6.3.2 Atmospheric Wind

Remote measurement of the atmospheric wind field has been the subject of investigation at many research establishments for more than a decade. In addition to serving the pollution transport modellers, wind probing techniques are of importance in aviation. Consequently the effort in this field of science is considerable and the number of different techniques of significant potential is large. In this brief report only a few will be mentioned.

1. *Laser Doppler Techniques*

The NASA-MSFC has developed laser Doppler systems for remote measurement of atmospheric wind velocity and turbulence. These systems utilize the Doppler frequency shift of the laser light when it is scattered by minute particles suspended in the atmosphere. The velocity is determined directly from the measurement of the difference in frequency between the scattered and reference laser energy and the geometry of the system. The Doppler frequency is directly proportional to velocity. The feasibility of

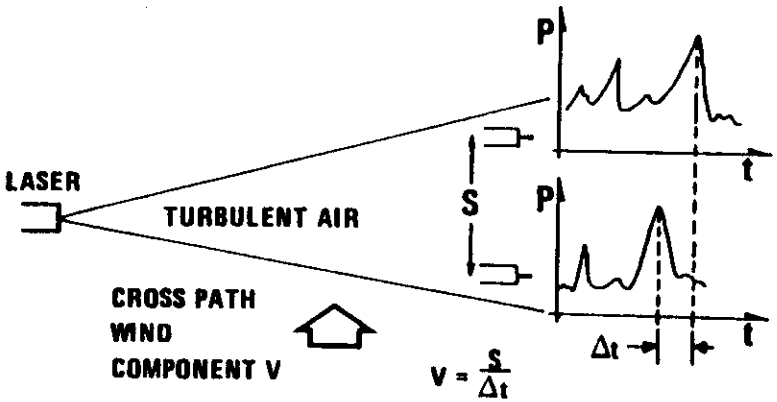

Figure 6.16. The principle of laser scintillation anemometer. The refractivity irregularities blown through the beam cause the laser signal to scintillate. The spatial correlation of these fluctuations gives information about wind speed.

measuring atmospheric wind velocity and turbulence, using a CO_2-laser Doppler system, was demonstrated at NASA in 1968. Since 1968 this technology has been directed toward (1) the development of a laser Doppler system for the detection and measurement of clear air turbulence in an onboard airline warning system, (2) the development of laser Doppler systems for detection, tracking and measurement of aircraft tailing vortices, and (3) research measurement of particular atmospheric wind fields.

Lidar (or "laser radar") provides a unique technique for observing the temporal and spatial variation of the atmospheric aerosol. Both particles and the atmospheric gases elastically backscatter pulsed laser energy at optical or near-optical wavelengths and provide information on the presence, location, and, with qualifications, the concentration of the scatterers.

Such observations are valuable in their own right, showing the structure of the atmosphere as revealed by the degree and variations of its particulate loading. Lidar measurements can also be valuable in conjunction with other observations concerned with radiative energy transfer in the atmosphere–especially of the passive type–since they provide data to complement and support information obtained on the basis of the radiometric instrumentation alone [75].

An *IR Doppler System* has been developed by Dr. R. L. Schwiesow and others of WPL, NOAA. The radial component is measured with a CW-CO_2 laser. The signal backscattered from aerosols is mixed with an infrared local oscillator. The heterodyne beat frequency is proportional to radial wind speed. Range resolution is achieved by beam focusing of the 30-cm coaxial optics. The range resolution is 10 m at 100 m and degrades as the square of the range. Angular resolution is 0.1 milliradians. Transmitted power is 3 watts CW. A spectrum analyzer yields a complete velocity-component spectrum as often as every 10 ms.

A system mounted in a light truck has been used for boundary-layer wind profile measurements to a range of 1 km. A similar system in a light aircraft has been used for the study of waterspouts and cloud dynamics. Closely-spaced multiple beams have been used to demonstrate the measurement of all three components of the velocity at a single point in space [76].

2. *Optical Scintillation Methods*
(Dr. R. S. Lawrence, WPL, NOAA)

The present methods involving line-of-sight measurements with two transversally spaced receivers and cross-correlation measurement give essentially the path average cross wind. The system may either be a one-ended system using a naturally illuminated scene (hillside, forest or buildings) as the source, or a double-ended system with a laser as the source. In the passive mode (one-ended system) the two-dimensional spatial spectrum of the scene, which in general is not the same as the white spectrum of a point laser source, has to be specified [77,78].

3. *Scintillation Method Using Spatially Filtered Apertures*
(Dr. R. W. Lee, Dr. A. T. Waterman, Stanford)

The idea of this wind-measuring technique is by the use of spatially filtered apertures to measure the transverse wind velocity as a function of the position along the path. Using two spatially filtered apertures (both transmitter and receiver) it can be shown that the observed variance at receiver output is associated with the intensity of a particular Fourier component of the refractivity irregularities located at a known distance from the transmitter. Measurements of the fluctuation frequency then lead immediately to the determination of the wind velocity through the use of Taylor's hypothesis ($2\pi f = VK$). The available space resolution is high, approximately 1% of the path length, which again may range from 10 m (optical and acoustic frequencies) to tens of kilometers (millimeter waves) [79].

4. *FM/CW Radar System*
(Dr. E. E. Gossard, Dr. R. B. Chadwick, WPL, NOAA)

Great advances have been made in this field largely due to new and very effective data reduction methods which give both the distribution in space of the scattering cross section (scattering caused by irregularities in refractive index) and the distribution in space of wind (systematic as well as the turbulent component, the variance). The technique for separating the Doppler information from the range information in short is as follows.

The signal from the homodyne mixer (frequency contains information on range + Doppler) is A/D converted. The Doppler

velocity spectrum (Doppler shift as well as Doppler broadening) is obtained from each resolution cell by computing the power spectrum from a sequence of consecutive sweeps. Target range is obtained from the signal frequency by means of the usual FM/CW technique. The technique offers a unique solution to the problem of all-weather velocity measurements in the atmosphere up to a height of some 2 km.

The vertical profile of mean wind and of the wind fluctuations can be obtained along any line in the atmosphere within the region of the radar (hemisphere of radius 2 km). Days with little refractivity variations present a problem. In order to take care of such conditions an extra 20 dB sensitivity is desirable [80].

5. *Meteorological Doppler Radar for Measurement of Storm Structure by Measuring the Raindrop Distribution*
(Dr. E. E. Gossard, WPL, NOAA)

Two radars are used to obtain direction of particle motion. Chaff has been used with great success in daytime with convective activities holding the chaff up and causing good mixing and spreading of the chaff. Recent developments indicate that the system may operate also in clear air conditions [81].

6. *Acoustic Radar Techniques*
(Dr. F. F. Hall, WPL, NOAA)

The acoustic Doppler radar (Figure 6.17) is also a powerful tool. By this, wind velocity and wind variance profiles can be obtained up to a height of some 500 m. Under conditions of high wind speed over the antenna, acoustic noise and drift of the acoustic wavefront are a hindrance. Wind shear investigations are routinely carried out at Denver Airport using the technique [82].

6.3.3 Atmospheric Temperature Distribution

In connection with the study of the dynamics of the atmosphere, information about temperature distribution (vertical profile) is imperative. Consequently, considerable effort has been invested to establish remote probing techniques. This has proved to be difficult. Although, as we shall see in the following, remote probing techniques have been developed, they are at present

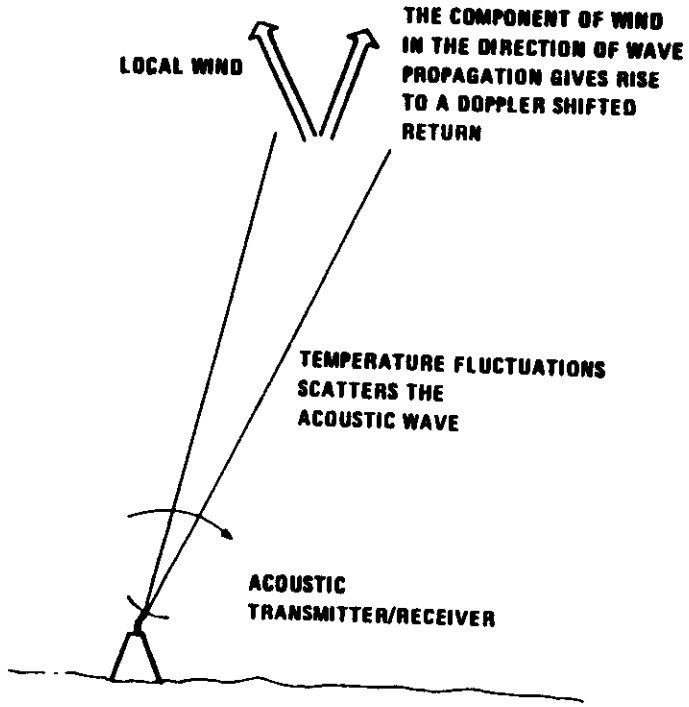

Figure 6.17 The acoustic Doppler radar for measurement of wind speed.

considered inadequate because of insufficient height resolution. However, a few methods should be mentioned.

1. *Passive Radiometry*

A passive microwave radiometer is tuned to the frequency corresponding to an absorption line (emission line) of a particular gas, such as O_2. The signal that the radiometer receives (ground-based or placed in an aircraft or a satellite) is determined by the temperature of the gas and its concentration. Knowing the concentration, which in general is the case with O_2, enables deduction of the temperature. However, our interest is not the mean temperature through the whole depth of the atmosphere, but the temperature profile. Therefore, one will have to make use of another characteristic feature of the radiating gas. The width of the frequency spectrum (line width) that a given gas emits is determined

by the pressure and the molecular temperature. Accordingly, if the emission is measured at a set of closely spaced frequencies around the emission line, the temperature profile may be obtained by solving the integral equation (inversion technique) provided the pressure profile is known. In practice, however, this does not give very good height resolution due to lack of knowledge of precise pressure profile [83].

2. *Active Raman Backscatter Technique*

The Raman backscattered intensity is proportional to the molecular density of the particular gas (*e.g.*, N_2). The backscattered power in the Raman process is distributed over several rotational and vibrational emission lines. The relative strength of these lines is determined by the temperature of the N_2 molecules. Hence, measuring the distribution of line intensity, the temperature can be obtained. Unfortunately, however, also this method suffers from comparatively poor spatial resolution and poor sensitivity.

3. *Radio Acoustic Sounding System (RASS)*
(Dr. A. T. Pedersen, Stanford)

An acoustic grating whose velocity is determined by air density (temperature dependent) is "'chased" by a radio wave with wavelength twice the acoustic wavelength. The RF wave is scattered back (Bragg scattering) and the Doppler shift is measured. Thus the velocity of the acoustic wave is measured and hence the temperature. This method suffers from destruction of the acoustic phase front as a result of wind, but is in other respects effective.

REFERENCES

1. Gordy, W. "Microwave spectroscopy," *Handbuch der Physik* (Berlin: Springer-Verlag, 1957), p. 28.
2. Ghosh, S. H. and V. Malaviya. "Microwave absorption in the earth's atmosphere," *J. Atmos. Terr. Phys.* 21:4 (1961).
3. McClatchey, R. A. *et al.* "AFCRL atmospheric absorption line parameters compilation," AFCRL-TR-73-0096, ERP434 (1973).
4. Ratcliffe, J. A. "Some aspects of diffraction theory and their application to the ionosphere," *Rep. Progr. Phys.* 19:188 (1956).
5. Gjessing, D. T. "Determination of permittivity variations in the troposphere by scatter-propagation methods," *Proc. IEE Monograph* 501 E, April 1962, *Proc. IEE Part C*, 109:16 (1962).
6. Batchelor, G. K. "The scattering of radio waves in the atmosphere by turbulent fluctuations in refractive index," Research Report EE262, School of Electrical Engineering, Cornell University (1955).
7. Balser, M. "Some observations on scattering by turbulent inhomogeneities," *Trans. IRE* AP-5(4):383 (1957).
8. Gjessing, D. T. "Atmospheric structure deduced from the forward scatter wave propagation experiments," *Radio Sci.* 4(12):1195-1210 (1969).
9. Wiener, N. "Generalized harmonic analysis," *Acta Mathematica* 55:117 (1930).
10. Gjessing, D. T. "On the influence of atmospheric refractive index irregularities on the resolution performance of a radar," *Atmospheric Effects on Radar Target Identification and Imaging.* H. Jeske, Ed. (D. Reidel Publishing Company, 1975).
11. Hagfors, T. "Investigation of the scattering of radio waves at metric wavelengths in the lower ionosphere," *Geophys. Norvegia* 21:2 (1959).
12. Gjessing, D. T. and J. Borresen. "The influence of an irregular refractive index structure on the spatial field-strength correlation of a scattered radio wave," *IEE Conf. Proc.* 48:September 1968.
13. Rice, S. O. "Mathematical analysis of random noise," *Bell Systm. Tech. J.* 23:282 (1944).
14. Gjessing, D. T. and F. Irgens. "On the scattering of electromagnetic waves by a moving tropospheric layer having sinusoidal boundaries," *IEE Trans. PTGAP* AP-12:1 (1964).

15. Gjessing, D. T. and F. Irgens. "Scattering of radio waves by a moving atmospheric rippled layer; A simple model experiment," *IEE Trans. PTGAP* AP-12:6 (1964).
16. Gjessing, D. T. "On the radiometeorological determination of refractive index and air velocity spectra of the troposphere," *Radio meteorologie en vue de l'application aux telecommunications*, P. Misme, Ed. (Liege: Vaillant-Carmanne Publishing Company, 1966).
17. Gjessing, D. T. "Radiophysical aspects of irregular structure in the atmosphere," *Atmospheric Turbulence and Radio Wave Propagation*, A. M. Yaglom, V. I. Tatarsky, Eds. (Moscow: Nauka Publishing House, 1967).
18. Lee, R. W. and J. C. Harp. "Weak scattering in random media," *Proc. IEEE* 57:375 (1969).
19. Kjelaas, A. Private communication.
20. Gjessing, D. T., A. G. Kjelaas and J. Nordo. "Spectral measurements and atmospheric stability," *J. Atmos. Sci.* 26(3):462-468 (1969).
21. Gjessing, D. T. and K. S. McCormick. "On the prediction of the characteristic parameters of long distance tropospheric communication links," *IEE Trans.* COM-22:9 (1974).
22. Gjessing, D. T. "On the use of forward scatter techniques in the study of turbulent stratified layers in the troposphere," *Bound Layer Meteorol.* 4:377-396 (1973).
23. Janes, H. B. and M. C. Thompson. "Comparison of observed and predicted phase-front distortion in line-of-sight microwave signals." *Trans. IEE* AP-21(2):263-311 (1973).
24. Kjelaas, A. G., P. E. Nordal and A. Bjerkestrand. "Multiwavelength scintillation effects in a long-path CO_2 laser absorption spectrometer," Proc URSI Commission F Symposium, La Baule, France, 28 April - 6 May 1977.
25. Gjessing, D. T. "A generalized method for environmental surveillance by remote probing," *J. Radio Sci.* March/April (1978).
26. Gjessing, D. T. "Scattering mechanisms and channel characterization in relation to broadband radio communication systems," AGARD Conf. Proc. *Aspects of Electromagnetic Scattering in Radio Communications*, Cambridge, Massachusetts, October 1977.
27. Plant, W. J. "Studies of backscattered sea return with a CW, dual-frequency, X-band radar," *IEE Trans.* AP-25:28 (1977).
28. Alpers, W. and K. Hasselmann. "The two-frequency microwave technique for measuring ocean wave spectra from an airplane or satellite," (1977).

29. Barrick, D. E. "Remote sensing of sea state by radar," *Remote sensing of the Troposphere*, V. E. Derr, Ed. (Washington, D.C.: U.S. Government Printing Office, 1972).
30. Wilheit, T. T. and M. G. Fowler. "Microwave radiometric determination of wind speed at the surface of the ocean during BESEX," *IEE Trans.* AP–25:111-120 (1977).
31. Webster, W. J., Jr., T. T. Wilheit, D. B. Ross and P. Gloersen. "Spectral characteristics of the microwave emission from a wind-driven, foam-covered sea," *J. Geophys. Res.* 81:3095 (1976).
32. *Project plan for SeaSat–A 1978 Mission.* Project document 622-3, Jet Propulsion Laboratory, Pasadena, California.
33. Briscoe, M. G., O. M. Johannessen and S. Vincerzi. "The Malthese oceanic front: a surface description by ship and aircraft," *Deep Sea Res.* 21:247-262 (1974).
34. Blume, H-J. C. and B. M. Kendall. "Measurement of ocean temperature and salinity via microwave radiometry," *Bound Layer Met.* (1977).
35. Thomann, G. C. "Remote measurement of salinity in an Estuarine environment," *Remote Sensing Environ.* 2:249-259 (1973).
36. Smith, S. D., M. I. Colles and G. Peckham. "The measurement of surface pressure from a satellite," *Quart. J. Roy. Meteorol. Soc.* 98(416): 431-433 (1972).
37. Barrick, D. E., J. M. Headrick, R. W. Bogle and D. D. Crombie. "Sea backscatter at HF: Interpretation and utilization of the echo," *Proc. IEE* 62(6):673-680 (1974).
38. Barrick, D. E. "First order theory and analysis of MG/HG/VHF scatter from the sea," *IEE Trans.* AP-20(1):2-10 (1972).
39. Crombie, D. D. "Backscatter of HP radio waves from the sea," *Electromagnetic Probing in Geophysics*, J. Q. Wait, Ed. (Boulder, Colorado: The Golden Press, 1971), pp. 131-162.
40. Measures, R. M. and M. P. F. Bristow. "The development of a laser fluorosensor for remote environmental probing," AIAA Paper 71-1121, Joint Conference on Sensing of the Environmental Pollutants, Palo Alto, California, November 8-10, 1971.
41. Bristow, M. P. F. "Airborne monitoring of surface water pollutants by fluorescence spectroscopy," Submitted for publication in *Remote Sensing of the Environment*.
42. Kim, H. H. "New algae mapping technique by the use of an airborne laser fluorosensor," *Appl. Optics* 12(7):1454-1459 (1973).

43. Mumola, P. B., O. Jarrett and C. A. Brown. "Multiwavelength lidar for remote sensing of chlorophyll *a* in algae and phytoplankton, *The Use of Lasers for Hydrographic Studies*, H. H. Kim, Ed., Proceedings of a symposium held at NASA Wallops Flight Center, September 12, 1973.
44. Browell, E. V. "Analysis of laser fluorosensor systems for remote algae detection and quantification," NASA TN D-8447 (June 1977).
45. Pilon, R. O. and C. G. Purves. "Radar imagery of oil slicks," *Proc. IEE* AES-9:630 (1973). "Remote sensing of southern California oil pollution experiment, US Coast Guard Office of R&D, report July 1971.
46. "Development of a prototype airborne oil surveillance system." Final report May 1975, Prepared for US Coast Guard by Aerojet Co.
47. Axelsson, S. "Remote sensing of oil slicks," Report RL-0-3 R27, SAAB/SCANIA AB (May 1975).
48. Nilsson, J. and T. Hagman. "Detektering av aljeutsläpp med radar," FOA report (1975).
49. Fontanel, A. and A. Roussel. "La détection des nappes d'hydrocarbures sur la mer," Report from Institut Francais du Pétrole/Centre National pour l'Exploitation des Océans (1976).
50. Hollinger, J. P. "The determination of oil slick thickness by means of multi-frequency passive microwave techniques," NRL Memorandum Report 2953 (June 1974).
51. Troy, B. E. and J. P. Hollinger. "The measurement of oil spill volume by a passive microwave imager," NRL Memorandum Report 3515 (May 1977).
52. Rambie, G. S., Jr. "A practical oil sensor," *Proc. 9th Symposium Remote Sensing of Environment* 1457-1466 (Ann Arbor, Michigan: University of Michigan, April 1974).
53. DeLoor, G. P. *et al.* "Radar cross sections of vegetation canpies determined by monostatic and bistatic scatterometry," *Proc. 9th Symposium Remote Sensing Environment* 1457-1466 (Ann Arbor, Michigan: University of Michigan, April 1974).
54. Schanda, E. "Microwave investigations of snow and soil moisture in Switzerland," *Proceedings of the First General Assembly of EARSeL* (European Association of Remote Sensing Laboratories), Strasbourg, March 23-24 (1977).
55. Ku, R. T., E. D. Hurkley and J. O. Sample. "Long-path monitoring of atmospheric CO with a tunable diode laser system," *Appl. Optics* 14:854-861 (1975).

56. Byer, R. L. and M. Garburry. "Pollutant detection by absorption using Mie scattering and topographic targets as retroreflectors," *Appl. Optics* 2:1496 (1973).
57. Kanstad, S. O., A. Bjukestrand and T. Lund. "Tunable dual line CO_2 laser for atmospheric spectroscopy," *J. Physics E:-Scientific Instruments* 10:998 (1977).
58. Hinkley, E. D. "Development and application of tunable diode lasers to the detection and quantitative evaluation of pollutant gases," Final technical report to the US Environmental Protection Agency (1971)
59. Sulzmann, K. G. P., J. E. G. Lowder and S. S. Penner. "Estimates of possible detection limits for combustion intermediates and products with line-center absorption and derivative spectroscopy using tunable lasers," *Combust. Flame* 20:177-191 (1973).
60. Delaney, M. E. "A Review of early spectrophone applications," *Sci. Prog.* 47:459 (1959).
61. Krenzer, L. B. "Ultralow gas concentration infrared absorption spectroscopy," *J. Appl. Phys.* 42(7):2934-2943 (1971).
62. Rosengren, L. G. "Optimal optoacoustic detector design," *Appl. Optics* 14(8):1960 (1975).
63. Rosenswaig, A. "Photoacoustic spectroscopy of solids," *Physics Today* 28 (1975).
64. Peyton, B. J. *et al.* "Infrared heterodyne spectrometer measurements of vertical profile of tropospheric ammonia and ozone," Presented at the AIAA 15th Aerospace Sciences Meeting, Atmospheric Environment Session, Los Angeles, California, January 24-26, 1977.
65. "Inner hemispheric survey of minor upper atmospheric constituents during October-November 1976," NASA TMX-73630.
66. Hinkley, E. D. and P. L. Kelley. "Detection of air pollutants with tunable diode lasers," *Science* 171:635 (1971).
67. Menzies, R. T. "Laser heterodyne detection techniques," *Laser Monitoring of the Atmosphere*, E. D. Hinkley, Ed. (Berlin: Springer-Verlag, (1976).
68. Hoell, J. M., W. R. Wade and R. T. Thompson, Jr. "Remote sensing of atmospheric SO_2 using the differential absorption lidar technique," Presented at International Conference on Environmental Sensing and Assessment (1975).
69. Browell, E. V., L. Perillo and F. S. Mills. "Double-pulse UV dia. system for measurement of SO_2," Presented at 8th International Laser Radar Conference, Drexel University, Philadelphia, Pennsylvania, June 6-9, 1977.

70. Grant, W. B. *et al.* "Calibrated remote measurement of NO_2 using the differential absorption backscatter technique," *Appl. Phys. Lett.* 24:550-552 (1974).
71. Menzies, R. T. and M. T. Chanine. "Remote atmospheric sensing with an airborne laser absorption spectrometer," *Appl. Optics* 13:2840 (1974).
72. Eckert, J. A., *et al.* "Downlooking airborne lidar studies," August 1974. EPA report, EPA, Las Vegas, Nevada (1974).
73. Farmer, C. B. "Infrared measurements of stratospheric composition," *Can. J. Chem.* 52:1544-1559 (1974).
74. Schnidler, R. A. "A small, high speed interferometer for aircraft, balloon and spacecraft applications," *Appl. Optics* 9:301-306 (1970).
75. Huffaker, R. M. "Laser Doppler detection system for gas velocity measurements," *Appl. Optics* 9:1026-1039 (1970).
76. Abshire, N. L., R. L. Schwiesow and V. E. Derr. *J. Appl. Meteorol.* 13:951 (1974).
77. Lawrence, R. S., G. R. Ochs and S. F. Clifford. "The use of scintillations to measure average wind across a light beam," *Appl. Optics* 11:239 (1972).
78. Clifford, S. F., G. R. Ochs and T-i. Wang. "Optical wind sensing by observing the scintillations of a random scene," *Appl. Optics* 14:2844 (1975).
79. Lee, R. W. "Remote probing using spatially filtered apertures," *J. Opt. Sec. Am.* 64:1295 (1974).
80. Chadwick, R. B., E. E. Gossard and R. G. Strauch. "Analysis of an all-weather system for wind sounding up to 15 km altitude," Technical Report ERL 334-WPL 41, NOAA, US Department of Commerce (1975).
81. Miller, L. J. "Internal airflow of a convective storm from Dual-Doppler Roydon measurements," *Pure Appl. Geophys.* 113:765 (1975).
82. Beran, D. W. and F. F. Hall, Jr. "Remote sensing for air pollution meteorology," *Bull. Am. Meteorol. Soc.* 55:9 (1974).
83. Westwater, E. R., J. B. Snider and A. V. Carlson. "Experimental determination of temperature profiles by ground based microwave radiometry," *J. Appl. Meteorol.* 14:524 (1975).